


**UCC Library and UCC researchers have made this item openly available.  
Please [let us know](#) how this has helped you. Thanks!**

<b>Title</b>	Monolithic integration of photonic devices for use in a regrowth-free coherent WDM transmitter
<b>Author(s)</b>	Kelly, Niall P.
<b>Publication date</b>	2017
<b>Original citation</b>	Kelly, N. 2017. Monolithic integration of photonic devices for use in a regrowth-free coherent WDM transmitter. PhD Thesis, University College Cork.
<b>Type of publication</b>	Doctoral thesis
<b>Rights</b>	© 2017, Niall Kelly. <a href="http://creativecommons.org/licenses/by-nc-nd/3.0/">http://creativecommons.org/licenses/by-nc-nd/3.0/</a> 
<b>Item downloaded from</b>	<a href="http://hdl.handle.net/10468/5738">http://hdl.handle.net/10468/5738</a>

Downloaded on 2019-12-02T13:50:07Z

# Monolithic Integration Of Photonic Devices For Use In A Regrowth-Free Coherent WDM Transmitter

Niall Kelly



National University of Ireland, Cork

Faculty of Science

Department of Physics

Thesis submitted for the degree of

Doctor of Philosophy

August 2017

Supervisors: Prof Frank H Peters

Mr Brian Corbett

Head of Department: Prof John McInerney

# Contents

<b>1. Optical Communications.....</b>	<b>1</b>
1.1 Introduction .....	1
1.2 Wavelength Division Multiplexing.....	4
1.3 Dispersion and Non-Linear Effects .....	5
1.4 Traditional WDM.....	6
1.5 Coherent WDM.....	7
1.6 Modulation Formats.....	10
1.7 Photonic Integration.....	14
<b>2. Photonic Integrated Circuits.....</b>	<b>19</b>
2.1 Introduction .....	19
2.2 Semiconductor Based Technology.....	19
2.3 Optical Waveguides .....	24
2.4 Semiconductor Lasers.....	27
2.5 Semiconductor Modulators.....	31
2.6 Photonic Integration Techniques.....	35
2.7 Proposed Coherent WDM PIC.....	36
<b>3. Photolithographic Mask and Semiconductor Process Design.....</b>	<b>45</b>
3.1 Introduction.....	45
3.2 Photolithographic Mask Design.....	45
3.3 Self-Aligned Deep and Shallow Etch Process.....	47
3.4 DC Process... ..	49
3.5 High Speed Process.....	55
3.6 Summary....	64
<b>4. Single Model Laser Based On Dual Port Multimode Interference Reflector.....</b>	<b>67</b>
4.1 Introduction .....	67
4.2 Multimode Interference Devices .....	67
4.3 Waveguide Slot Characterization.....	69
4.4 MIR Test Structures.....	72
4.5 MIR Laser Test Devices.....	76
4.6 Mir Facetless Laser....	76
4.7 Summary.....	82
<b>5. Monolithic Regrowth-Free Coherent WDM PIC.....</b>	<b>85</b>
5.1 Introduction .....	86
5.2 First Generation PIC.....	86
5.3 Second Generation PIC.....	92
5.4 Third Generation PIC.....	96
5.5 Integration of SFP Laser and EAM.....	102

5.6	Summary.....	107
<b>6.</b>	<b>High Speed Electroabsorption Modulators.....</b>	<b>111</b>
6.1	Introduction .....	111
6.2	High Speed EAM Electrode Design.....	111
6.3	High Speed Epitaxial Design.....	115
6.4	RF Pedestal Characterization.....	118
6.5	Lumped Element EAM Array.....	120
6.6	50 $\mu\text{m}$ Lumped Element EAM.....	122
6.7	Curved EAM Design.....	128
6.8	Summary.....	134
<b>7.</b>	<b>Conclusions And Future Work.....</b>	<b>139</b>
7.1	Summary.....	139
7.2	Future Work.....	140
<b>Appendix A:</b>	<b>Epitaxial Structures.....</b>	<b>143</b>



I, Niall Kelly, certify that this thesis is my own work and I have not obtained a degree in this university or elsewhere on the basis of the work submitted in this thesis.

*Niall Kelly*

# Acknowledgements

I would like to thank my supervisors Frank Peters and Brian Corbett for giving me the opportunity to work in such an interesting field. I am grateful for their support over the course of my studies. I would also like to thank James O'Callaghan for mentoring me in the dark arts of semiconductor device fabrication. I am grateful to all the members of IPG, the Tyndall Taggers, UCC Rugby and the greater Tyndall community for providing me with friendship and countless good memories over the years.

Thanks a million to my family for their unwavering support. I couldn't have done it without you. And last but not least, Roxane you're a star. Merci buckets.

*For Tommy,*

# List of Publication

## Journal Articles

1. **N. P. Kelly**, J. O’Callaghan, A. Goclinska, K. Thomas, E. Pelucchi and F.H. Peters, “Curved Lumped Element Electroabsorption Modulator Based On A Trapezoidal Bend”, Applied Optics, (under review).
2. **N. P. Kelly**, M. Dernaika, L. Caro, P. E. Morrissey, F. H. Peters, “Monolithic Integration Of Photonic Devices For Use In A Regrowth-Free CoWDM Transmitter”, IEEE Photonics Technology Letters , 29 (12), 2017.
3. **N. P. Kelly**, L. Caro, M. Dernaika, and F.H. Peters, “Regrowth-free integration of injection locked slotted laser with an electroabsorption modulator”, Optics Express, 25 (4), pp. 4054-4060, Feb. 2017. DOI 10.1364/OE.25.004054
4. **N. P. Kelly**, M. Dernaika, L. Caro, P. Morrissey, A. Perrott, J. Alexander, F.H. Peters, “Regrowth-Free Single Mode Laser based on Dual Port Multimode Interference Reflector”, IEEE Photon. Tech. Lett, 29 (3) pp. 279-282, Feb. 2017. DOI 10.1109
5. L. Caro, **N. P. Kelly**, M. Dernaika, M. Shayesteh, P. Morrissey, J. Alexander and F.H. Peters “A Facetless Regrowth-Free Single Mode Laser Based on MMI Couplers”, Optics and Laser Technology 94, pp. 159–164, Sept. 2017 DOI: 10.1016/j.optlastec.2017.03.029
6. M. Dernaika, **N. P. Kelly**, L. Caro, and F. H. Peters, “Regrowth-free single mode semiconductor laser suitable for monolithic integration based on pits mirror”. Optical Engineering, 2017 (In the press).
7. P. E. Morrissey, **N. Kelly**, M. Dernaika, L. Caro, H. Yang and F. H. Peters, "Coupled Cavity Single Mode Laser based on Regrowth-Free Integrated MMI Reflectors", Photon. Tech. Lett., pp. 1313-1316, June 2016. DOI: 10.1109/LPT.2016.2541695
8. M. Dernaika, L. Caro, **N. P. Kelly**, J. K. Alexander, F. Dubois, P. E. Morrissey and F. H. Peters, “Deeply Etched Inner-Cavity Pit Reflector”, IEEE Photonics Journal, 9 (1), Feb. 2017. DOI:10.1109/JPHOT.2017.2656252
9. M. Dernaika, L. Caro, **N. P. Kelly**, and F. H. Peters, “Single facet semiconductor laser with deep etched V-notch reflectors integrated with an active multimode interference reflector” Journal of Modern optics, 2017, DOI: 10.1080/09500340.2017.1327621.
10. M. Dernaika, L. Caro, **N. P. Kelly** and F. H. Peters “Tunable L-band semiconductor laser based on Mach-Zehnder interferometer” Optics communications, 402 (56-59), 2017.

11. M. Shayesteh, K. Huet, I. Toqué-Tresonne, R. Negru, C.L.M Daunt, **N. Kelly**, R. Duffy, "Atomically Flat Low-Resistive Germanide Contacts Formed by Laser Thermal Anneal", IEEE Transactions on Electron Devices 60 (7), 2013.
12. K. Huet, M. Shayesteh, I. Toque-Tresonne, R. Negru, C. Daunt, **N. P. Kelly**, D. O'Connell, R. Yu, V.Djara, N. Ptkov and R. Duffy, "Laser thermal anneal formation of atomically-flat low-resistive germanide contacts", Phys. Status Solidi, No. 1, pp. 169-173, 2014.
13. H. Yang, P. Morrissey, W. Cotter, C. L. M. Daunt, J. O'Callaghan, B. Roycroft, Nan Ye, **N. Kelly**, B. Corbett, and F. H. Peters, "Monolithic Integration of Single Facet Slotted Laser, SOA, and MMI Coupler", IEEE Photon. Tech. Lett., 25 (3), pp. 257-260, 2013.

### Conference Proceedings

1. **N. P. Kelly**, M. Dernaika, L. Caro and F. H. Peters, "Monolithic CoWDM Transmitter Via Integration of Injection Locked Slotted Laser With Electroabsorption Modulator", European Conference on Lasers and Electro-Optics, Munich, 2017.
2. **N. P. Kelly**, P. E. Morrissey and F. H. Peters, "Monolithic Integration of Facetless Slotted Fabry-Perot Lasers and Star Coupler", European Conference on Integrated Optics, Warsaw, 2016.
3. **N. P. Kelly**, W. E. Cotter, P. E. Morrissey, R. Sheehan and F. H. Peters, "Dielectric Crossings for Simplified Photonic Integrated Circuit Testing", Photonics Ireland, Cork, Sept. 2015.
4. M. Dernaika, **N. P. Kelly**, P. E. Morrissey, L. Caro, H. Yang and F. H. Peters, "Single mode semiconductor lasers based on offset waveguides" Advances in Lasers II, Photon16, Leeds UK, Sept. 2016.
5. S. P. Duggan, **N. P. Kelly**, L. Caro, M. Dernaika, M. Shayesteh, J. Alexander, H. Yang, P. E. Morrissey, A. Gocalińska, K. Thomas, E. Pelucchi, and F. H. Peters, "Development of inverted p-substrate InP/AlGaInAs lasers for vertical integration with multiple passive or active intrinsic regions", European Conference on Integrated Optics, Eindhoven, 2017.
6. L. Caro, M. Dernaika, **N. P. Kelly**, P. Morrissey, H. Yang and F. Peters, "A facetless regrowth-free single mode laser based on multimode interference couplers and reflectors", P:07, Photon16, Leeds UK, Sept. 2016.
7. A.H. Perrott, L. Caro, M. Dernaika, **N. P. Kelly**, F. Dubois, and F.H. Peters, "Mutual Injection Locking of Lasers in a Photonic Integrated Circuit", IOP Spring Meet, Dublin, 2016.
8. A.H. Perrott, L. Caro, M. Dernaika, **N. P. Kelly**, P.E. Morrissey, and F.H. Peters, "Mutual Injection Locking of Lasers in a Photonic Integrated Circuit", European Conference on Integrated Optics, Eindhoven, 2017.

9. A. Perrott, P. Morrissey, F. Dubois, M. Dernaika, L. Caro, **N. Kelly** and F. Peters, "Injection locking behaviour of mutually coupled slotted Fabry-Pérot lasers integrated onto a single growth monolithic photonic integrated circuit", Photon16, Leeds UK, Sept. 2016.
10. M. Shayesteh, K. Shortiss, W. Cotter, P. E. Morrissey, Al. Perrot, **N. P. Kelly** and F. H. Peters, "De-multiplexing coherent optical combs within Photonic Integrated Circuits", European Conference on Integrated Optics, Eindhoven, 2017.
11. R. N. Sheehan, H. Yang, P. J. Marraccini, M. Q. Yang, F. Azzarello, **N. Kelly** and F. H. Peters, "Electroabsorption Modulator for High Performance Computing Architectures", Photonics Ireland, Cork, Sept. 2015.
12. P. Marraccini, P. Morrissey, M. Jezzini, M. Sadiq, H. Yang, M. Crowley, **N. Kelly**, Y. Li, L. Gao and F. H. Peters, "Phase Matched Transmission Line Design for High-Speed Optical Modulators", ISSC 2014, OS-2A.4, Limerick, June, 2014

# Introduction

## Motivation

In this communication age, consumer internet traffic continues to grow at an exponential rate year on year. As a result, communication networks need to be continually upgraded to keep up with ever increasing bandwidth demands. Diverse research is currently being undertaken at a global level to produce cost effective solutions to maximize network performance. One such area focuses on the development of photonic integrated circuits (PICs), which strives to replicate the same compact design and low power consumption achieved by integrated circuits in the electronics industry. However, photonic components are more complex and diverse than their electrical equivalents, such as transistors. As these components can have large footprints, involve multiple electrical contacts and require different material properties for optimal performance, the best approach is not obvious when cost is considered. While platforms such as heterogenous integration and monolithic regrowth have produced PICs with advance functionality, they rely on complex fabrication processes, which increase production time and cost. This thesis investigates the feasibility of a monolithic, regrowth free transmitter for long range telecommunications which requires less sophisticated fabrication techniques and would therefore be more cost effective to manufacture.

## Thesis Outline

This thesis consists of seven chapters. Chapter 1 beings with an overview of optical communications networks and a brief introduction into the avenues of research currently being undertaking to continually increase their capacity. It then describes the evolution of wavelength division multiplexing (WDM) in such systems, while exploring the properties of one of the newer forms: namely coherent wavelength division multiplexing. Finally, the concept of photonic integrated circuits to reduce cost and power consumption of transmitters and receivers is introduced.

In Chapter 2, photonic integrated circuits are discussed in detail. The fundamental properties of semiconductive materials, which makes them suitable for such

applications are examined as well as the processes involved in the production of multiple quantum well structures. Since there is a difference in the optimal material properties of lasers and modulators for given wavelength, the pros and cons of various integration formats are also summarized. The chapter concludes by proposing a novel monolithic regrowth free photonic integrated circuit for use as a coherent WDM transmitter suitable for long range communications.

Chapter 3 describes the design and fabrication processes that were undertaken as part of this thesis. This begins with a review of current design software packages and a discussion on the development of a process which utilizes a composite hard mask to integrate rib and ridge waveguide structures. This is followed by a detailed description of the DC and High-Speed processes which were employed to fabricate the devices and circuits, as discussed in later chapters.

Utilizing the composite hard mask process, an integratable laser, which is based on the self-imaging properties of propagating multimode waves and total internal reflection is developed in Chapter 4. The work includes an investigation of the effect of various slot types on a laser's output spectrum and the characterization of single port and dual port multimode interference reflector test structures on indium phosphide. This laser design offers multiple advantages such as UV compatible lithography, regrowth free and does not require a cleaved facet to lase.

Chapter 5 outlines the integration of core components required for the WDM transmitter proposed in Chapter 2. A PIC consisting of couplers, splitters, lasers and DC modulators is fabricated and characterized. The feasibility of integrating a laser with an EAM by means of injection locking is also verified by producing a 2.5 Gbps open eye diagram. It is concluded that the high-speed performance of these PICs can be improved by using more advanced modulator designs.

Following the conclusions drawn in the previous chapter, high speed modulators are investigated in Chapter 6 with the aim of to increase the data rate of the developed PICs. This includes a discussion on lumped and traveling wave electrode designs as well as optimal epitaxial structures. A range of lumped modulators are then



## Introduction

designed and characterized. A curved modulator suitable for heterogeneous integration using flip chip packaging was also developed.

To conclude, chapter 7 summarises the main points of this thesis and proposes future work to continue development towards a monolithic regrowth-free WDM transmitter. These include the addition of a pre-existing comb source design to the developed PIC, and integration of the characterized high-speed modulator designs. Finally, the number of optical carriers can be increased by adding additional arms to the current design.



# Chapter 1

## Optical Communications

### 1.1 Introduction

The invention of the internet has changed how the world communicates with the advent of applications such as high-speed internet access, multimedia broadcast systems and high capacity remote storage. This shift has been driven by the circular trend whereby increases in available bandwidth result in a reduction in the price per bit of transmitted data, which in turn increases customer demand and the need to develop new technologies to further increase the bandwidth. Industrial analysts have concluded that the global consumer internet traffic has risen by a factor of five in the last 5 years with similar trends likely to continue as areas such as high definition video streaming, internet of things (IOT) and immersive experiences continue to grow [1] as illustrated in Figure 1.1.

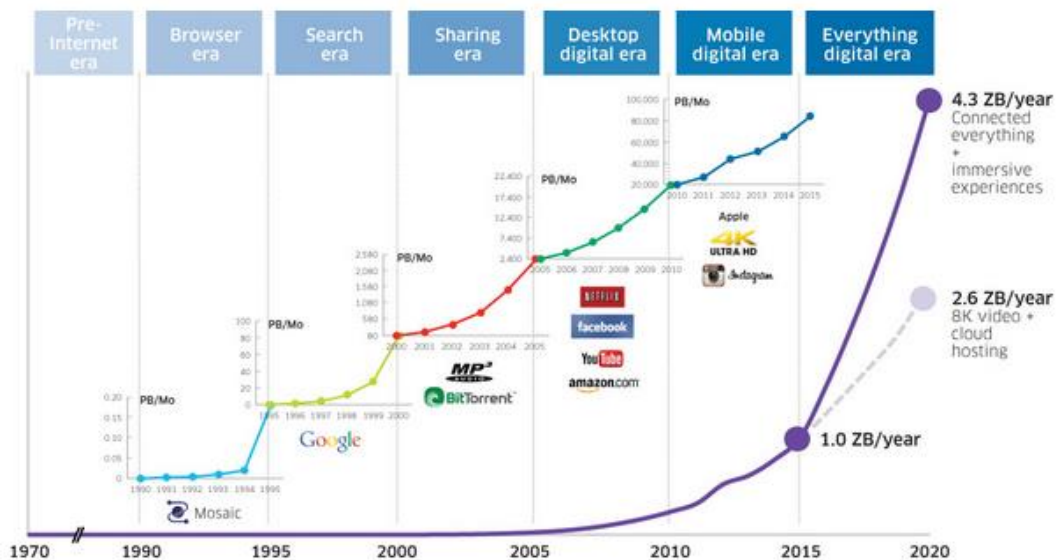
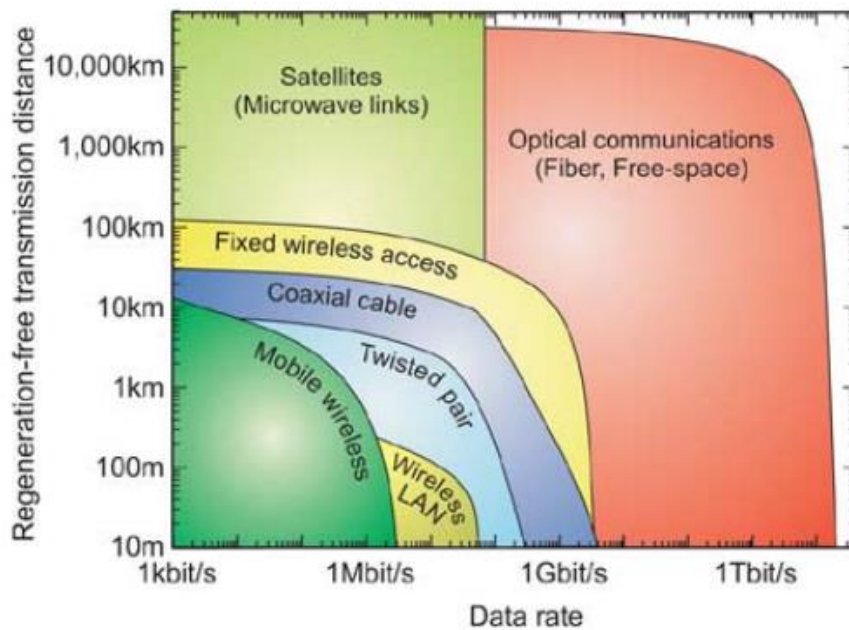


Fig 1.1: Data transfer projections to 2020. [1]

Several communications technologies are used to address the widely different bandwidth demands of various applications in a cost-effective way, each with their own advantages and limitations. One way of comparing these technologies is to

quantify their maximum supportable data rates and regeneration free transmission distances which is defined as the distance that can be bridged without detecting and retransmitting the digital information, as shown in Figure 1.2. Optical communications can support Tb/s capacities over thousands of kilometres, making it an ideal technology base for high capacity data transfer. As a result, almost any network based services will at some point involve the conversion of data into a modulated optical signal traveling down a network of optical fibres. The inventions of the ruby laser [2], which provided an optical signal that could be modulated to encode information, and low loss optical fibre [3] were the first two breakthroughs in fibre-based communication systems. With these two technologies, it became feasible to transmit optical signals across significant distances.



**Fig 1.2:** Regeneration-free transmission distance versus data rate for various communication technologies [4].

Subsequent research yielded numerous technological advancements such as low loss optical filters and optical amplifiers for lasers operating at the low loss portion of the fibre. Erbium doped fibre amplifiers (EDFAs) [5] and Raman amplification enabled transmission over increasing long distances by providing low-noise, high-gain response over a wide range of transmission wavelengths. The resultant modern optical networks can be divided into three categories: core networks, metropolitan

area networks (MAN) and access networks. Core networks primarily focus on long haul point-to-point data transfer but networking capabilities can be included with the addition of optical cross connects and optical add drop multiplexers. MAN refers to the interconnection of networks in a geographic area such a city into a single larger network, offering efficient connection to the core network. Access networks provide the final connection to the end user. This can be achieved using copper wire or optical approaches such as fibre to the home (FTTH).

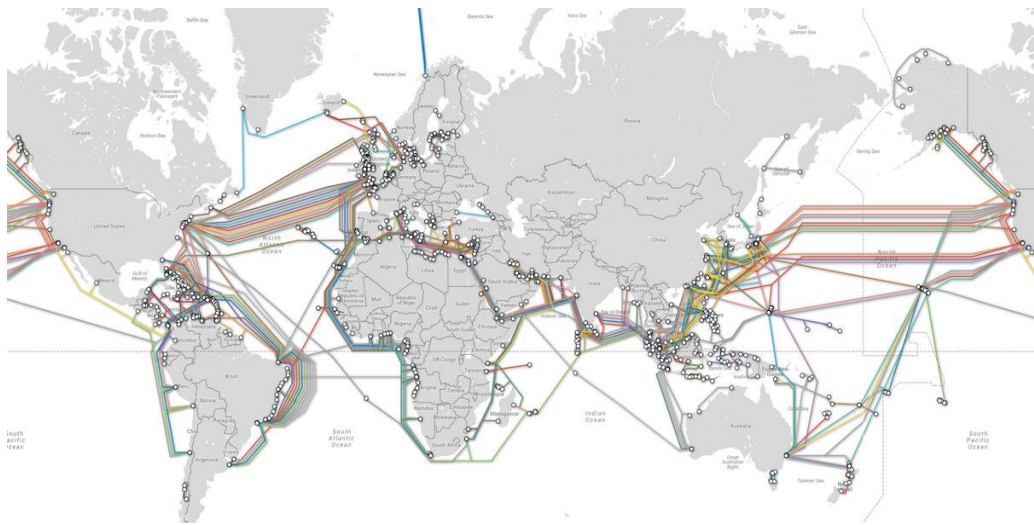


**Fig 1.3:** Undersea cables connecting the world's core networks [6].

The constant need to increase the data transfer rate of the core networks is hindered by the limited transmission bandwidth of optical fibres due to a combination of Rayleigh scattering, water absorption and the infrared absorption of silica [7]. One solution for increasing bandwidth focuses on improving existing long-haul networks for transport of larger capacities by the development of advanced optical fibres with wider transmission bandwidths. However, an extensive network of submarine cables has been installed to allow communications between countries (Figure 1.3), facilitating global communication. The total length of all currently installed optical fibres is estimated to be approximately two billion kilometres and upgrading these cables is both difficult and expensive [8]. Therefore, such a radical change to the existing infrastructure would only be adopted if it provided ground breaking improvements, resulting in a substantial increase in revenue. A second shorter term solution to the capacity demand is to maximize the data rate of the

existing infrastructure by focusing on advancements in the design of the transmitters and receivers. The ideal solution would yield a simple transmitter and receiver configuration which is spectrally efficient and has a high tolerance for fibre induced impairments and inter channel crosstalk. However, due to inherent limitations that will be discussed in the following sections, there are unavoidable trade-offs which must be made.

## 1.2 Wavelength Division Multiplexing

Wavelength division multiplexing involves the transmittance of multiple optical carriers simultaneously along an optical fibre at different wavelengths. Each wavelength is independently modulated and multiplexed to form one signal which is launched into the optical fibre. At the receiver end, the signal is demultiplexed into its individual carriers and the data is recovered. The primary advantage of WDM is that it facilitates large increases in data transfer rates without the need to upgrade the existing optical fibre network. The usage of WDM for optical communications was first proposed in 1970 [9] and WDM systems were widely implemented during the 90's [10],[11], fuelled by the ever-increasing demand for bandwidth intensive applications. The quantity of information which can be transferred over a given bandwidth in a communication system can be quantified by its information spectral density (ISD).

$$ISD = \frac{\textit{Total Capacity}}{\textit{Total Occupied Bandwidth}} = \frac{\textit{No. of Channels} \times \textit{Bit rate}}{\textit{Total Occupied Bandwidth}}$$

This equation demonstrates that the data transfer rate of a WDM signal can be improved by increasing the number of wavelengths in the fibre or by increasing the bit rate of the carriers in the system. However, increasing either of these values comes at a cost, either in terms of the technology required or the degradative effects which must be accounted for. The primary impairment that limits the increase in the ISD of WDM systems is crosstalk between neighbouring carriers as they propagate through the optical fibre, which increases the error rate. Increasing the data rate broadens the spectral width of a channel while adding extra channels provides less space between channels. Both of these cases can potentially lead to

increased crosstalk. Such crosstalk can be minimized by maintaining wide guard bands in-between the channels, but this negatively affects the maximum ISD of a system.

### 1.3 Dispersion and Non-Linear Effects

Singled mode sources are implemented in WDM systems due to reduced dispersion penalties. Chromatic dispersion is the wavelength dependence of a material's refractive index, resulting in carriers of different wavelengths traveling at different speeds as they propagate. This dispersion can cause pulses to spread and overlap within an optical fibre, increasing the bit error rate (BER) of the signal. The dispersion limited fibre distance for a non-return-to-zero (NRZ) signal can be expressed as a function of the speed of light ( $c$ ), the linear material dispersion coefficient ( $D$ ), the wavelength ( $\lambda$ ) and the carrier baud rate ( $B$ ) [12].

$$L = \frac{c}{2D\lambda^2 B^2}$$

Assuming  $D$  to be approximately 10ps/nm-km in standard single mode fibre, the maximum transmission distance for 10 and 40 Gb/s signals are calculated as 63.5 and 4 km respectively, highlighting the significance of this effect [13].

Polarisation mode dispersion (PDM) is a form of modal dispersion where two orthogonally polarised components of a mode will travel at different speeds due to random defects in the waveguide. These deformity induced birefringences result in the spreading of optical pulses due to the different refractive indices experienced by the two polarisations. PMD can prove difficult to compensate for as it varies randomly with time, wavelength, and is different for each individual fibre. This issue becomes increasing problematic as the bit rate increases because the pulse spreading effect of PDM increases as the pulse width becomes shorter [14].

$$B_m = |n_x - n_y|$$

The modal birefringence of a fibre for a given wavelength ( $B_m$ ) can be expressed as the absolute differential of the two refractive indices ( $n_x, n_y$ ) and is typically in the order of  $10^{-7}$  [15].

The quality of an optical signal is often quantified by its optical signal to noise ratio (OSNR). The launched signal must be transmitted at high power to maximise this OSNR value. This can prove problematic however, as non-linear effects begin to impact the systems performance at these high launch powers. A dominant non-linear effect known as the Kerr effect occurs when high signal power interacts with bound electrons, resulting in a phase shift of the optical field due to changes in the refractive index [15].

$$\tilde{n} = n + n_2 \frac{P}{A_{eff}}$$

A material's intrinsic material properties and therefore the electronic nonlinearities are summarised by its electric susceptibility coefficients. Since silica is a perfect centro-symmetric medium, its nonlinear effects are determined by  $\chi^{(3)}$  only and can be represented in terms of a refractive index ( $n_2$ ). Therefore, the refractive index experienced by a high-powered signal ( $\tilde{n}$ ) can be expressed as a function of the signal power (P), the effective area of the fibre  $A_{eff}$  and  $n_2$  which is also known as the Kerr coefficient. The Kerr effect can induce multiple impairments such as self-phase modulation, four wave mixing and cross phase modulation which all become more evident at increasing bit rate [16].

#### 1.4 Traditional WDM

Traditional WDM systems are divided into three different formats: binary WDM, coarse WDM and dense WDM. These formats are all based on the same concept of using multiple carriers at different wavelengths propagating through a single fibre, but differ in the spacing and number of channels as well as the applicable amplification technologies. Another common factor to these formats is that the optical power of each of the channels is created by discrete optical sources as in Figure 1.4. As previously discussed, this requires the application of a minimum carrier spacing to minimize inter-channel crosstalk due to the in-coherence of the light sources and potential wavelength drifting.

Binary WDM uses only two wavelengths at 1310nm and 1550 nm and therefore has a very limited ISD. According to current international telecommunication union (ITU)



standards, coarse WDM utilises channels ranging from 1271 nm to 1611 nm with a wavelength spacing of 20 nm [17]. As coarse WDM has a bandwidth which is incompatible with EDFAs, its use is restricted to metropolitan applications. An advantage of coarse WDM over dense WDM however is that its wide channel spacings facilitate the use of less sophisticated and therefore cheaper transceivers. Dense WDM refers to the compact multiplexing of optical signals in the C band (1530 nm to 1565m) to take advantage of the properties of EDFAs for long range data transfer.

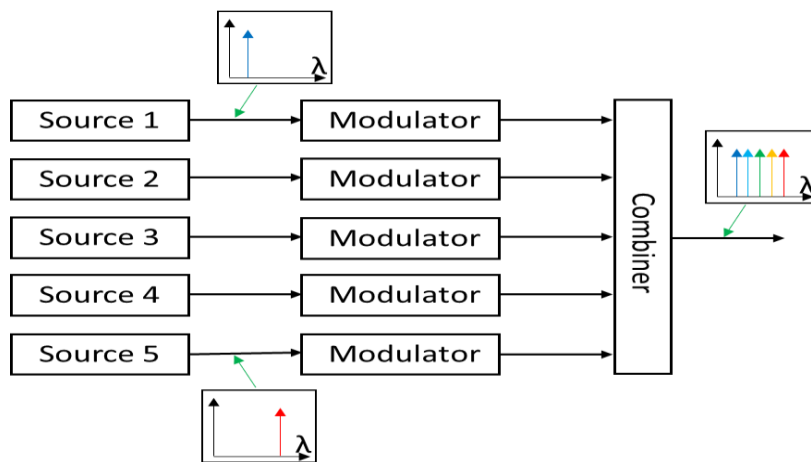


**Fig 1.4:** Schematic of traditional WDM transmitter.

Dense WDM formats vary but a typical (fully implemented) system is composed of either 40 channels at 100 GHz spacing or 80 channels at 50 GHz spacing [18]. The addition of Raman amplification has increased the number of useable wavelength into the L-band (1565nm-1625nm), effectively doubling the number of useable channels.

### 1.5 Coherent WDM

As previously discussed, inter channel crosstalk in standard WDM systems occurs when two channels are closely spaced. This interference is chaotic when independent lasers are used for each channel as their phases are incoherent. Techniques such as transmitter pre-filtering or polarisation multiplexing can be applied to limit this interference [19]. However, if the phase difference between the channels is controlled, the interference can become deterministic. For example, if a series of closely spaced coherent channels of equal amplitude are used, a periodic

pulse train is produced. The variation in power of this pulse train can be expressed as a function of the number of channels (N) and the frequency of the spacing ( $\omega$ ). Crucially, if the period of this train (T) is an integral multiple of the bit period used, the pulse peak always occurs at the same point within a bit [20].

$$P \propto \frac{\sin^2\left(\frac{N\omega t}{2}\right)}{\sin^2\left(\frac{\omega t}{2}\right)}$$

$$T = \frac{2\pi}{\omega}$$

Advanced control of the relative phase of the carriers can be used to increase or decrease an eye opening using the pulse train. This phase control of the channels is the fundamental principle of coherent WDM. Coherent WDM is conceptually similar to orthogonal frequency division multiplexing (OFDM), which is used to increase spectral efficiency in the electrical domain. As a result, coherent WDM is also referred to as all optical OFDM. However, the bandwidth of the transceivers used in electrical OFDM systems must scale with the data rate as multiplexing and demultiplexing occurs in the electrical domain using digital signal processing (DSP) [21]. This means that the bandwidth of the transceivers used must scale with the data rate of the OFDM system. In the case of CoWDM however, since the sub-channels are modulated, multiplexed and demultiplexed in the optical domain the operating speed of the transceivers only scale with the sub channel bit rate resulting in a much larger potential bandwidth.

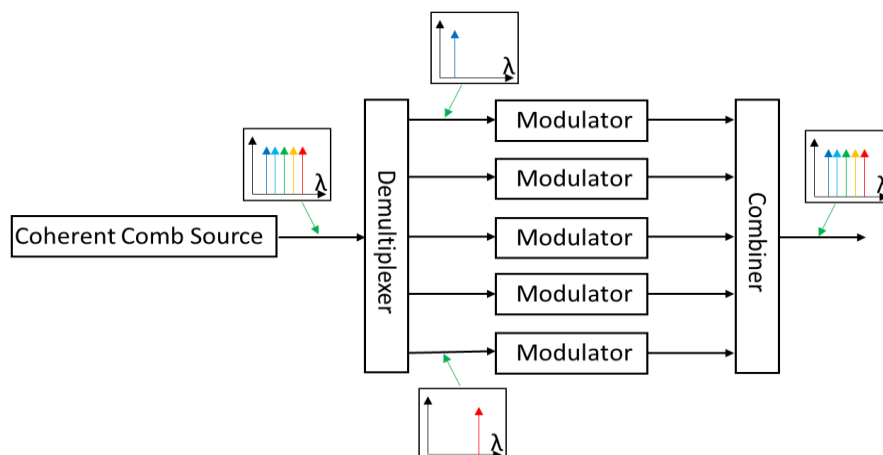


**Fig 1.5:** Schematic of coherent WDM transmitter.

Due to the pulse train considerations described above, it is necessary to have optical channels which are spaced by a specific frequency and have a stable inter channel phase relationship. One approach to achieve coherent optical channels is to demultiplex, modulate and multiplex the lines of a coherent optical comb (Figure 1.5). There has been extensive work published on the production of these coherent optical combs for a wide variety of applications in addition to coherent WDM. Such techniques included the amplitude or frequency modulation of mode-locked lasers [22] or fibre ring lasers [23] which provide suitable channel spacings for WDM applications but require precise control of the laser cavity length, significantly increasing the system's complexity. A wide band  $\text{LiNbO}_3$  phase modulator arranged in such a way that it is driven with a feedback signal from its output has been shown to produce a 10-channel optical comb with 9.95 GHz channel spacing [24]. While this method is easier to maintain than mode-locked lasers, it requires large RF power amplifiers with precise control of the output voltage for the feedback loop. It is also possible to create an optical comb using two cascaded MZMs which are driven by sinusoidal electrical waves [25]. Each modulator will create a set of side bands whose spacing can be adjusted by varying the applied RF frequency. Nine optical sidebands with a spacing of 12.5 GHz and intensity uniformity within 2 dB have been demonstrated using this approach. It is also possible to cascade components such as phase modulators (PM) or a combination of PMs and MZMs to achieve similar results. Finally, comb generation is also achievable by injection locking a gain switched Fabry-Pérot laser. An optical comb consisting of eight clearly resolved 10 GHz sidebands within a 3 dB envelope peak has been reported using such a technique demonstrating tunability over the entire C band [26]. Further expansion of the comb was achieved with the aid of an optical phase modulator, resulting in near doubling of comb tones as seen in Figure 1.6.

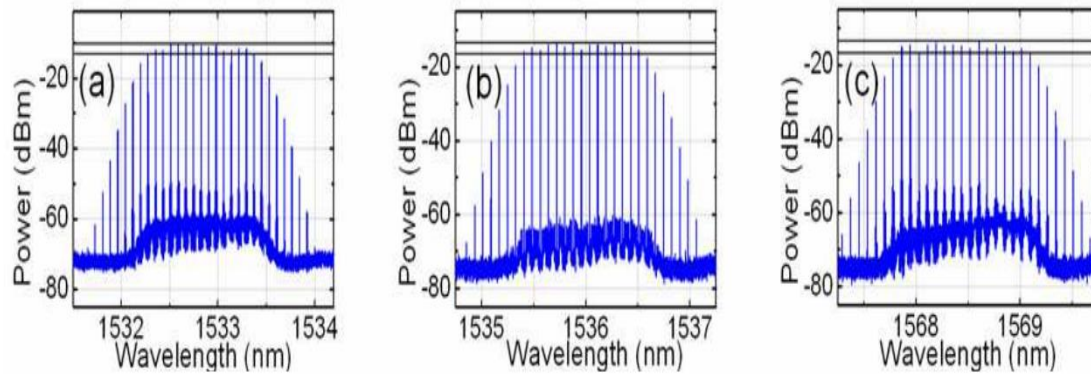


**Fig 1.6:** Optical combs consisting of between 14 and 16 tones which are expanded via phase modulation [26].

### 1.6 Modulation Formats

In single mode fibres, the optical field has three properties which can be used to carry encoded information: intensity, phase and polarisation. A wide range of modulation formats have been developed for use in optical communication systems and will be briefly discussed in this section. Amplitude shift keying (ASK) encodes data on an optical carrier by modulating the intensity. Direct detection using a photodiode is performed at the receiver to recover the encoded data. On-Off keying (OOK) is the simplest case of ASK modulation where no carrier is present during the transmission of a zero while a second symbol is found at a finite amplitude, resulting in a one bit per symbol format [27]. Two common version of ASK are non-return-to-zero (NRZ) and return-to-zero (RZ) OOK, both are show in Figure 1.7 below. NRZ-OOK maintains an on state for the entire bit period and its amplitude remains constant for two consecutive identical bits. RZ-OOK consists of optical pulses which are shorter than the bit period so that the amplitude returns to zero at the end of every bit slot. While RZ-OOK has superior tolerance to single channel nonlinear effects, NRZ-OOK is less susceptible to dispersion and therefore more suitable for closely spaced WDM systems [28].

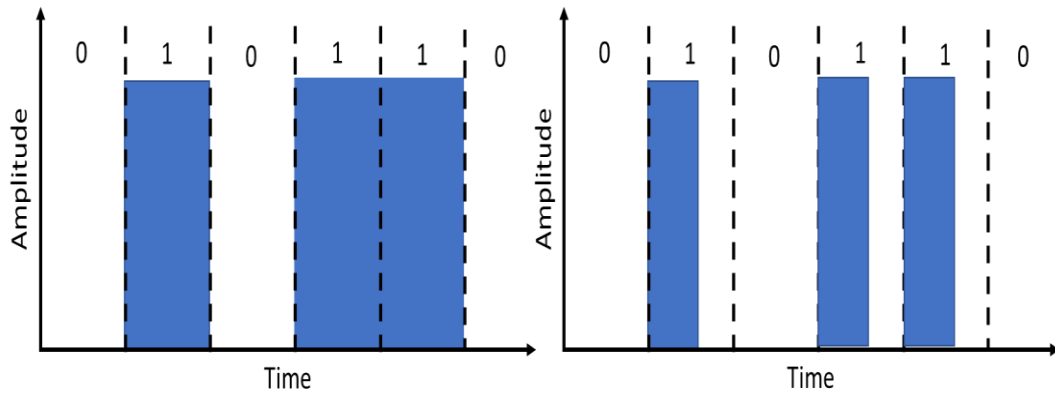


**Fig 1.7:** NRZ-OOK (left) and RZ-OOK (right) modulation formats.

A more sophisticated binary modulation format is known as binary phase shift keying (BPSK). Phase shift keying (PSK) is a modulation scheme which maintains the amplitude of the carrier but encodes the information in the optical phase instead [29]. BPSK consists of two symbols with identical amplitudes which are separated by a  $\pi$  phase difference. This format is the most robust of the PSK formats as it takes the highest level of noise or distortion to create an error, but is only able to modulate at 1 bit per symbol. It is also less susceptible to non-linear effects present in an optical system than OOK due to its lower overall peak power. Since it is not currently possible to detect absolute phase, it is common to use the phase of the preceding bit as a reference for demodulation. This results in differential phase shift keying (DPSK) whereby the information is carried in the optical phase change of the bits [30].

Polarisation shift keying (PoSK) is the transfer of data by switching the polarisation of a carrier between two orthogonal states to produce a modulated signal [31]. However, polarisation mode dispersion and fibre non-linearities limit the performance of such a modulation format. As a result, polarisation is more often used to reduce impairments such as inter channel crosstalk by transmitting signals in orthogonal polarisations, enhancing the ISD of the system. Typically, modulation states are represented on a constellation diagram as shown in Figure 1.8 [32]. These diagrams allow for a straight forward visualization of possible symbols that may be selected by a given modulation scheme by representing them as complex points on a two-dimensional scatter diagram. The real and imaginary axis are often referred to

as the in-phase (I) axis and the quadrature (Q) axis respectively. Measured constellation diagrams can be used to identify the types of interference which are distorting a given signal. For example, attenuation causes the corner points to move towards the centre while phase noise results in a rotationally spreading of the points.

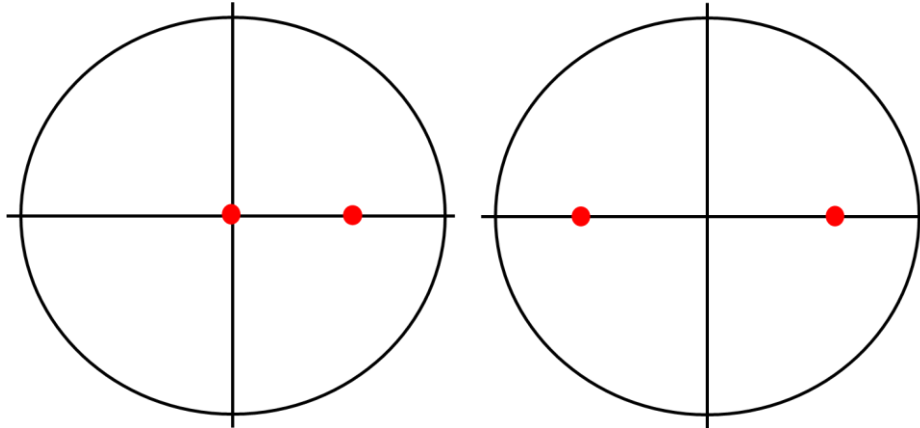


**Fig 1.8:** OOK (left) and BPSK (right) modulation formats.

One method of increasing the data rates of an optical system is the use of advanced modulation formats, which offer a higher bit per symbol ratio and therefore a higher bit rate. Pulse-amplitude modulation (PAM) is a form of ASK modulation where the amplitudes of a train of carrier pulses are varied according to the sample value of the message signal [33]. While the number of possible pulse amplitudes in analog PAM is theoretically infinite, possible digital PAM amplitudes are reduced to some power of two. For example, in PAM4 there are  $2^2$  discrete amplitudes. Quadrature phase shift keying (QPSK) is an enhancement of BPSK, offering four points on a constellation diagram, equispaced around the circle [34]. These points correspond to four phase shifts of  $0$ ,  $\frac{\pi}{2}$ ,  $\pi$  and  $\frac{3\pi}{2}$  to encode two bits per optical symbol (Figure 1.9). PSK formats with higher symbol rates such as 8PSK are possible but suffer from increasing error rates.

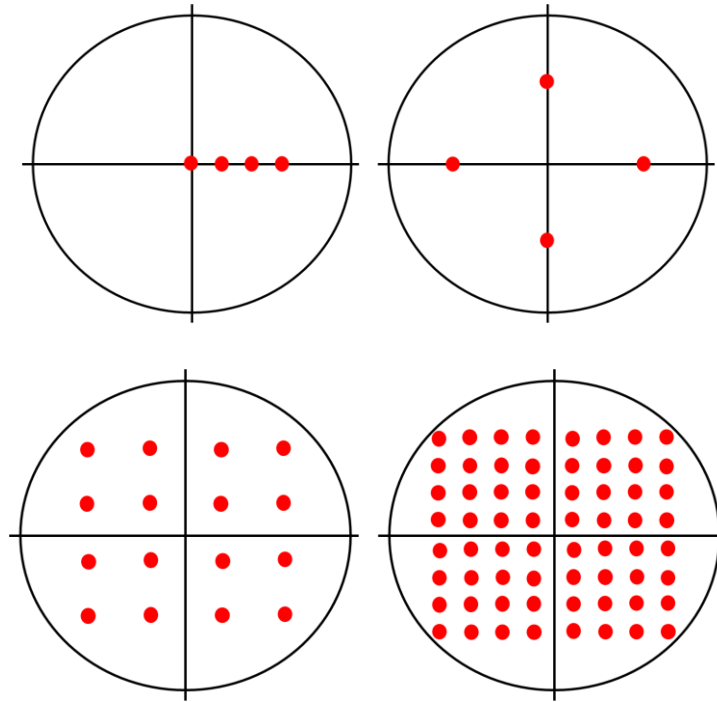


**Fig 1.9:** PAM4 (top left) QPSK (top right) 16QAM (bottom left) and 64QAM (bottom right) modulation formats.

Quadrature amplitude modulation (QAM) conveys data by changing the amplitude of two waves of equal frequency which are  $\frac{\pi}{2}$  out of phase with each other [35]. Amplitude modulating two carriers in quadrature can be equated to modulating both the amplitude and phase of a single carrier. A variety of forms of QAM exist such as QAM16 and QAM64, which provide increased bit per symbol ratios for optical fibre systems. QAM constellations can be constructed in many ways such as square, rectangular and non-square layouts. While rectangular constellations can be comparatively easily demodulated, they are not as spectrally efficient as square constellations. Non-square constellations achieve marginally better bit-error rates, but they are harder to modulate and demodulate.

**Table 1.1:** Summary of bit rates of different modulation formats.

Modulation	Bits Per Symbol	Symbol Rate
OOK	1	bit rate
BPSK	1	bit rate
QPSK	2	0.50 x bit rate
PAM4	2	0.50 x bit rate
16QAM	4	0.25 x bit rate
64QAM	6	0.16 x bit rate

## 1.7 Photonic Integration

Significant focus has been directed towards the integration of multiple discrete optical components into a single device, drawing inspiration from the electronics world. The research into such integration techniques is driven by the many potential benefits such as reduced cost, greater reliability, and lower power consumption. Despite the first photonic integrated circuit (PIC) being proposed in 1969 [36] it is only in the last 15 year that PICs have been realised for commercial applications [37]. This research has yielded dense circuitry such as an InP based monolithic tuneable optical router (MOTOR) consisting of eight Mach-Zehnder modulators (MZMs), semiconductor optical amplifiers (SOAs) and a passive arrayed-waveguide grating (AWG) router [37], shown in Figure 1.10. In light of this, semiconductor devices and integrated circuits for use in coherent WDM systems will be discussed in detail in the next chapter.

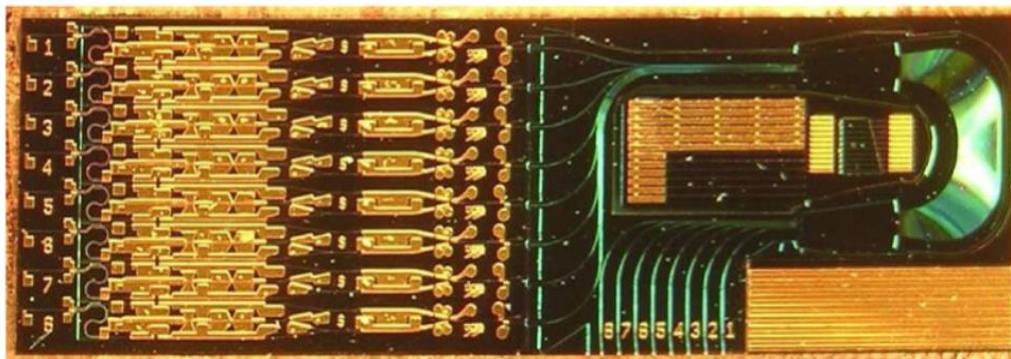


**Fig 1.10:** Photograph of fabricated MOTOR chip [38].

### Bibliography

- [1] “Big changes—again—for cable operators’ business | Insight | Nokia.” [Online]. Available: <https://insight.nokia.com/big-changes-again-cable-operators-business>. [Accessed: 22-May-2017].
- [2] T. H. MAIMAN, “Stimulated Optical Radiation in Ruby,” *Nature*, vol. 187, no. 4736, pp. 493–494, Aug. 1960.
- [3] F. P. Kapron, D. B. Keck, and R. D. Maurer, “RADIATION LOSSES IN GLASS OPTICAL WAVEGUIDES,” *Appl. Phys. Lett.*, vol. 17, no. 10, pp. 423–425, Nov.



1970.

- [4] P. J. Winzer and R.-J. Essiambre, "Advanced Optical Modulation Formats," *Proc. IEEE*, vol. 94, no. 5, pp. 952–985, May 2006.
- [5] R. J. Mears, L. Reekie, I. M. Jauncey, and D. N. Payne, "Low-noise erbium-doped fibre amplifier operating at 1.54 $\mu$ m," *Electron. Lett.*, vol. 23, no. 19, p. 1026, 1987.
- [6] "Bandwidth explosion: As Internet use soars, can bottlenecks be averted? | Ars Technica." [Online]. Available: <https://arstechnica.com/business/2012/05/bandwidth-explosion-as-internet-use-soars-can-bottlenecks-be-averted/>. [Accessed: 22-May-2017].
- [7] "Fibercore - Fibercore Fiberpedia - Attenuation." [Online]. Available: <http://fibercore.com/fiberpedia/attenuation>. [Accessed: 22-May-2017].
- [8] P. J. Winzer, "Scaling Optical Fiber Networks: Challenges and Solutions," *Opt. Photonics News*, vol. 26, no. 3, p. 28, Mar. 2015.
- [9] O. E. DeLange, "Wide-band optical communication systems: Part II— Frequency-division multiplexing," *Proc. IEEE*, vol. 58, no. 10, pp. 1683–1690, 1970.
- [10] E. Lowe, "Current European WDM deployment trends," *IEEE Commun. Mag.*, vol. 36, no. 2, pp. 46–50, 1998.
- [11] A. R. Chraplyvy *et al.*, "One-third terabit/s transmission through 150 km of dispersion-managed fiber," *IEEE Photonics Technol. Lett.*, vol. 7, no. 1, pp. 98–100, Jan. 1995.
- [12] P. Henry, "Lightwave primer," *IEEE J. Quantum Electron.*, vol. 21, no. 12, pp. 1862–1879, Dec. 1985.
- [13] B. Clesca, S. Gaudhard, C. Coeurjolly, J.-P. Thiery, L. Pierre, and L. Berthelon, "The WDM answer to line-rate increase within the terrestrial fiber-based networks," in *Proceedings of GLOBECOM'96. 1996 IEEE Global*

- Telecommunications Conference*, vol. 3, pp. 1925–1929.
- [14] M. Brodsky, N. J. Frigo, M. Boroditsky, and M. Tur, “Polarization Mode Dispersion of Installed Fibers,” *J. Light. Technol.*, vol. 24, no. 12, 2006.
- [15] G. P. (Govind P. . Agrawal, *Fiber-optic communication systems with cd*. Wiley, 2010.
- [16] L. Paradiso, P. Boffi, L. Marazzi, N. D. Vecchia, M. Artiglia, and M. Martinelli, “Experimental XPM, SPM, FWM penalty evaluation in very dense WDM optical systems,” in *(CLEO). Conference on Lasers and Electro-Optics, 2005.*, 2005, p. 1339–1341 Vol. 2.
- [17] “G.694.2 : Spectral grids for WDM applications: CWDM wavelength grid.” [Online]. Available: <http://www.itu.int/rec/T-REC-G.694.2-200312-I>. [Accessed: 11-May-2017].
- [18] “Index of /downloads/DWDM ITU Table - 100 GHz.pdf.” [Online]. Available: <http://www.telecomengineering.com/downloads/>. [Accessed: 11-May-2017].
- [19] A. D. Ellis, F. C. G. Gunning, and T. Healy, “Coherent WDM: the achievement of high information spectral density through phase control within the transmitter,” in *2006 Optical Fiber Communication Conference and the National Fiber Optic Engineers Conference*, 2006, p. 3 pp.
- [20] A. D. Ellis and F. C. G. Gunning, “Spectral density enhancement using coherent WDM,” *IEEE Photonics Technol. Lett.*, vol. 17, no. 2, pp. 504–506, Feb. 2005.
- [21] J. Zhao, A. D. Ellis, F. C. G. Gunning, S. K. Ibrahim, and P. Frascella, “Multi-carrier systems for high-capacity transmission,” in *2009 14th OptoElectronics and Communications Conference*, 2009, pp. 1–2.
- [22] T. Healy, F. C. Garcia Gunning, A. D. Ellis, and J. D. Bull, “Multi-wavelength source using low drive-voltage amplitude modulators for optical communications,” *Opt. Express*, vol. 15, no. 6, p. 2981, 2007.
- [23] S. Yamashita and G. J. Cowle, “Bidirectional 10-GHz optical comb generation

- with an intracavity fiber DFB pumped Brillouin/erbium fiber laser," *IEEE Photonics Technol. Lett.*, vol. 10, no. 6, pp. 796–798, Jun. 1998.
- [24] T. Sakamoto, T. Kawanishi, and M. Izutsu, "Optoelectronic oscillator using a LiNbO<sub>3</sub> phase modulator for self-oscillating frequency comb generation."
- [25] M. Fujiwara, M. Teshima, J. Kani, H. Suzuki, N. Takachio, and K. Iwatsuki, "Optical carrier supply module using flattened optical multicarrier generation based on sinusoidal amplitude and phase hybrid modulation," *J. Light. Technol.*, vol. 21, no. 11, pp. 2705–2714, Nov. 2003.
- [26] R. Zhou, S. Latkowski, J. O'Carroll, R. Phelan, L. P. Barry, and P. Anandarajah, "40nm wavelength tunable gain-switched optical comb source," *Opt. Express*, vol. 19, no. 26, p. B415, Dec. 2011.
- [27] S. Jawla and R. K. Singh, "Different Modulation Formats Used In Optical Communication System," *IOSR J. Electron. Commun. Eng.*, vol. 8, no. 4, pp. 2278–8735.
- [28] Y. Frignac, S. Bigo, and J.-P. Hamaide, "NRZ versus RZ format in Nx40 Gbit/s WDM terrestrial transmission systems with high spectral efficiency of 0.4 bit/(s.Hz)," in *Proceedings 27th European Conference on Optical Communication (Cat. No.01TH8551)*, vol. 4, pp. 524–525.
- [29] A. H. Gnauck and P. J. Winzer, "Optical phase-shift-keyed transmission," *J. Light. Technol.*, vol. 23, no. 1, pp. 115–130, 2005.
- [30] A. Tzanakaki, I. Zachropoulos, D. Parcharidou, and I. Tomkos, "Performance optimization using advanced modulation formats in WDM metropolitan area networks," in *Proceedings of 2004 6th International Conference on Transparent Optical Networks (IEEE Cat. No.04EX804)*, pp. 81–86.
- [31] A. Carena, V. Curri, R. Gaudino, N. Greco, P. Poggiolini, and S. Benedetto, "Polarization modulation in ultra-long haul transmission systems: a promising alternative to intensity modulation," in *24th European Conference on Optical Communication. ECOC '98 (IEEE Cat. No.98TH8398)*, vol. 1, pp. 429–430.

- [32] A. S. Tanenbaum and Andrew, *Computer networks*. Prentice Hall PTR, 2003.
- [33] J. Man, W. Chen, X. Song, and L. Zeng, "A Low-Cost 100GE Optical Transceiver Module for 2km SMF Interconnect with PAM4 Modulation," in *Optical Fiber Communication Conference*, 2014, p. M2E.7.
- [34] R. A. Griffin and A. C. Carter, "Optical differential quadrature phase-shift key (oDQPSK) for high capacity optical transmission," in *Optical Fiber Communication Conference and Exhibit*, pp. 367–368.
- [35] A. H. Gnauck, C. R. Doerr, L. L. Buhl, M. Magarini, and P. J. Winzer, "Spectrally Efficient Long-Haul Optical Networking Using 112-Gb/s Polarization-Multiplexed 16-QAM," *J. Light. Technol. Vol. 28, Issue 4*, pp. 547-556, vol. 28, no. 4, pp. 547–556, 2010.
- [36] S. E. Miller, "Integrated Optics: An Introduction," *Bell Syst. Tech. J.*, vol. 48, no. 7, pp. 2059–2069, Sep. 1969.
- [37] J. Rahn *et al.*, "250Gb/s real-time PIC-based super-channel transmission over a gridless 6000km terrestrial link," in *Optical Fiber Communication Conference and Exposition (OFC/NFOEC)*, 2012.
- [38] B. Jevremović, D. J. Blumenthal, E. Lively, L. A. Coldren, M. L. Mašanović, and S. C. Nicholes, "An 8 x 8 InP Monolithic Tunable Optical Router (MOTOR) Packet Forwarding Chip," *J. Light. Technol. Vol. 28, Issue 4*, pp. 641-650, vol. 28, no. 4, pp. 641–650, 2010.

## Chapter 2

# Photonic Integrated Circuits

### 2.1 Introduction

Photonic integrated circuits involve the integration of a range of optoelectronic devices such as lasers, modulators, amplifiers, splitters and filters to create a cost-effective solution for applications such as long haul optical communications. However, this integration has proven to be more difficult to achieve than electronic ICs due to the comparatively diverse and complicated component design. The primary difficulty centres around the difference in optimal material for active sections such as lasers and amplifiers and components like waveguide sections and phase based modulators which favour a passive medium. For semiconductor materials, the difference between active and passive regions is largely defined by the band structure. This chapter will introduce semiconductor based technologies including epitaxial structures and the fundamental operation of key devices such as lasers and modulators before discussing various integration formats. It will conclude by proposing a novel monolithic transmitter design for use in a CoWDM network.

### 2.2 Semiconductor Based Technology

From quantum mechanics, electrons from isolated atoms can have only discrete energy values, with these allowed energy values being calculable by solving Schrodinger's equation using the appropriate energy potentials. However, as the spacing between atoms is reduced, their orbitals begin to overlap. Each atomic orbital splits into numerous molecular orbitals corresponding to the number of atoms in the crystal due to the Pauli Exclusion Principle [1]. Since the number of atoms in a crystalline structure can be extremely large, the molecular orbitals become densely packed and can be considered as a continuous band. The two bands of interest are the conduction and valence bands. The valence band is the highest set of energy levels in which electrons are present at 0 K, while the conduction band is the first group of levels which are entirely empty at 0 K. Above 0 K, some electrons

have sufficient thermal energy to transition to the conduction band creating holes (missing electrons) in the valence band. Both carrier types (electrons and holes) can contribute to conduction.

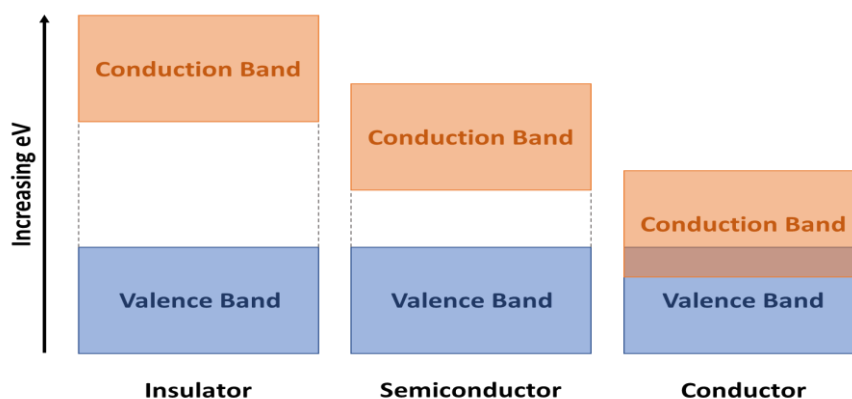


**Fig. 2.1:** Representation of the band gap for insulating, semiconductor and conductive materials.

The energy between the valence band and conduction band is an extremely important parameter. Figure 2.1 provides a representation of the band gap of three common material types. Large band gap materials are good electrical insulators as few carriers will have enough energy to transition from the valence to conduction band. A material is considered electrically conductive if the band gap is small or overlapping as carriers readily move between bands. Finally, semiconductors are the intermediate case and are an essential component of most electronic and photonic circuits. The energy bands can be expressed as a function of the magnitude of the crystal momentum ( $k$ -vector) and can also depend on the crystallographic direction of the momentum. If the minima of the conduction band and the maxima of the valence band correspond to the same  $k$  value, the band gap is considered direct and photons can be readily emitted or absorbed provided they have sufficient energy. Conversely, an indirect bandgap occurs if the respective  $k$  vectors are different, as shown in Figure 2.2. In this case, carriers must undergo significant changes in momentum to transition between levels which can be achieved with the aid of lattice vibrations known as phonons [2]. As a result, direct bandgap semiconductors are much more efficient at radiative absorption and emission which is important for many photonic devices such as LEDs and lasers.

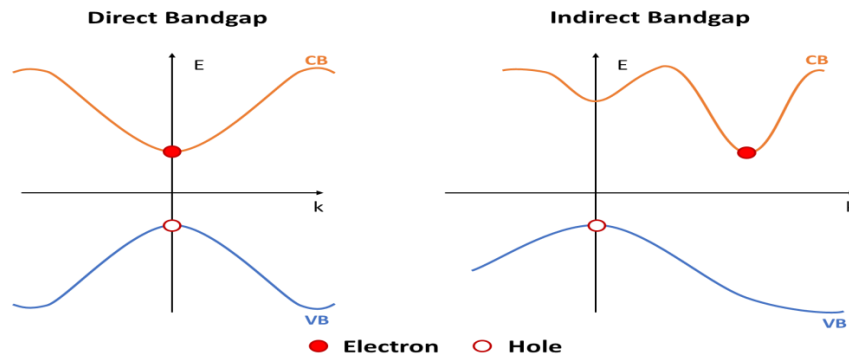


**Fig. 2.2:** Direct and indirect band gaps found in semiconductor materials.

A heterojunction is an interface that occurs when two materials of unequal bandgaps are joined at the atomic level. The resultant interfaces restrict the movement of charge carriers which can be highly advantageous. A quantum well is a particular kind of double heterostructure where a thin “well” layer is enclosed by two “barrier” layers. This layer is so thin (about 40 atomic layers) that the allowed electron states as a function of energy have distinct steps instead of the square root dependence of bulk material [3]. This quantum confinement of the charge carriers leads to improved performance of electro optic devices such as lasers and modulators by exhibiting interesting properties which will be discussed later in this chapter. The successful fabrication of double heterostructures involves the combination of multiple materials with similar lattice constants to form single crystal, defect free films which can be epitaxially grown on each other. In this way, compound materials of group III and V of the periodic table have played a major role in the realisation of various active and passive photonic components. Industrial scale substrate wafers of binary compounds such as InP and GaAs are currently available. Ternary and quaternary compounds are grown epitaxially onto these substrates to form heterojunctions with the appropriate band profile. A popular quaternary for wavelengths suitable for long-distance optical communication is InGaAsP. This quaternary can be grown on InP to form layers with band gaps corresponding to a wavelength range which includes the important minimal loss fibre-optic bands of 1.31  $\mu\text{m}$  and 1.55  $\mu\text{m}$ . Such quaternaries can be specified by an x and y value where the ratio between these values is fixed for a given lattice constant. For example,  $\text{In}_{1-x}\text{Ga}_x\text{As}_y\text{P}_{1-y}$  can be lattice matched to an InP substrate by setting x

approximately equal to 0.46y [4]. Alternatively, the lattice constant for a quaternary of given composition can be calculated from Vegard's law [5]. For example, the lattice constant for InGaAsP can be expressed as:

$$a(x, y) = xy a_{\text{GaAs}} + x(1 - y)a_{\text{GaP}} + (1 - x)y a_{\text{InAs}} + (1 - x)(1 - y)a_{\text{InP}}$$

Using a similar approach, the lattice constant for other alloys can be calculated and Figure 2.3 plots the lattice constant, band gap energy and corresponding wavelength for a range of III-V semiconductor materials. Corners represent binary compounds; the adjoining lines signify ternary compounds and quaternary compounds can be located in any region enclosed by four binary points. Moreover, solid lines connecting the binary compounds are direct band gaps and dotted lines represent indirect band gaps.

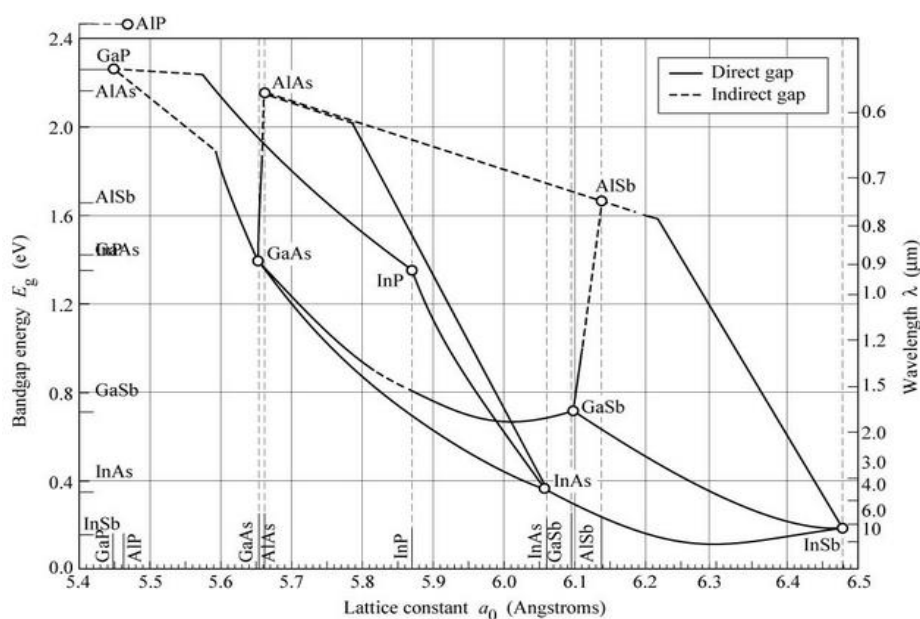


**Fig. 2.3:** Band energies and corresponding wavelengths for a range of III-V semiconductor compounds [6].

Finally, lattice matching is necessary to avoid crystalline defects such as dangling bonds. These bonds result in intra-band electron trap states which can increase the rate of non-radiative transitions. However, small lattice mismatches can be tolerated up to a certain critical thickness without any defects forming. This critical thickness ( $t_c$ ) can be expressed as a function of the substrate lattice constant ( $a_s$ ) and the layer lattice constant ( $a_l$ ) [7].



$$t_c = \frac{a_s a_l}{2(a_l - a_s)}$$

Therefore, a thin layer with a slightly different lattice constant will distort to fit the substrate's crystalline structure. This distortion occurs both parallel and perpendicular to the interface, so that the film approximately retains its unit cell volume. Such an approach can be used to create strained quantum wells, achieving more favourable electrooptic properties without introducing any undesired defects. A secondary limit that must be considered is the cumulative stress on the entire structure, which can result in relaxations at the top and bottom of the epitaxial stack. This issue can be compensated for by adjusting the strain of the barrier layers.

In order to make the multilayer structures required for quantum well epitaxy, processes which grow lattice-matched layers with precisely controlled thicknesses are required. Liquid phase epitaxy (LPE) is the original method used to form epitaxial layers [8]. An InP or GaAs substrate is placed in a slider that can be moved across the surface of molten liquid which has been saturated with the desired material and dopants. The temperature difference between wafer and the melt is such that atoms solidify onto the crystal substrate. This process could be repeated using multiple melts to form a layered deposition. While it was widely used in early laboratory work, it proved unsuitable for industrial applications due to difficulties in growing uniform layers over large surface areas. In vapour phase epitaxy (VPE) methods, atoms (which can include dopants) are introduced to the substrate in a gaseous phase [9]. Under carefully controlled conditions, reactions occur between the gases and substrate, resulting in atoms being deposited on the surface. These newly deposited layers replicate the underlying crystalline structure. A popular form of VPE known as metalorganic vapour phase epitaxy (MOVPE) transports material using organic molecules to produce III-V compounds [10]. For example, indium phosphide can be grown on a heated substrate by introducing trimethylindium and phosphine in an oxygen free environment. This pyrolysis results in the deposition of atoms onto the surface of the substrate. Molecular beam epitaxy (MBE) is another way in which epitaxy can be formed and could be described as a sophisticated evaporation technique performed at high vacuum [11]. Elements are evaporated from ovens and

deposited onto the heated substrate where they assemble in crystalline order. With proper control of the sources, a wide range of material compositions and doping levels can be achieved. Finally, atomic layer deposition (ALD) is a variation of the MBE process in which single atomic layers of material are deposited at a time [12]. The majority of ALD reactions use two gas phase chemicals which are introduced in a series of sequential, non-overlapping pulses. Consequently, the reaction terminates once all the available area on the surface of the substrate is consumed, limiting the deposition of a pulse to a single atomic layer. ALD is used in a wide range of research fields such as photonics, photovoltaics and energy storage applications.

### 2.3 Optical Waveguides

The fundamental behaviour of light as it propagates through a medium is described by Maxwell's equations which are listed below in time-harmonic form.

$$\nabla \times \mathbf{E} = -j\omega \mathbf{B}$$

$$\nabla \times \mathbf{H} = \mathbf{J} + j\omega \mathbf{D}$$

$$\nabla \cdot \mathbf{B} = 0$$

$$\nabla \cdot \mathbf{D} = \rho$$

The quantities above are the electric field ( $\mathbf{E}$ ), magnetic flux density ( $\mathbf{B}$ ), magnetic field ( $\mathbf{H}$ ), current density ( $\mathbf{J}$ ), electric flux density ( $\mathbf{D}$ ) and charge density ( $\rho$ ). Important relationships between these quantities include  $\mathbf{D} = \epsilon \mathbf{E}$ ,  $\mathbf{B} = \mu \mathbf{H}$  and  $\mathbf{J} = \sigma \mathbf{E}$  where  $\epsilon$ ,  $\mu$  and  $\sigma$  are the electrical permittivity, magnetic permeability and electrical conductivity of the medium respectively. Any medium of interest can be placed into one of the four categories listed below, where  $\omega$  is the angular frequency of the wave [13].

1. Vacuum ( $\sigma = 0, \epsilon = \epsilon_0, \mu = \mu_0$ )
2. Lossless dielectric ( $\sigma = 0, \epsilon = \epsilon_r \epsilon_0, \mu = \mu_r \mu_0$ , or  $\sigma \ll \omega \epsilon$ )
3. Lossy dielectric ( $\sigma \neq 0, \epsilon = \epsilon_r \epsilon_0, \mu = \mu_r \mu_0$ )
4. Good conductor ( $\sigma \approx \infty, \epsilon = \epsilon_0, \mu = \mu_r \mu_0$ , or  $\sigma \gg \omega \epsilon$ )

A lossy dielectric is defined as a medium in which an electromagnetic wave loses power as it propagates and can be considered as a general case from which the other types of media can be derived. Therefore, considering an isotropic, homogeneous, lossy dielectric medium that is charge free ( $\rho = 0$ ), Maxwell's equations become

$$\nabla \times \mathbf{E} = -j\omega\mu\mathbf{H}$$

$$\nabla \times \mathbf{H} = (\sigma + j\omega\epsilon)\mathbf{E}$$

$$\nabla \cdot \mathbf{E} = 0$$

$$\nabla \cdot \mathbf{H} = 0$$

The homogeneous E field vector wave equation can then be derived by taking the curl of both sides of the equation  $\nabla \times \mathbf{E} = -j\omega\mu\mathbf{H}$  and substituting in  $\nabla \cdot \mathbf{E} = 0$  and  $\nabla \times \mathbf{H} = (\sigma + j\omega\epsilon)\mathbf{E}$ . The corresponding H field vector wave equation can also be obtained using a similar procedure. These Helmholtz equations describe the propagation of electromagnetic waves through a known medium.

$$\nabla^2 \mathbf{E} - \gamma^2 \mathbf{E} = 0$$

$$\nabla^2 \mathbf{H} - \gamma^2 \mathbf{H} = 0$$

The parameter  $\gamma$  is known as the propagation constant of a medium and can be expressed as a complex quantity  $\gamma = \alpha + j\beta$  where  $\alpha$  and  $\beta$  represent the attenuation and phase contributions [13].

$$\alpha = \omega \sqrt{\frac{\mu\epsilon}{2} \left[ \sqrt{1 + \left[\frac{\sigma}{\omega\epsilon}\right]^2} - 1 \right]}$$

$$\beta = \omega \sqrt{\frac{\mu\epsilon}{2} \left[ \sqrt{1 + \left[\frac{\sigma}{\omega\epsilon}\right]^2} + 1 \right]}$$

The refractive index of a medium ( $n = c\sqrt{\mu\epsilon}$ ) is a dimensionless quantity which also defines how light propagates through it and can also be expressed as a complex

number to account for attenuation. As with silica optical fibres, a core region of high refractive index ( $n_1$ ) surrounded by a cladding region of lower refractive index ( $n_2$ ) is used to confine light along semiconductor waveguides. When light propagating in the core strikes the boundary at an oblique angle of incidence ( $\theta_i$ ) a certain percentage of the light is reflected back into the core while the remainder is transmitted into the cladding. According to law of reflection the angle of reflection ( $\theta_r$ ) will be equal to the angle of incidence ( $\theta_r = \theta_i$ ), while Snell's law states the relationship between the angle of incidence, the angle of transmission and the medias' respective refractive indices:  $n_1 \sin \theta_i = n_2 \sin \theta_t$  [14]. For certain propagation angles, no light is transmitted from the core into the cladding region resulting in optical confinement. This condition known as total internal reflection occurs when the angle of incidence is greater than a critical angle ( $\theta_c$ ). This critical angle can be calculated by setting the transmission angle to 90 degrees.

$$\sin \theta_c = \frac{n_2}{n_1} = \sqrt{\frac{\mu_2 \epsilon_2}{\mu_1 \epsilon_1}}$$

Figure 2.4 depicts two ray diagrams which illustrate the transmission of optical power into the cladding for angles less than the critical angle and the optical confinement mechanism which occurs when  $\theta_c$  is exceeded.

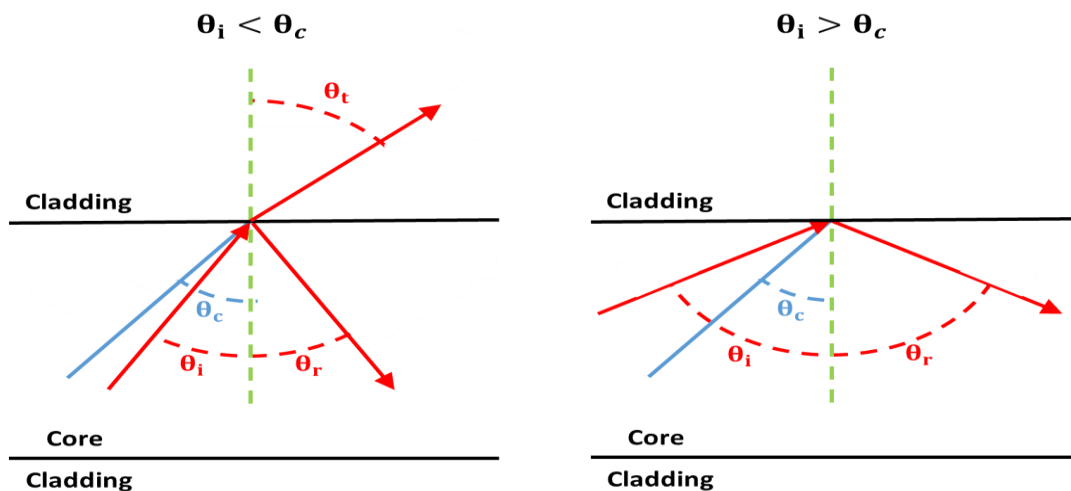


**Fig 2.4:** Ray diagrams depicting Snell's Law (left) and its special case namely total internal reflection (right).

## 2.4 Semiconductor Lasers

A semiconductor laser is an optical device which emits a coherent output through the process of optical amplification based on stimulated emission of photons. Such devices commonly consist of a gain section to is an active region in which photons are created, surrounded by mirrors, which reflect a percentage of the photons back into the cavity. This reflection provides the optical feedback necessary for stimulated emission to become the dominant effect in the cavity. To begin describing the behaviour of a laser gain section, the electronic transitions that occur in semiconductor materials must first be defined [15]. Spontaneous emission ( $R_{sp}$ ) represents the spontaneous recombination of an electron in the conduction band and a hole in the valence band resulting in the release of a photon. This is the primary mechanism in light emitting diodes (LEDs) as these devices create an incoherent light source. Stimulated absorption ( $R_{sa}$ ) involves the creation of an electron-hole pair due to photon absorption. Stimulated emission ( $R_{st}$ ) is the principle mechanism involved in the creation of coherent photons, which are essential for lasers to operate. It involves a photon stimulating the recombination of an electron-hole pair which creates a second photon with the same phase, frequency and direction as the first. Finally, non-radiative transitions ( $R_{nr}$ ) can also occur which result in electron-hole pairs recombining without the release of a photon. The energy released by these recombinations can be transferred to other carriers in the form of kinetic energy. A representation of these transitions is illustrated in Figure 2.5.

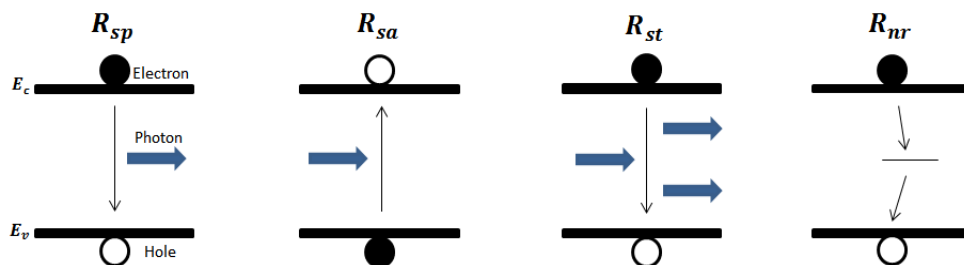


**Fig 2.5:** Electron transitions between the conduction and valence bands.

As discussed above, stimulated emission required both the presence of an electron-hole pair and a photon to occur. Semiconductor layers are grown to form p-i-n

heterostructures, which creates an active region, confining the carriers which can contribute to photon emission. The total number of carriers lost due to recombination ( $R_{rec}$ ) is the sum of the carriers lost due to spontaneous emission, non-radiative recombination, stimulated emission and Auger recombination ( $R_a$ ).

$$R_{rec} = R_{sp} + R_{nr} + R_a + R_{st}$$

The spontaneous emission, non-radiative recombination and Auger recombination are dependent on the carrier density (N) and can be expressed as  $R_{sp} \approx BN^2$ ,  $R_{nr} \approx AN$  and  $R_a \approx CN^3$  respectively where A is the non-radiative recombination coefficient, B is the bimolecular recombination coefficient and C is Auger coefficient. The carrier loss terms  $R_{sp}$ ,  $R_{nr}$  and  $R_l$  can be grouped to represent the carrier density divided by the carrier lifetime ( $\tau$ ) [16].

$$\frac{N}{\tau} = R_{sp} + R_{nr} + R_a$$

Since stimulated emission relies on the presence of photons to occur, the rate of stimulated emission is directly linked with the coherent photon density ( $N_p$ ). Assuming that the length of the active region is sufficiently small, the rate of stimulated emission can be expressed as a function of the group velocity ( $v_g$ ), gain (g) and photon density [16].

$$R_{st} = \frac{\Delta N_p}{\Delta t} = v_g g N_p$$

Gain represents the increase in photons due to stimulated electron-hole recombination while the transparency carrier density ( $N_{tr}$ ) is the carrier density required to overcome the absorption of the material, which results in zero gain (and zero loss). The relationship between the gain and transparency carrier density can be expressed as  $g \approx a(N - N_{tr})$ , where  $a$  is the differential gain ( $\frac{\delta g}{\delta N}$ ). It is possible to create additional carriers by passing a current through the junction, however, this current is not 100% efficient. The internal quantum efficiency ( $\eta_i$ ) is the fraction of the injected current that generates carriers in the active region. The net gain of carriers can be described as  $G_{Gen} = \frac{n_i I}{qV}$  where, I is the applied current, q is the

elementary charge and  $V$  represents the volume of the active region. Therefore, the rate of change of carriers is given by

$$\frac{dN}{dt} = G_{Gen} - R_{rec} = \frac{n_i I}{qV} - \frac{N}{\tau} - v_g g N_p$$

The next step is to develop an equation for the rate of change of the photon density in terms of carrier density and stimulated emission. As discussed above, every time an electron hole pair is stimulated to recombine, another photon is generated. A percentage of photons produced by spontaneous emission can also contribute to the number of coherent photons. This percentage is calculated by multiplying the rate of spontaneous emission ( $R_{sp}$ ) by a spontaneous emission factor ( $\beta_{sp}$ ). The loss of photons due to absorption and scattering can be represented as  $\frac{N_p}{\tau_p}$ , where  $\tau_p$  is the photon lifetime. Finally, since the cavity volume occupied by photons ( $V_p$ ) is usually larger than the active region volume ( $V$ ), the change in photon density is related to the optical confinement factor ( $\Gamma = \frac{V}{V_p}$ ).

$$\frac{dN_p}{dt} = \Gamma v_g g N_p + \Gamma \beta_{sp} R_{sp} - \frac{N_p}{\tau_p}$$

These expressions for  $\frac{dN}{dt}$  and  $\frac{dN_p}{dt}$  are known as the laser rate equations and are valid both above and below threshold [17]. Using these equations, the contributions of spontaneous and stimulated emission to a laser's output power can be derived as a function of current ( $I$ ) [16].

$$P_{spontaneous} = \eta_r \eta_d \beta_{sp} \frac{h\nu}{q} I$$

$$P_{stimulated} = \eta_d \frac{h\nu}{q} (I - I_{th})$$

The differential quantum efficiency ( $\eta_d$ ) is related to the internal quantum efficiency, optical loss in the cavity and mirror loss. The radiative efficiency ( $\eta_r$ ) represents the ratio of spontaneous emission versus the other forms of emission ( $R_{sp}$ ,  $R_{nr}$  and  $R_l$ ). Only spontaneous emission contributes to the optical power when the current is

below threshold. Above threshold the stimulated power quickly becomes dominant as the spontaneous power is clamped at its threshold value (Figure 2.6).

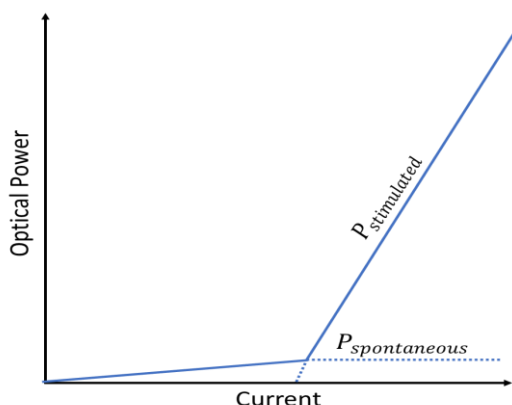


**Fig 2.6:** Optical power of a laser vs current

A Fabry-Pérot (FP) laser, which is the simplest form of laser design, consists of an optical cavity capable of providing gain enclosed by two highly reflective mirrors. In semiconductor devices, these mirrors are usually the product of the high refractive index difference between the gain material and air at a cleaved facet. A variation of the FP, known as slotted Fabry-Pérot (SFP) lasers [18], relies on arrays of waveguide slots instead of cleaved facets to provide optical feedback into the cavity. The spacing between the slots can be adjusted to modify the free running spectrum of the laser. In the case of facetless SFP lasers, a Vernier effect can be used to ensure single mode operation with a tunability of up to 30 nm reported [19]. SFP lasers offer excellent potential for monolithic regrowth-free integration and are compatible with UV contact lithography unlike distributed feedback (DFB) [20] and distributed Bragg reflector (DBR) lasers [21]. A scanning electron microscope image of a single facet SFP laser is shown in Figure 2.7.



**Fig 2.7:** Single facet SFP laser with angled output on the right side to minimise reflections from the facet.



Optical injection locking [22] is a technique which has received significant interest of late as it has found applications in increasing laser modulation bandwidths [23], single sideband modulation [24] and opto-electronic oscillators [25]. It involves the coupling of external optical power from a master laser into a slave laser. For a sufficiently small wavelength detuning between the sources, the corresponding resonant mode of the slave laser is forced to lase while the other free running modes are suppressed. This approach differs from mutual coupling in the sense that light is considered to be propagating in one direction only. This is commonly achieved by means of an optical isolator or a large optical power difference between the master and slave lasers. The stable injection locking of a SFP laser by a monolithically integrated master SFP laser also has been investigated [26] with the coupling power controlled using the variable gain section which acted as a variable optical attenuator or amplifier depending on the bias.

## 2.5 Semiconductor Modulators

A modulator is an optical device which is used to encode data onto a beam of light by perturbing one of its properties such as amplitude, phase or polarisation. There are three main field induced effects exhibited by semiconductor devices which are: the Pockels effect, the Kerr effect and the electro-absorption effect. The Pockels effect changes or produces birefringence in an optical medium subject to an external electric field. This effect, which is also known as the linear electro-optic effect is proportional to the magnitude of the electric field, but only occurs in crystals which lack inversion symmetry [27]. Therefore, silicon modulators rely on carrier induced refractive index changes or strain induced refractive index changes [28]. In III-V compound materials, which have no centre of symmetry, the atoms or molecules become polarised due to the opposite forces experienced by their positively and negatively charged components. The redistribution of these bound charges alters the relative permittivity ( $\epsilon_r$ ) tensor of the material. Since the refractive index is defined as  $n = \sqrt{\epsilon_r}$ , any change to the permittivity of the medium results in a change in the refractive index which would result in a phase change of a propagating optical mode. The Kerr effect also causes a change in the refractive index of a material which is directly proportional to the electric field squared. Unlike the Pockels effect, the Kerr

effect is evident in all materials and therefore exhibited by silicon based devices [29]. However, the Kerr effect is comparatively small and will be dominated by the Pockels effect in media that lack inversion symmetry. The Kerr electro-optic effect is a specific case in which the medium becomes birefringent when a slowly varying external electric field is applied (unlike the optical Kerr effect discussed in section 1.2). The difference in refractive index can be expressed as a function of the wavelength of the light ( $\lambda$ ), the Kerr constant ( $K$ ) and the strength of the electric field ( $E$ ):

$$\Delta n = \lambda K E^2$$

Finally, field induced electro-absorption effects involve the change in optical absorption of a semiconductor under an applied electric field. According to basic semiconductor theory, a photon must have an energy equal to or greater than the difference between the conduction and valence bands to be absorbed. However, the wavefunctions of an electron and hole in the presence of an electric field become Airy functions rather than plane waves. Under sufficient applied electric field, the semiconductor bandgaps begin to tilt and the tails of these function penetrate the bandgap. The resulting overlap gives rise to an exponential tail in the fundamental absorption edge of the material. This non-zero absorption below the bandgap in bulk materials is known as the Franz-Keldysh effect [30], [31]. The situation is different in quantum well structures, where a lower bandgap well is encompassed by high band gap barriers. The resultant potential barriers confine the carriers while also forming discrete energy levels for both conduction and valence bands. Under no external bias, the electron and hole distributions form symmetric functions at the centre of the well. An applied electric field results in electron states shifting to lower energies while the hole states shift to higher energies reducing the effective band gap of the well. Simultaneously, the electron and hole wave functions shift to opposite sides of the well, decreasing the overlap integral which in turn reduces the overall absorption level. However, greater confinement of the wave functions can maintain sufficient absorption levels even in the presence of a high electric field. Figure 2.8 shows the electron-hole confinement in a typical potential

well in the absence of an electric field and the deformation of the wavefunction and reduced energy levels in the presence of an electric field.

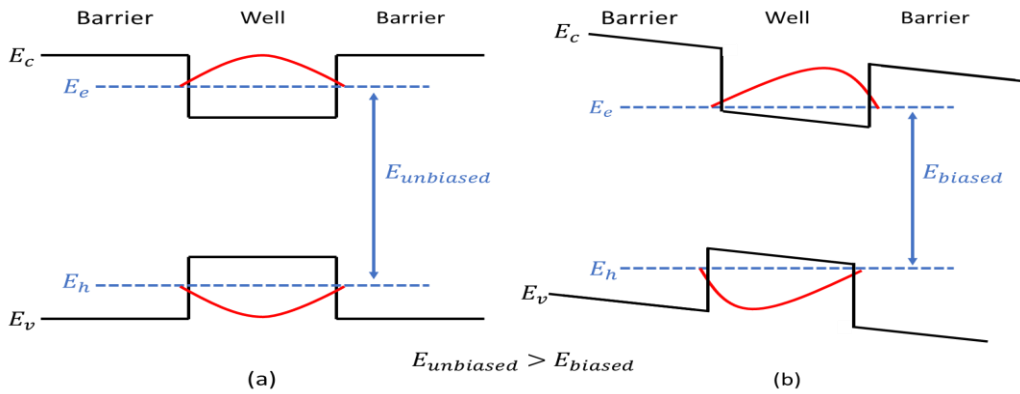


**Fig 2.8:** Electron-hole confinement in a potential well (a) in the absence of an electric field and (b) under bias.

At this point it is necessary to account for electrons and holes which are stimulated due to photon absorption as they can form electron-hole pair resonances due to Coulomb interactions [32]. These resonances are known as excitons and can greatly enhance the absorption at energies close to the bandgap of the semiconductor. When an electron hole pair is created, they are initially spatially close. Consequently, the electron in the conduction band is attracted to the oppositely charged hole in the valence band in accordance with Coulomb's law, resulting in the creation of energy levels smaller than the material's band gap [33]. However, excitons quickly decay in bulk materials at room temperature as their binding energy is less than the thermal energy of the associated particles. Multiple quantum wells can be used to enhance the Coulomb attraction between the electrons and holes by improving the spatial confinement. This increased confinement allows sharp excitonic peaks to be visible even at room temperature as the binding energy of the two-dimensional exciton is four times larger than the three-dimensional case. The  $n^{th}$  bound state exciton energy is given by [7]:

$$E_n = -\frac{R_y}{n^2}$$

Where the Rydberg energy ( $R_y$ ) can be expressed in terms of the effective mass and the permittivity of the material:

$$R_y = \frac{m_r e^4}{8h^2 \epsilon_s^2}$$

This field induced change in the absorption in a multiple quantum well structure combined with the excitonic resonances at high applied fields is known as the quantum confined stark effect (QCSE) [34]. Due to the Kramers-Kronig relations, a change in absorption also results in a change in refractive index and therefore, can also be utilised by phase modulators.

The two most common forms of modulator currently used in PICs are Mach-Zehnder modulators (MZMs) and electroabsorption modulators (EAMs). A MZM, which is based on the interferometric principle, utilises field induced changes in refractive index to alter the relative phase of two light beams which have been split [35]. The phase shift causes constructive and destructive interference as the light in the two arms is recombined. The device is usually fabricated using passive epitaxial material to minimise absorption losses, even at high reverse biases. MZMs have numerous advantages over EAMs including reduced inherent optical loss, lower chirp and higher suitability to phase modulation formats. However, MZMs are typically in the order of 1.5 mm in length or longer. In addition to this large footprint, MZMs' tendency to operate using passive epitaxy means that they have a larger bandgap than that of the operating wavelength of a corresponding laser. Therefore, advanced integration techniques need to be applied when forming MZM based PICs. Figure 2.9 illustrates the two states of an MZM.

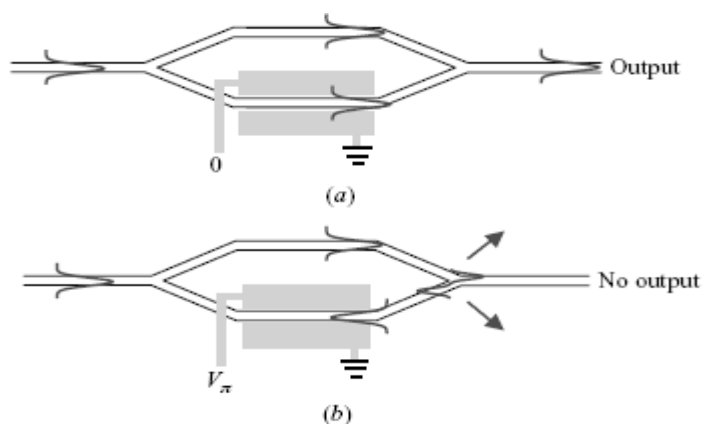


**Fig 2.9:** Schematic of a Mach-Zehnder Modulator with (a) constructive and (b) destructive interference [36].

An electroabsorption modulator is a semiconductor device which is based on a voltage induced absorption change due to the Franz-Keldysh effect or quantum confined stark effect [37]. An EAM is easier to incorporate into an integrated circuit than an MZM as it has a similar band gap energy to that of the operating wavelength of the laser. EAMs can also be much smaller than an MZM ( $\sim 100 \mu\text{m}$ ) if the wavelength of the optical signal coincides with the optimum wavelength for absorption, making them highly suitable for dense PIC designs. However, as the device is absorption based it, is susceptible to saturation.

### **2.6 Photonic Integration Techniques**

As discussed in previous sections, one of the primary difficulties in creating photonic integrated circuits is due to the difference in optimal band structure between light sources and modulators. There are many types of integration that have been attempted to overcome this material difference. Heterogeneous integration involves the fabrication of components on different substrates and combining them using optical coupling. Silicon on insulator (SOI) solutions provide a high index contrast which allows for passive low loss waveguides at  $1.55 \mu\text{m}$  which are capable of high curvature [38]. Rib waveguide structures are formed due to the refractive contrast between the silicon, air and underlying silicon dioxide layer. While silicon modulators and dense ICs have been demonstrated, silicon is inefficient as a light source due to its indirect band gap. Therefore, III-V layers, structure and devices are required to generate photons. This can be achieved using flip-chip techniques to mount a III-V device onto the silicon substrate with light being laterally coupled between the two sections using lensed fibre or polymer waveguides [39]. An alternative solution is to adhere a III-V layer onto a fabricated silicon PIC which acts as an optical pump, introducing light to the system. This optical power is transferred to the silicon structures using a variety of techniques such as tapers or evanescent coupling to create devices such as a hybrid InP/SOI 10 Gbps transmitter which is based on a tunable laser and MZM [40]. However, the use of such heterogeneous approaches introduce challenges such as varying mechanical properties and fabrication complexity.

Alternatively, monolithic integration focuses on the implementation of PICs using a single substrate, therefore removing the need for optical interconnects to link the different materials. A wide range of techniques exist for monolithic integration based on current technologies including vertical twin-guide [41], butt-joint regrowth [42], selective area regrowth [43], quantum well offsetting [44] and dual quantum wells. The layer structure of such approaches is shown in Figure 2.10. However, these methods rely on selective area etching and regrowth to form photonic devices on a single substrate. As with hybrid integration, PICs with extensive functionality have been demonstrated using monolithic approaches, such as optical transmitters for DWDM, QPSK and PAM4 optical systems [45]. However, they also require complex fabrication techniques which require advanced foundries and long processing durations.

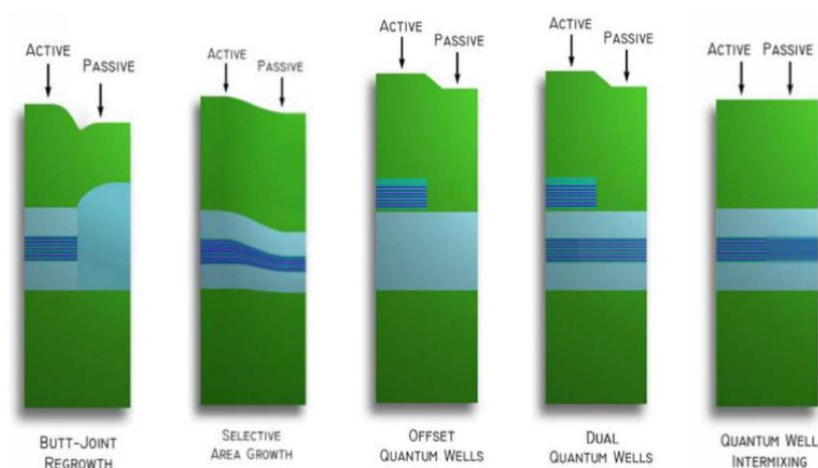


**Fig 2.10:** Active-passive waveguide integration approaches [46].

As a result, regrowth-free monolithic approaches to photonic integrated circuits are being investigated by the Integrated Photonics Group at Tyndall National Institute with the aim of reducing cost, potentially increasing device yield and making the technology more accessible. For example, while regrowth processes commonly take months to complete, the monolithic regrowth-free process discussed in Chapter 3 had a process time of approximately 6 days.

## 2.7 Proposed Coherent WDM PIC

In response to the need for both coherent WDM systems and regrowth-free solutions to PICs, this thesis proposes a novel monolithic transmitter which does not

require epitaxial regrowth. Furthermore, all components are compatible with standard UV contact lithography which is more suitable for large scale manufacturing than higher resolution approaches such as E-beam lithography. As discussed in Chapter 1, coherent WDM requires the generation of a coherent optical comb and the demultiplexing, modulation and multiplexing of the subcarriers. A recent study [47] has demonstrated the monolithic integration of slotted Fabry-Pérot lasers into a three-section device to produce a low linewidth optical frequency comb using the injection locked gain switching technique. An optical comb consisting of up to 8 comb lines within a 3.5 dB band was observed making it suitable for use in a prototype coherent WDM PIC. It was also shown that the optical comb could be red shifted as far as 1584 nm by a combination of thermal and Vernier tuning. At this point, traditional coherent WDM approaches demultiplex the comb lines for modulation. However, common integratable demultiplexers such as arrayed waveguide gratings (AWGs) [48] have large footprints and low fabrication tolerance. Alternatively, the selective amplification and filtering properties of injection locked SFP lasers has been published, reporting the suppression of unwanted wavelengths in excess of 20 dB [49]. Moreover, the tuning of the SFP laser to different comb lines by varying the applied bias was also shown. Therefore, instead of formally demultiplexing the comb lines, the optical power could instead be split into multiple arms and the active filtering properties of the SFP lasers used to suppress unwanted channels while providing gain to the wavelength of interest. This would effectively split the comb lines into the respective arms of the transmitter while maintaining coherence. The next step would be to encode data on the filtered comb lines using optical modulators. As discussed in section 2.5, while MZMs offer low chirp and low optical loss, they are difficult to integrate without the use of heterogeneous or regrowth techniques. However, EAMs operate much closer to the band edge and therefore are compatible with a redshifted comb source. The modulated carriers would then be recombined while maintaining coherence, to produce a coherent WDM signal.

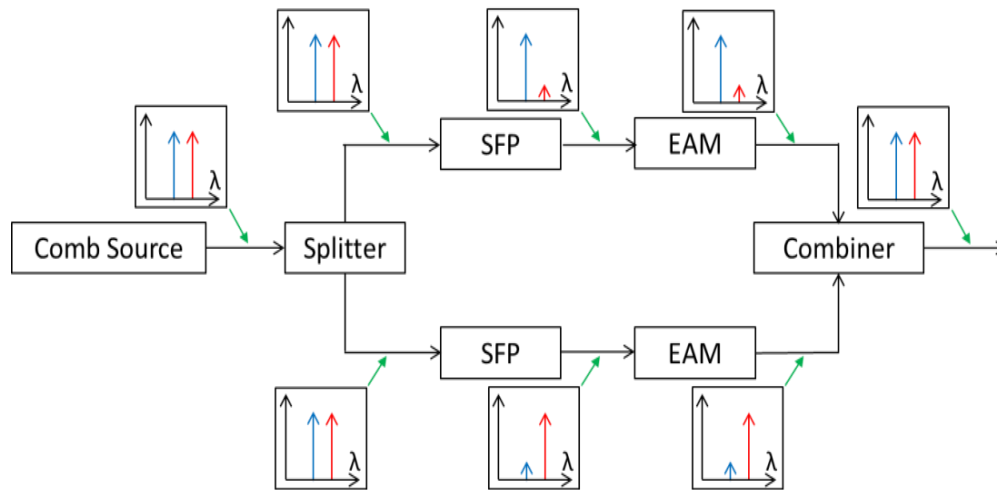


**Fig. 2.11:** Schematic of proposed regrowth-free coherent WDM transmitter based on SFP lasers and EAMs.

While the final transmitter will inevitably contain multiple arms to maximise the number of carriers which can be modulated, this thesis will focus on developing a two-armed prototype transmitter outlined in Figure 2.11 as proof of concept. The next chapter will outline the development of fabrication processes suitable for DC components (such as lasers) and high-speed modulators respectively. The following chapters will then utilise these processes to develop a range of components and PICs, striving towards the realisation of the prototype coherent WDM transmitter described above.

### Bibliography

- [1] F. Reines and H. W. Sobel, "Test of the Pauli Exclusion Principle for Atomic Electrons," *Phys. Rev. Lett.*, vol. 32, no. 17, pp. 954–954, Apr. 1974.
- [2] L. Gu, V. Srot, W. Sigle, C. Koch, P. van Aken, F. Scholz, S. B. Thapa, C. Kirchner, M. Jetter, and M. Rühle, "Band-gap measurements of direct and indirect semiconductors using monochromated electrons," *Phys. Rev. B*, vol. 75, no. 19, p. 195214, May 2007.
- [3] N. Holonyak, R. Kolbas, R. Dupuis, and P. Dapkus, "Quantum-well heterostructure lasers," *IEEE J. Quantum Electron.*, vol. 16, no. 2, pp. 170–186, Feb. 1980.
- [4] G. H. Olsen, T. Z. Zamerowski, R. T. Smith, and E. P. Bertin, "InGaAsP quaternary alloys: Composition, refractive index and lattice mismatch," *J. Electron. Mater.*, vol. 9, no. 6, pp. 977–987, Nov. 1980.



- [5] A. R. Denton and N. W. Ashcroft, "Vegard's law," *Phys. Rev. A*, vol. 43, no. 6, pp. 3161–3164, Mar. 1991.
- [6] [https://www.google.ie/search?q=tien+1988&client=firefox-b&source=Inms&tbm=isch&sa=X&ved=0ahUKEwj4pJywhI7VAhVNaVAKHdBfCXAQ\\_AUICigB&biw=1280&bih=932#imgrc=7cJKsbF5DHgbcM](https://www.google.ie/search?q=tien+1988&client=firefox-b&source=Inms&tbm=isch&sa=X&ved=0ahUKEwj4pJywhI7VAhVNaVAKHdBfCXAQ_AUICigB&biw=1280&bih=932#imgrc=7cJKsbF5DHgbcM): [Accessed: 16-Jul-2017].
- [7] S. L. Chuang, *Physics of photonic devices*. John Wiley & Sons, 2009.
- [8] E. Kuphal, "Liquid phase epitaxy," *Appl. Phys. A Solids Surfaces*, vol. 52, no. 6, pp. 380–409, Jun. 1991.
- [9] M. R. Leys and H. Veenvliet, "A study of the growth mechanism of epitaxial GaAs as grown by the technique of metal organic vapour phase epitaxy," *J. Cryst. Growth*, vol. 55, no. 1, pp. 145–153, Oct. 1981.
- [10] J. J. COLEMAN, "Metal-organic chemical vapor deposition," *Conf. Lasers Electro-Optics (1985), Pap. THO2*, p. THO2, 1985.
- [11] J. R. Arthur, "Molecular beam epitaxy," *Surf. Sci.*, vol. 500, no. 1–3, pp. 189–217, Mar. 2002.
- [12] M. Leskelä and M. Ritala, "Atomic layer deposition (ALD): from precursors to thin film structures," *Thin Solid Films*, vol. 409, no. 1, pp. 138–146, Apr. 2002.
- [13] W. S. C. Chang, *Fundamentals of Guided-Wave Optoelectronic Devices*. Cambridge: Cambridge University Press, 2009.
- [14] G. R. Fowles, *Introduction to modern optics*. Dover Publications, 1989.
- [15] A. Rose, "Recombination Processes in Insulators and Semiconductors," *Phys. Rev.*, vol. 97, no. 2, pp. 322–333, Jan. 1955.
- [16] S. W. C. Larry A. Coldren, *Diode Lasers and Photonic integrated Circuits*. Santa Barbara: Wiley-Interscience Publication, 1995.
- [17] D. Marcuse, "Classical derivation of the laser rate equation," *IEEE J. Quantum Electron.*, vol. 19, no. 8, pp. 1228–1231, Aug. 1983.
- [18] D. Byrne, Q. Lu, W. Guo, J. Donegan, B. Corbett, B. Roycroft, P. Lambkin, J. Engelstaedter and F. Peters, "A Facetless Laser Suitable For Monolithic Integration,"

- in *Conference on Lasers and Electro-Optics/Quantum Electronics and Laser Science Conference and Photonic Applications Systems Technologies OSA Technical Digest (CD) (Optical Society of America, 2008), paper JThA28*, 2008.
- [19] B. Corbett, C. Percival, and P. Lambkin, "Multiwavelength array of single-frequency stabilized Fabry-Perot lasers," *IEEE J. Quantum Electron.*, vol. 41, no. 4, pp. 490–494, Apr. 2005.
- [20] S. R. Jain, M. N. Sysak, G. Kurczveil, and J. E. Bowers, "Integrated hybrid silicon DFB laser-EAM array using quantum well intermixing," *Opt. Express*, vol. 19, no. 14, p. 13692, Jul. 2011.
- [21] G. Hasnain, K. Tai, L. Yang, Y. H. Wang, R. J. Fischer, J. D. Wynn, B. Weir, N. K. Dutta, and A. Y. Cho, "Performance of gain-guided surface emitting lasers with semiconductor distributed Bragg reflectors," *IEEE J. Quantum Electron.*, vol. 27, no. 6, pp. 1377–1385, Jun. 1991.
- [22] R. Lang, "Injection locking properties of a semiconductor laser," *IEEE J. Quantum Electron.*, vol. 18, no. 6, pp. 976–983, Jun. 1982.
- [23] J. Wang, M. K. Haldar, L. Li, and F. V. C. Mendis, "Enhancement of modulation bandwidth of laser diodes by injection locking," *IEEE Photonics Technol. Lett.*, vol. 8, no. 1, pp. 34–36, Jan. 1996.
- [24] Hyuk-Kee Sung, E. K. Lau, and M. C. Wu, "Optical Single Sideband Modulation Using Strong Optical Injection-Locked Semiconductor Lasers," *IEEE Photonics Technol. Lett.*, vol. 19, no. 13, pp. 1005–1007, Jul. 2007.
- [25] H.-K. Sung, X. Zhao, E. K. Lau, D. Parekh, C. J. Chang-Hasnain, and M. C. Wu, "Optoelectronic Oscillators Using Direct-Modulated Semiconductor Lasers Under Strong Optical Injection," *IEEE J. Sel. Top. Quantum Electron.*, vol. 15, no. 3, pp. 572–577, 2009.
- [26] P. E. Morrissey, W. Cotter, D. Goulding, B. Kelleher, S. Osborne, H. Yang, J. O'Callaghan, B. Roycroft, B. Corbett, and F. H. Peters, "On-chip optical phase locking of single growth monolithically integrated slotted fabry perot lasers," *Opt. Express*, vol. 21, no. 14, p. 17315, Jul. 2013.
- [27] A. Chen and E. J. Murphy, *Broadband optical modulators : science, technology, and*

*applications*. CRC Press/Taylor & Francis Group, 2012.

- [28] G. T. Reed, G. Mashanovich, F. Y. Gardes, and D. J. Thomson, "Silicon optical modulators," *Nat. Photonics*, vol. 4, no. 8, pp. 518–526, Aug. 2010.
- [29] N. (Nadir) Dagli, *High-speed photonic devices*. Taylor & Francis, 2007.
- [30] W. Franz, "Einfluß eines elektrischen Feldes auf eine optische Absorptionskante," *Zeitschrift für Naturforsch. A*, vol. 13, no. 6, pp. 484–489, Jan. 1958.
- [31] L. V Keldysh, "THE EFFECT OF A STRONG ELECTRIC FIELD ON THE OPTICAL PROPERTIES OF INSULATING CRYSTALS," *J. Exptl. Theor. Phys.*, vol. 34, no. 34, pp. 1138–1141, 1958.
- [32] I. A. Merkulov and V. I. Perel', "Effects of electron-hole interaction on electro absorption in semiconductors," *Phys. Lett. A*, vol. 45, no. 2, pp. 83–84, Sep. 1973.
- [33] J. D. Dow and D. Redfield, "Electroabsorption in Semiconductors: The Excitonic Absorption Edge," *Phys. Rev. B*, vol. 1, no. 8, pp. 3358–3371, Apr. 1970.
- [34] D. A. B. Miller, "Band-Edge Electroabsorption in Quantum Well Structures: The Quantum-Confined Stark Effect," *Phys. Rev. Lett.*, vol. 53, no. 22, p. 2173, 1984.
- [35] M. U. Sadiq, M. R. Gleeson, N. Ye, J. O'Callaghan, P. Morrissey, H. Y. Zhang, K. Thomas, A. Gocalinska, E. Pelucchi, F. C. G. Gunning, B. Roycroft, F. H. Peters, and B. Corbett, "10 Gb/s InP-based Mach-Zehnder modulator for operation at 2  $\mu\text{m}$  wavelengths," *Opt. Express*, vol. 23, no. 9, p. 10905, May 2015.
- [36] "[http://www.globalspec.com/RefArticleImages/C3B67686880D71FB52B40587B7F17A/C4\\_12\\_12\\_23.gif](http://www.globalspec.com/RefArticleImages/C3B67686880D71FB52B40587B7F17A/C4_12_12_23.gif)." .
- [37] C. L. M. Daunt, J. O'Callaghan, K.-H. Lee, H. Yang, R. J. Young, K. Thomas, E. Pelucchi, B. Corbett, and F. H. Peters, "Compact Electroabsorption Modulators for Photonic Integrated Circuits, Using an Isolated Pedestal Contact Scheme," *IEEE Photonics Technol. Lett.*, vol. 24, no. 5, pp. 356–358, Mar. 2012.
- [38] W. Bogaerts, D. Taillaert, B. Luyssaert, P. Dumon, J. Van Campenhout, P. Bienstman, D. Van Thourhout, R. Baets, V. Wiaux, and S. Beckx, "Basic structures for photonic integrated circuits in Silicon-on-insulator," *Opt. Express*, vol. 12, no. 8, p. 1583, Apr. 2004.

- [39] S. Tanaka, S.-H. Jeong, S. Sekiguchi, T. Kurahashi, Y. Tanaka, and K. Morito, "High-output-power, single-wavelength silicon hybrid laser using precise flip-chip bonding technology," *Opt. Express*, vol. 20, no. 27, p. 28057, Dec. 2012.
- [40] M. J. R. Heck, J. F. Bauters, M. L. Davenport, J. K. Doylend, S. Jain, G. Kurczveil, S. Srinivasan, Y. Tang, and J. E. Bowers, "Hybrid Silicon Photonic Integrated Circuit Technology," *IEEE J. Sel. Top. Quantum Electron.*, vol. 19, no. 4, pp. 6100117–6100117, Jul. 2013.
- [41] P. V. Studenkov, M. R. Gokhale, J. C. Dries, and S. R. Forrest, "Monolithic integration of a quantum-well laser and an optical amplifier using an asymmetric twin-waveguide structure," *IEEE Photonics Technol. Lett.*, vol. 10, no. 8, pp. 1088–1090, Aug. 1998.
- [42] H. Wang, J. Yuan, P. J. van Veldhoven, T. de Vries, B. Smalbrugge, E. J. Geluk, E. A. J. M. Bente, Y. S. Oei, M. K. Smit, S. Anantathanasarn, and R. Nötzel, "Butt joint integrated extended cavity InAs/InP (100) quantum dot laser emitting around 1.55 [micro sign]m," *Electron. Lett.*, vol. 44, no. 8, p. 522, 2008.
- [43] S. Mokkalapati, H. H. Tan, and C. Jagadish, "Integration of an InGaAs quantum-dot laser with a passive waveguide using selective-area MOCVD," in *2005 IEEE LEOS Annual Meeting Conference Proceedings, 2005*, pp. 915–916.
- [44] H. Park, A. Fang, S. Kodama, and J. Bowers, "Hybrid silicon evanescent laser fabricated with a silicon waveguide and III-V offset quantum wells.," *Opt. Express*, vol. 13, no. 23, pp. 9460–4, Nov. 2005.
- [45] M. Smit, X. Leijtens, and E. Bente, "A generic foundry model for InP-based photonic ICs," in *Optical Fiber Communication Conference and Exposition (OFC/NFOEC), 2012 and the National Fiber Optic Engineers Conference, 2012*.
- [46] L. A. Coldren, S. C. Nicholes, L. Johansson, S. Ristic, R. S. Guzzon, E. J. Norberg, and U. Krishnamachari, "High Performance InP-Based Photonic ICs—A Tutorial," *J. Light. Technol.*, vol. 29, no. 4, pp. 554–570, Feb. 2011.
- [47] J. K. Alexander, P. E. Morrissey, H. Yang, M. Yang, P. J. Marraccini, B. Corbett, and F. H. Peters, "Monolithically integrated low linewidth comb source using gain switched slotted Fabry-Perot lasers."
- [48] P. Munoz, D. Pastor, and J. Capmany, "Modeling and design of arrayed waveguide

gratings," *J. Light. Technol.*, vol. 20, no. 4, pp. 661–674, Apr. 2002.

- [49] W. Cotter, D. Goulding, B. Roycroft, J. O'Callaghan, B. Corbett, and F. H. Peters, "Investigation of active filter using injection-locked slotted Fabry–Perot semiconductor laser," *Appl. Opt.*, vol. 51, no. 30, p. 7357, Oct. 2012.



## Chapter 3

# Photolithographic Mask and Semiconductor

## Process Design

### 3.1 Introduction

Photonic device fabrication involves the sequential application of a series of processing techniques (which are collectively referred to as a layer stack) to create complex topographies. This chapter outlines the design software and processing techniques used in the fabrication of the devices and circuits discussed in this thesis. This work was carried out in the III-V clean room at Tyndall National Institute, Cork using standard UV contact lithography, and monolithic regrowth free epitaxy to reduce process complexity, thus minimising fabrication cost.

### 3.2 Photolithographic Mask Design

Common layout editors such as Clewin [1], L-Edit [2] and KLayout [3] offer a simple interface for designing simple photonic devices. These pieces of software function similarly to a simple drawing program where the user adds simple geometric shapes together layer by layer to form structures. However, this becomes very tedious when forming large structures such as arrayed waveguide gratings (AWGs) or a dense multi-level PIC with many components. There are also commercial packages which specialize in PIC design such as Luceda [4] and Phoenix [5]. These packages allow the user to arrange predesigned components into circuits by assuming a fabrication process based on process design kits (PDKs) related to specific foundries.

An alternative software tool called PICDraw [6] has previously been developed in the Integrated Photonics Group at Tyndall for photolithographic mask design. Unlike other layout packages the user interacts with it entirely through written code, defining each component mathematically. This algorithm based approach to circuit design offers significant advantages arising from the efficiency with which alterations can be made to even the most complicated of circuits. For example, any changes to

bend radius, component length etc. will result in an automatic update to the entire layout. This is very significant when at the prototype level of PIC design, where designs and structures can change rapidly during development. Examples of such structures are shown in Figure 3.1.

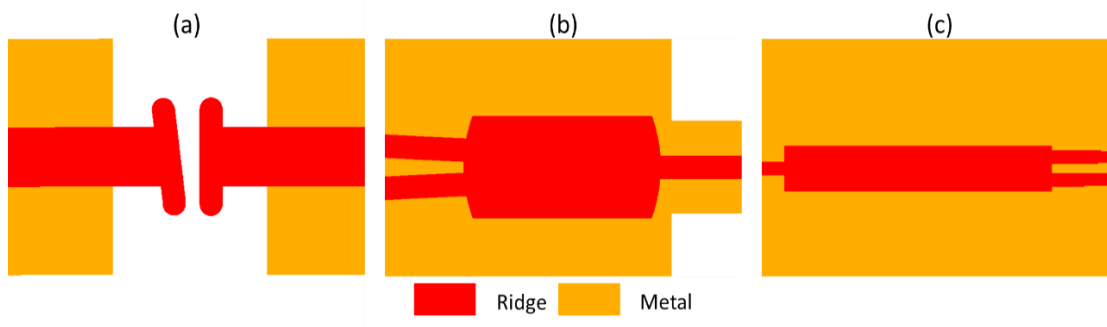


**Fig. 3.1:** Schematic of cells containing a (a) T bar slot (b) 2x1 star coupler (c) 1x2 MMI.

PICDraw is designed around the premise of a cell, which it inherited from the standard GDSII file format. Each component, consisting of multiple layers is placed in a unique cell. These cells can in turn be linked or cascaded to create complex integrated circuits. Devices and structures ranging in complexity from simple T bar slots to arrays of high speed Mach-Zehnder modulators have been designed and implemented using this approach (Figure 3.2).

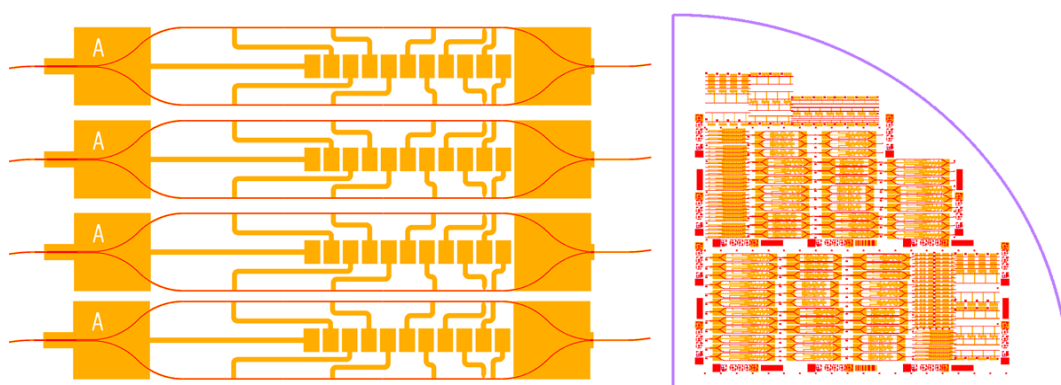


**Fig. 3.2:** Schematic of an array of PICs and a quarter wafer layout superimposing mask levels.

At the design stage, PICDraw produces a GDSII file with all the layers superimposed on top of each other, providing a convenient way to visually monitor how the design



is progressing. Once the wafer design has been finalised, PICDraw arranges the layers into a plate format suitable for mask ordering (Figure 3.3).

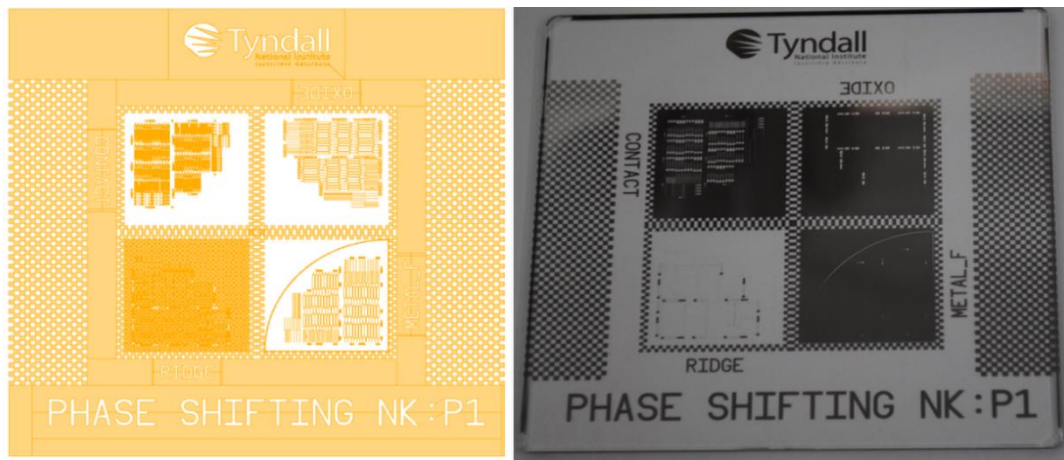


**Fig. 3.3:** PICDraw layout and microscopic image of photolithographic mask plate.

### 3.3 Self-Aligned deep and shallow etch process.

A requirement for the realisation of the CoWDM PIC outlined in Chapter 2 is the ability to integrated shallow etched (rib waveguide) and deep etched (ridge waveguide) structures. Current SFP laser designs are based on rib waveguides to minimise scattering losses while the higher optical confinement of the ridge structure enables waveguides with a smaller bend radius. As the work described in this thesis utilised contact lithography, considerations needed to be given to the transition between the shallow and deep etched regions. Defining the rib and ridge waveguides in separate lithographic steps was deemed inappropriate as any misalignment would result in significant optical losses due to mode mismatch. Therefore, a self-aligned process was developed to improve alignment tolerances and thus maximise device performance and yield.

This process begins with the deposition and patterning of silicon dioxide ( $\text{SiO}_2$ ), which defines the regions that will remain unetched throughout, Figure 3.4a. Next, a layer of silicon nitride ( $\text{SiN}_x$ ) is deposited on top of the patterned  $\text{SiO}_2$  prior to any etching of the semiconductor layers. The  $\text{SiN}_x$  is patterned using a  $\text{CF}_6$  based dry etch which has a high selectivity over  $\text{SiO}_2$  (>10:1), denoting the area that will be deep etched. This selective etch means that the nitride can be fully removed from sections with negligible effect to the underlying  $\text{SiO}_2$ , Figure 3.4b. It is this

combination of dielectrics, which are used to define the layout and topography of the devices that creates a process which is resilient to lithographic misalignment. The next stage of the process is to dry etch the semiconductive material to a depth just above the intrinsic region, Figure 3.4c. The silicon nitride is then stripped using the same selective  $CF_4$  dry etch as before, exposing any underlying  $SiO_2$ , Figure 3.4d. Afterwards, the semiconductor dry etch is continued, simultaneously defining the ridge waveguide structures while extending the pre-existing deep etch. Upon completion of this step, the deep waveguide has a depth just above the intrinsic region while the downmost etch has penetrated through the quantum wells and into

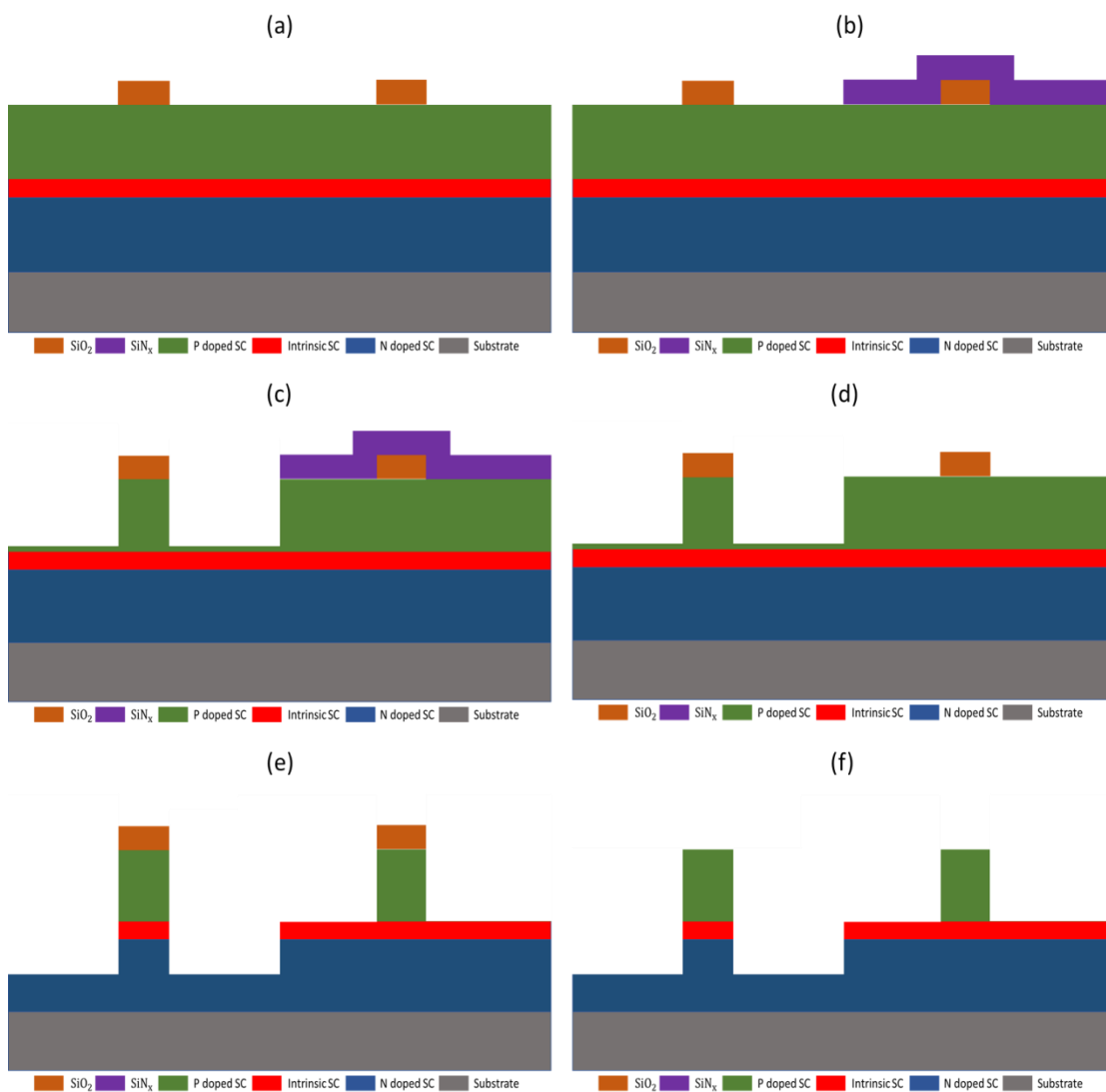


**Fig. 3.4:** Schematic of the self-aligned deep and shallow etch process.

the n doped layers, Figure 3.4e. Finally, the SiO<sub>2</sub> hard mask is removed using a hydrofluoric acid (HF) based buffered oxide etchant (BOE), Figure 3.4f. BOE was favoured over dry etching alternatives as it inflicts less damage to the underlying semiconductor when compared with plasma etching. This preservation of the upper p doped semiconductor layers facilitates the formation of a low resistance ohmic metal contact.

### **3.4 DC Process**

This section will outline the process used in the fabrication of the wide range of test structures, devices and photonics circuits detailed in chapters 4 and 6. This approach utilised the self-aligned deep and shallow etched process producing devices suitable for DC to 5.5 GHz applications.

#### **3.4.1 SiO<sub>2</sub> Deposition and Patterning**

As discussed in the previous section, the first step in the self-aligned process is to deposit and pattern a layer of SiO<sub>2</sub> to create the first level of the hard mask required for epitaxial etching. All dielectrics in this work were deposited by means of plasma enhanced chemical vapour deposition (PECVD) as it causes minimal damage to the semiconductor surface when compared with more physical techniques such as dielectric sputtering. Thin films of SiO<sub>2</sub> are grown by introducing silane and nitrous oxide to a combination of RF signals. A 13.56 MHz RF signal is applied to the electrodes to produce ions and therefore create a plasma while a lower frequency of 260 kHz is applied to the chuck to accelerate the ions towards the material. Microdeposit<sup>TM</sup> S1800 photoresists are used extensively in this work due to their UV contact lithography compatibility, resistance to dry etching and application in lift off lithography for metal patterning. Hexamethyldisilazane (HMDS) is an adhesion promoter which is recommended when depositing photoresists onto dielectrics. Inductively coupled plasma (ICP) etching is a technique used to remove a wide variety of semiconductor and dielectric materials. It produces very high plasma densities by means of an RF magnetic field which results in isotropic etch profiles. The gases used to etch SiO<sub>2</sub> are CF<sub>4</sub>/CHF<sub>3</sub> Ratio (3:7) with a 74.4 W platen power.

Finally, 1165 is a solvent commonly used for stripping photoresists from sensitive substrates. The process is as follows:

1. PECVD deposition of 400 nm  $\text{SiO}_2$ .
2. Static spin HMDs 4000 rpm 60 seconds.
3. Static spin S1813 4000 rpm 60 seconds.
4. Prebake at 115C 60 seconds.
5. UV exposure 7.5 seconds.
6. Develop in MF319 25 seconds.
7. Pattern  $\text{SiO}_2$  using  $\text{CF}_4$  based ICP etch.
8. 50 W  $\text{O}_2$  Plasma 60 seconds.
9. S1813 removal using 1165 at 90C.

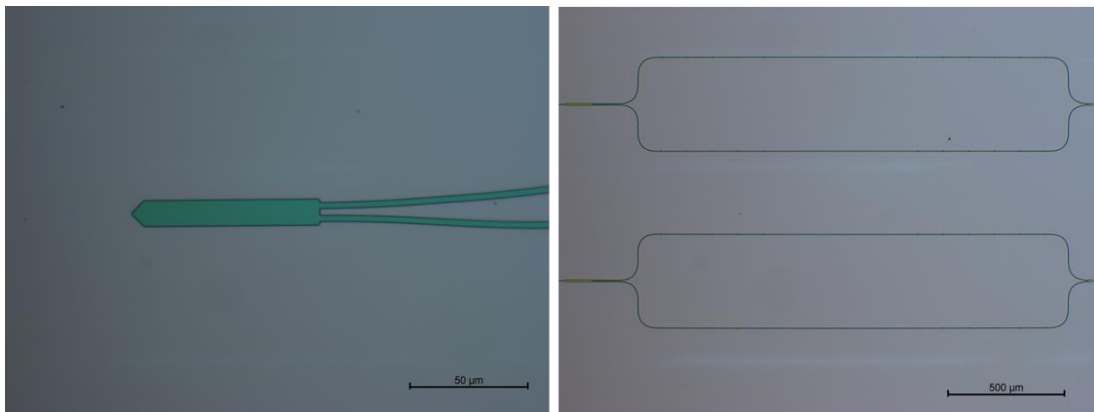


**Fig. 3.5:** Microscopic images of silicon dioxide patterning.

### 3.4.2 $\text{SiN}_x$ Deposition and Patterning

The second stage of the hard mask formation begins with the deposition of  $\text{SiN}_x$  by means of PECVD using silane, ammonia and nitrogen. The remainder of this step is quite similar to the previous one with a key exception being the ICP etch used to pattern the  $\text{SiN}_x$  is based on  $\text{CF}_6$  instead of  $\text{CF}_4$  with a platen power of 10W. This change in chemistry combined with a lower RF power produces an etch with a high selectivity of  $\text{SiN}_x$  over  $\text{SiO}_2$ . As previously stated, this means that the  $\text{SiN}_x$  can be patterned without degrading any underlying  $\text{SiO}_2$ .

1. PECVD deposition of 400 nm  $\text{SiN}_x$ .
2. Static spin HMDs 4000 rpm 60 seconds.

3. Static spin S1813 4000 rpm 60 seconds.
4. Prebake at 115C 60 seconds.
5. UV exposure 7.5 seconds.
6. Develop in MF319 25 seconds.
7. Pattern  $\text{SiN}_x$  using  $\text{CF}_6$  based ICP etch.
8. 50 W  $\text{O}_2$  Plasma 60 seconds.
9. S1813 removal using 1165 at 90C.

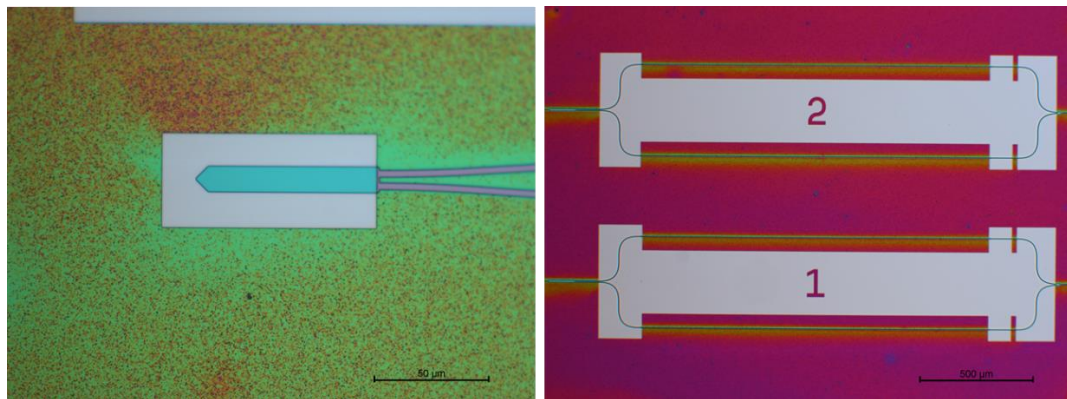


**Fig. 3.6:** Microscopic images of silicon nitride patterning.

### 3.4.3 First Etch and Silicon Nitride Removal

Now that the two hard masks have been patterned, the semiconductor dry etching can begin. Both semiconductor etches were achieved using a  $\text{Cl}_2/\text{CH}_4/\text{H}_2$  (Ratio 10:8:4) ICP etch. The first etch stops in the p doped layers at a depth of approximately 1.6 µm. The remainder of the  $\text{SiN}_x$  hardmask is then removed with the selective  $\text{CF}_6$  ICP etch.

1. Semiconductor etch using ICP etch.
2. Removal of remaining  $\text{SiN}_x$  using  $\text{CF}_6$  ICP etch.

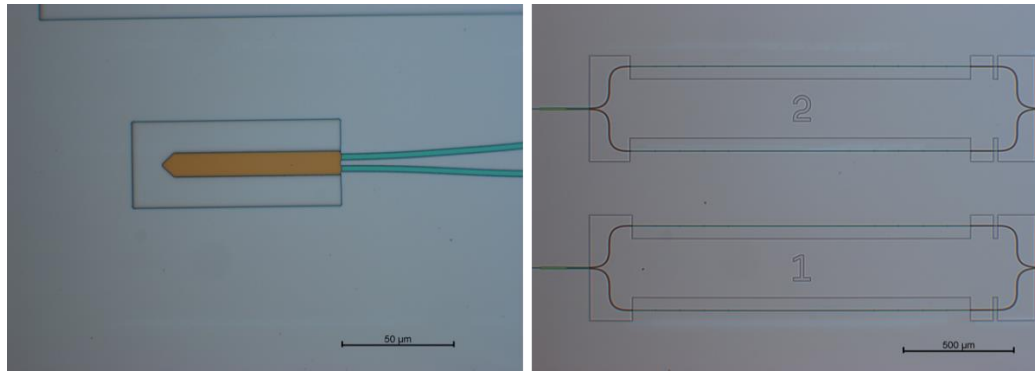


**Fig. 3.7:** Microscopic images first semiconductor etch.

### 3.4.4 Second Etch and SiO<sub>2</sub> Removal

The second Cl<sub>2</sub>/CH<sub>4</sub>/H<sub>2</sub> etch defines the ridge waveguides with a depth of 1.8 μm while extending the pre-existing trenches through the quantum wells and into the n doped layers. The remaining SiO<sub>2</sub> hard mask is removed using the CF<sub>4</sub> ICP etch completing the shaping for the semiconductor topography.

1. Semiconductor etch using ICP etch.
2. Removal of remaining SiO<sub>2</sub> using CF<sub>4</sub> ICP etch.

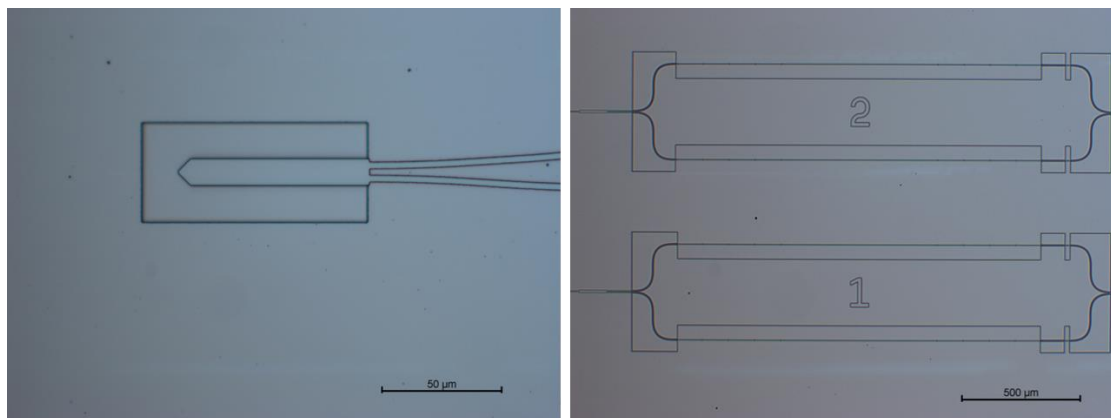


**Fig. 3.8:** Microscopic images second semiconductor etch.

### 3.4.5 Deposition and Patterning of SiO<sub>2</sub> Sidewall Passivation Layer and ridge opening.

Since the photonic devices and integrated circuits in this thesis have been fabricated using monolithic, regrowth free epitaxy, all sections need to be biased to transparency to minimize absorption losses. To facilitate the necessary contact pads,

the sidewalls of the structures need to be passivated to prevent the metal from shorting the various semiconductor layers. This is achieved by depositing a layer of  $\text{SiO}_2$  over the entire wafer and creating openings for the metal pads to contact the semiconductor p and n layers as required.

1. PECVD deposition of 400 nm  $\text{SiO}_2$ .
2. Static spin HMDs 4000 rpm 60 seconds.
3. Static spin S1813 4000 rpm 60 seconds.
4. Prebake at 115C 60 seconds.
5. UV exposure for 7.5 seconds.
6. Develop in MF319 25 seconds.
7. Pattern  $\text{SiO}_2$  using  $\text{CF}_4$  based ICP etch.
8. 50 W  $\text{O}_2$  Plasma 60 seconds.
9. S1813 removal using 1165 at 90C.

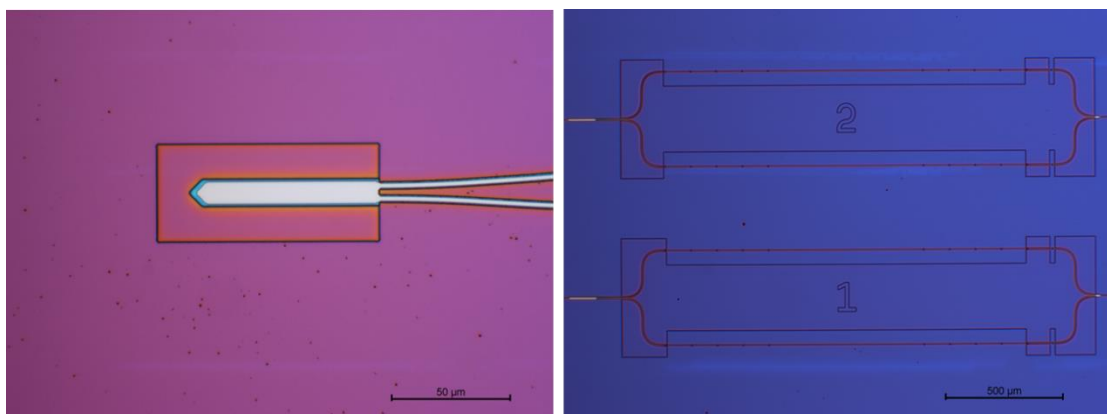


**Fig. 3.9:** Microscopic images side wall passivation and ridge opening.

### 3.4.6 P Contact Metal Deposition

Titanium and gold were deposited by standard lift-off lithography and e-beam evaporation to form contacts on the surface of the chip. A 360-degree rotational tool was used to ensure the metal ran continuously up the sidewall of the structures, reducing potential metal breaks. The lift-off lithography consisted of the deposition of LOR10A (a pre-exposed photoresist) with S1813 spun on top. While the resists are being developed, the S1813 patterns as normal. However, since the LOR10A is pre-exposed, it develops isotropically underneath the other resist creating an undercut.

The metal layer was then deposited on top of the two patterned resists. To finish the lift-off process, the wafer was placed in 1165, which aided by the undercut removed the resists and any unwanted metal.

1. Static spin HMDs 4000 rpm 60 seconds.
2. Static spin LOR10A 4000 rpm 60 seconds.
3. Prebake at 150C 180 seconds.
4. Static spin HMDs 4000 rpm 60 seconds.
5. Static spin S1813 4000 rpm 60 seconds.
6. Prebake at 115 C 60 seconds.
7. UV exposure 7.5 seconds.
8. Develop in MF31990 seconds.
9. BOE wet etch 25 seconds.
10. E-beam deposition of Ti:Au metal.
11. Metal lift off in 1165 at 90 C.

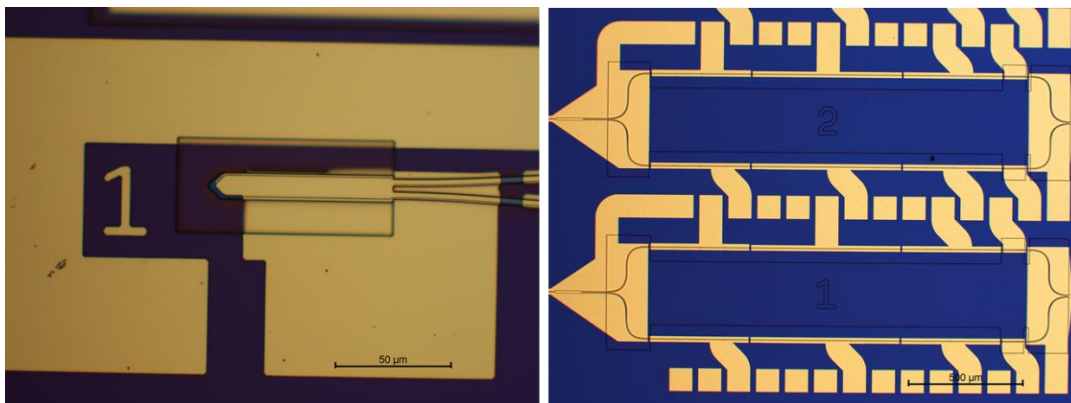


**Fig. 3.10:** Microscopic images contact metal pads.

### 3.4.7 Wafer Thinning, N metal Deposition and Cleaving

To characterize the fabricated devices, it was necessary to couple light out via cleaved facets. To achieve this, the wafer must be first thinned to ensure that the break occurs along the crystalline axis, creating a high quality optical interface. To this end, the substrate was chemically thinned to a thickness of 100 μm. This is achieved by mounting the wafer face down onto a glass slide and suspending it in a bromine methanol solution. The backside of the wafer is mechanical polished prior



to suspension to remove any contaminants that may have formed during the previous steps. The black wax used to adhere the sample to the glass slide also protects the processed epitaxy during this stage. As the substrate is n doped, it was then possible to load the sample into an e beam evaporator to form a n contact metal on the backside of the chip. Finally, the wafer is removed from the glass slide using Toluene and is cleaved into testable bars.

1. Fix wafer to glass slide (epitaxy face down) using black wax.
2. Mechanically polish back side of wafer.
3. Thin wafer to 100  $\mu\text{m}$  using bromine methanol.
4. E-beam deposition of Ti:Au metal.
5. Remove from glass slide using Toluene.
6. Cleave wafer into testable bars.

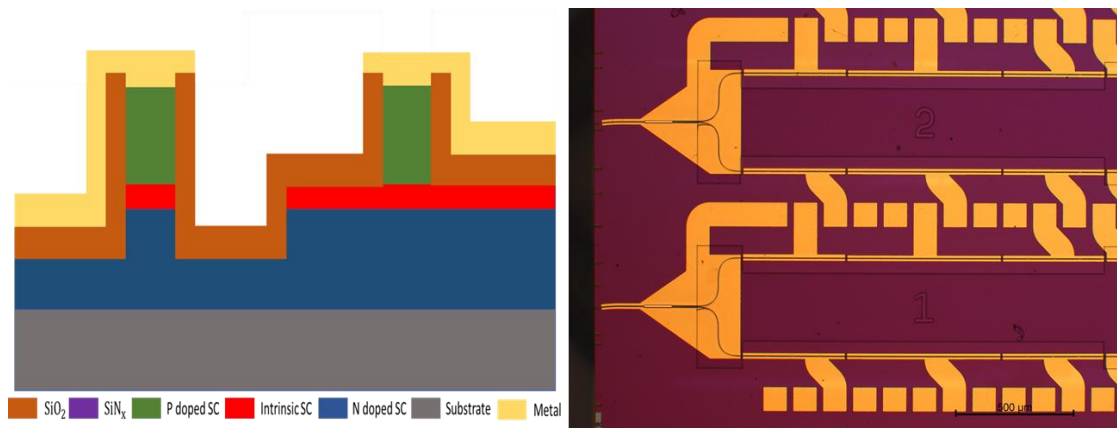


**Fig. 3.11:** Cross section and microscopic image of completed device.

### 3.5 High Speed Process

This section outlines the process used to fabricate the electroabsorption modulators discussed in Chapter 5. It centres on the formation of isolated pedestal contacts, which result in a significant reduction of the parasitic capacitance of the bond pads, thus enabling much higher speeds than the 5.5 GHz limitation of the DC process. Another major consideration in the fabrication of high speed devices is the quality of the metal contacts. High contact resistances can severely impact on a device's ability to function at high modulation speeds. This is particularly true for the p metal contacts which naturally have a higher resistance due to the smaller contact surface

area. To this end, the high-speed process begins with the deposition of a thin ridge metal on the pristine semiconductor surface to ensure an optimal contact. The next challenge is in protecting the quality of this ridge metal throughout the numerous etches that follow. This was achieved with the use of a composite hard mask for the various etches. A thin layer of silicon dioxide is deposited over the surface of the wafer, covering the ridge metals. As this layer is too thin to withstand the plasma, a thick silicon nitride layer is also deposited (Figure 3.12a). The patterning of this composite hard mask is identical to that of a single layer mask. However, after the etch the remaining silicon nitride can be removed using the selective  $\text{CF}_6$  dry etch (Figures 3.12b and 3.12c). In this way, the silicon nitride mask can be removed and replaced multiple times with no effect to the underlying silicon dioxide and metal (Figures 3.12d and 3.12e). Upon completion of the semiconductor etching, the thin  $\text{SiO}_2$  layer can be removed using a dilute BOE solution. This reveals the protected ridge making it possible to form contact pads suitable for DC and RF characterisation (Figure 3.12f).

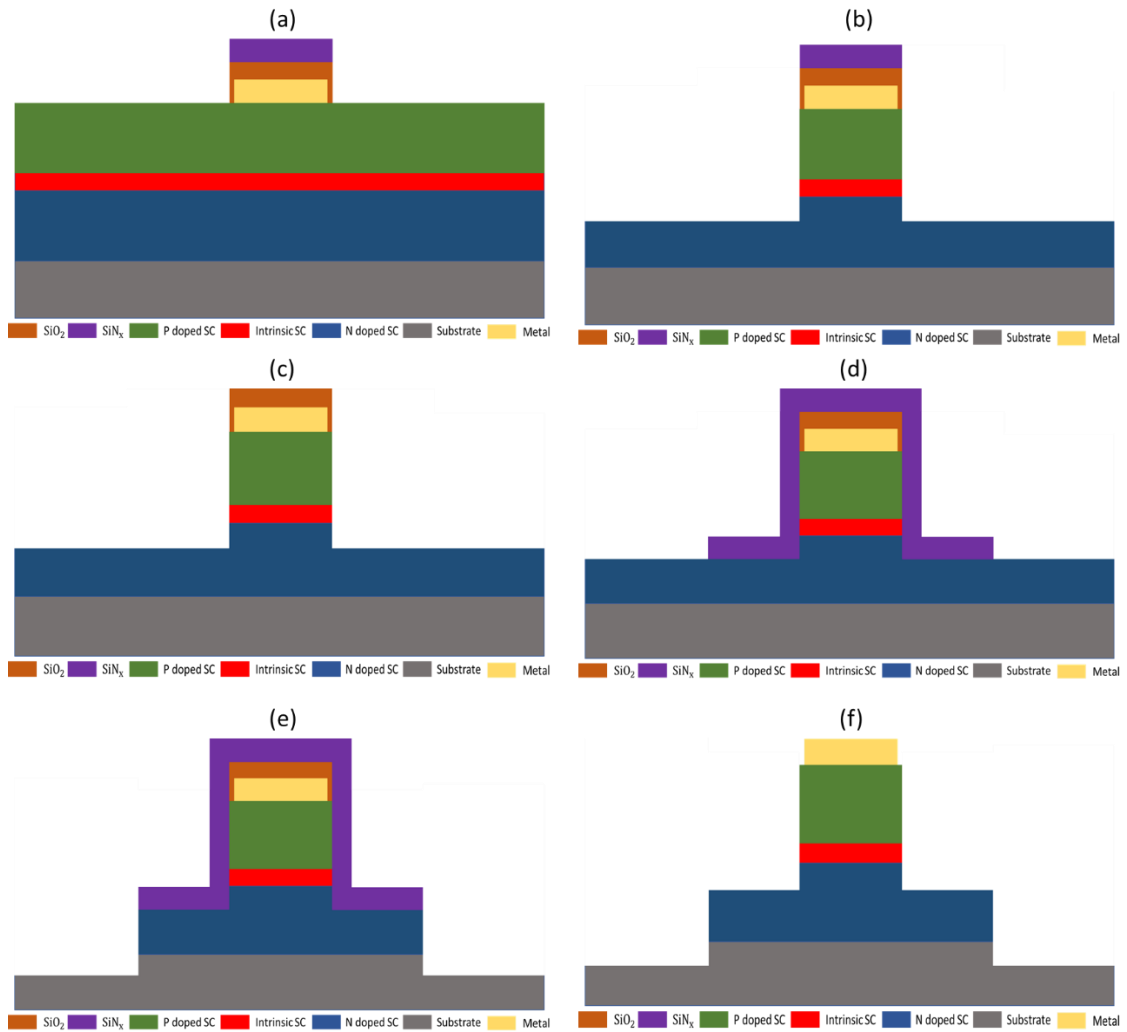


**Fig. 3.12:** Schematic illustrating the use of a composite hard mask to protect the ridge metal during multiple etches.

### 3.5.1 P Contact Metal Deposition

A ridge P metal is deposited at the beginning of the process to ensure a high quality ohmic contact. Due to the relatively fine resolution requirements of this step, the thickness of the metal is limited to 120 nm to ensure a successful lift off. Gaps are patterned in the metal where the isolation slots will be formed. Exposure of even a small fraction of the metal trace to the semiconductor plasma etch can delaminate the entire strip.

1. Static spin HMDs 4000 rpm 60 seconds.
2. Static spin LOR3A 4000 rpm 60 seconds.
3. Prebake at 150C 180 seconds.

4. Static spin HMDs 4000 rpm 60 seconds.
5. Static spin S1805 4000 rpm 60 seconds.
6. Prebake at 115C 60 seconds.
7. UV exposure 7.5 seconds.
8. Develop in MF319 90 seconds.
9. BOE wet etch 10 seconds.
10. E-beam deposition of Ti:Au metal.
11. Metal lift off in 1165 at 90C.

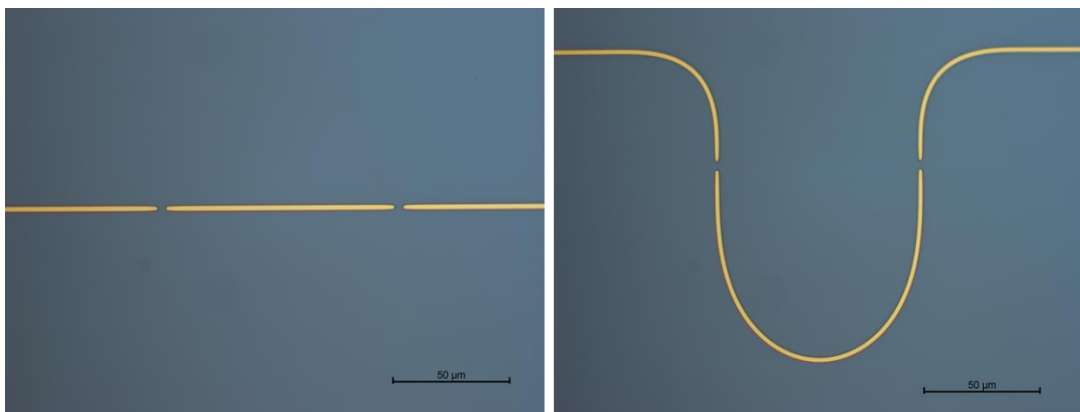


**Fig. 3.13:** Microscopic images of ridge P metal.

### 3.5.2 Isolation Slot Etch

This step forms 1  $\mu\text{m}$  wide slots in between the ridge metals which will electrically isolate the various sections. These slots are angled to minimise optical reflections. This process is done before the definition of the ridge waveguides as it would be challenging to achieve the necessary resolution afterwards due to the topography. Firstly, the composite hard mask is deposited and patterned. The exposed semiconductor layers are then etched to a depth of 1.8  $\mu\text{m}$  which is just above the quantum wells using the  $\text{Cl}_2/\text{CH}_4/\text{H}_2$  recipe. The remaining silicon nitride layer is then stripped using the selective  $\text{CF}_6$  etch.

1. PECVD deposition of 50 nm  $\text{SiO}_2$ .
2. PECVD deposition of 400 nm  $\text{SiN}_x$ .
3. Static spin HMDs 4000 rpm 60 seconds.
4. Static spin S1813 4000 rpm 60 seconds.

5. Prebake at 115 C 60 seconds.
6. UV exposure 7.5 seconds.
7. Develop in MF319 25 seconds.
8. Pattern hard mask using  $\text{CF}_4$  based ICP etch.
9. 50 W  $\text{O}_2$  Plasma 60 seconds.
10. S1813 removal using 1165 at 90 C.
11. Semiconductor etch using ICP etch.
12. Removal of remaining  $\text{SiN}_x$  using  $\text{CF}_6$  ICP etch.

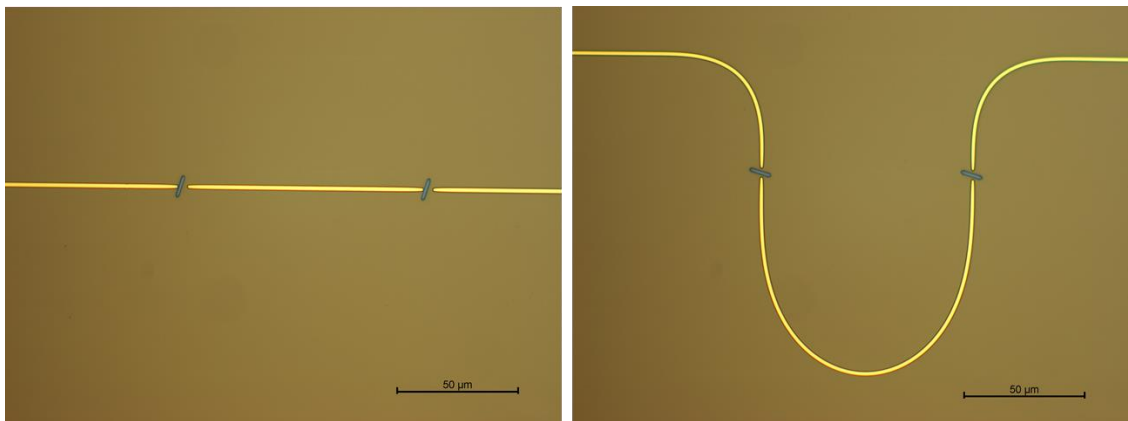


**Fig. 3.14:** Microscopic images of isolation slot formation.

### 3.5.3 Ridge and Pedestal Etch

A second  $\text{Cl}_2/\text{CH}_4/\text{H}_2$  dry etch penetrates through the quantum wells and into the N doped layers to form the ridge waveguides and contact pedestals. This step also serves to expose the N doped epitaxial layers for the formation of metal contacts. The remaining silicon nitride layer is again stripped using the selective  $\text{CF}_6$  etch.

1. PECVD deposition of 400 nm  $\text{SiN}_x$ .
2. Static spin HMDs 4000 rpm 60 seconds.
3. Static spin S1813 4000 rpm 60 seconds.
4. Prebake at 115C 60 seconds.
5. UV exposure 7.5 seconds.
6. Develop in MF319 25 seconds.
7. Pattern hard mask using  $\text{CF}_4$  based ICP etch.
8. 50 W  $\text{O}_2$  Plasma 60 seconds.

9. S1813 removal using 1165 at 90C.
10. Semiconductor etch using ICP etch.
11. Removal of remaining  $\text{SiN}_x$  using  $\text{CF}_6$  ICP etch.

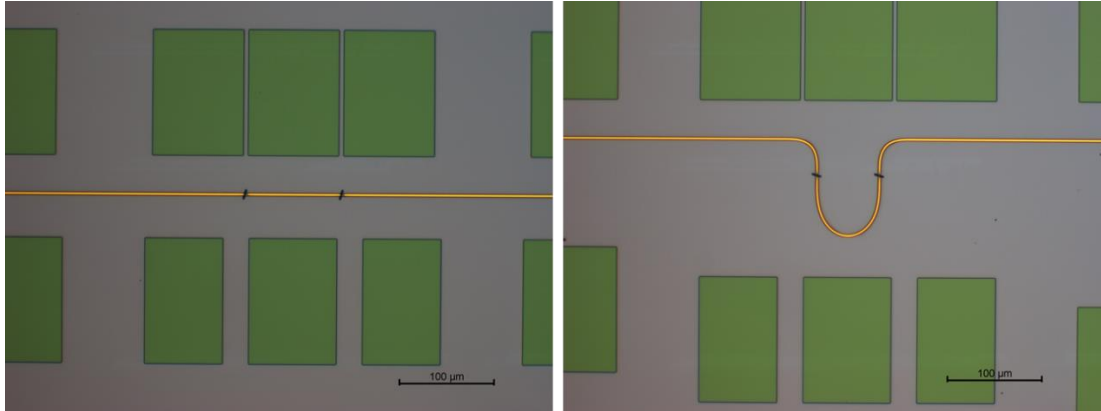


**Fig. 3.15:** Microscopic images of waveguide and pedestal formation.

#### 3.5.4 N Contact Metal Deposition

A series of metal pads are deposited directly onto the N semiconductor layers using standard lift-off lithography. The pads have a large surface area to minimise the resistance of the device. The metal is annealed at 380 C to form a high quality contact. Metal is also deposited on top of the pedestals to improve adhesion of the contact metal.

1. Static spin HMDs 4000 rpm 60 seconds.
2. Static spin LOR10A 4000 rpm 60 seconds.
3. Prebake at 150C 180 seconds.
4. Static spin HMDs 4000 rpm 60 seconds.
5. Static spin S1813 4000 rpm 60 seconds.
6. Prebake at 115C 60 seconds.
7. UV exposure 7.5 seconds.
8. Develop in MF319 90 seconds.
9. BOE wet etch 25 seconds.
10. E-beam deposition of Au/Ge/Au/Ni/Au metal.
11. Metal lift off in 1165 at 90C.
12. Anneal at 380C 5 min.

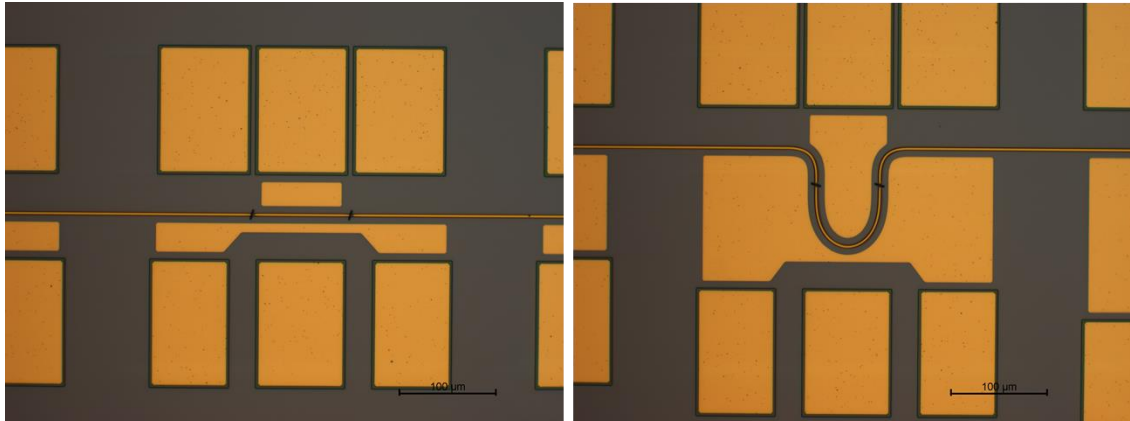


**Fig. 3.16:** Microscopic images of N metal contacts.

### 3.5.6 Isolation Trench

Next, an isolation trench into the semi-insulating substrate is formed. This trench surrounds the signal pedestal to minimise parasitic capacitances and resistance that can form between it and the ground pads. Unlike the previous etches, a  $\text{BCl}_3/\text{Ar}$  chemistry is used to etch into the substrate despite having a less than ideal sidewall profile. This is due to a study previously undertaken in Tyndall showing that the hydrogen present in the  $\text{Cl}_2/\text{CH}_4/\text{H}_2$  recipe passivates the iron dopant in the semi-conductive InP substrate. This passivation of the dopant makes the substrate conductive, rendering the isolation trench ineffective.

1. PECVD deposition of 400 nm  $\text{SiN}_x$ .
2. Static spin HMDs 4000 rpm 60 seconds.
3. Static spin S1813 4000 rpm 60 seconds.
4. Prebake at 115C 60 seconds.
5. UV exposure 7.5 seconds.
6. Develop in MF319 25 seconds.
7. Pattern hard mask using  $\text{CF}_4$  based ICP etch.
8. 50 W O2 Plasma 60 seconds.
9. S1813 removal using 1165 at 90C.
10. Semiconductor etch using ICP etcher.
11. Removal of remaining  $\text{SiN}_x$  using  $\text{CF}_6$  ICP etch.

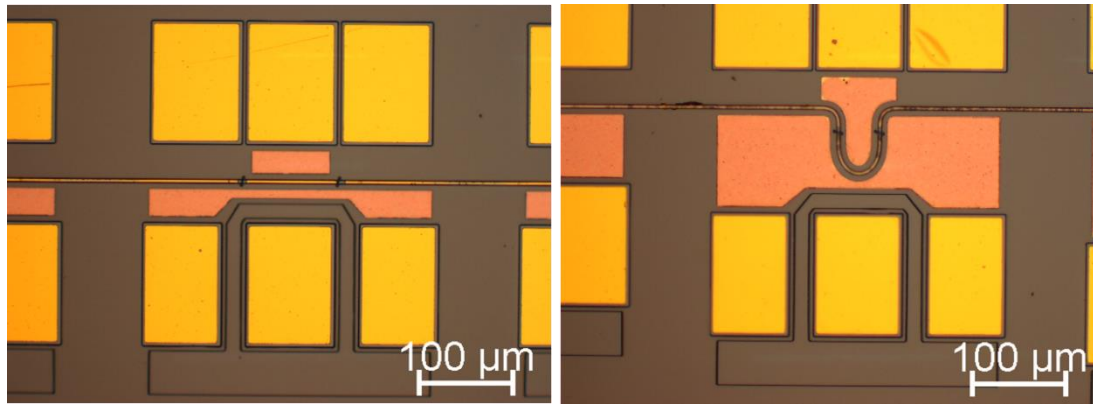


**Fig. 3.17:** Microscopic images of isolation trench formation.

### 3.5.7 BCB Deposition and Etch Back

Benzocyclobutene (BCB) is used as a support for the bridge metal that will link the signal pedestal to the ridge metal. It has a low dielectric constant, minimising parasitic capacitances which will limit device performance. This stage begins with the deposition of 400 nm of  $\text{SiN}_x$  which acts as a protective layer for the metals. BCB is dynamically spun onto the wafer with the aid of the adhesion promoter AP3000. The sample is then baked in an oven at low vacuum, curing the BCB while removing any bubbles that may become trapped within the layer. Once cured the BCB is then uniformly etched back so that the nitride covering the ridges and pedestals begins to protrude.

1. PECVD deposition of 400 nm  $\text{SiN}_x$ .
2. Dynamic spin AP3000 300 rpm 5 seconds, 3000 rpm 20 seconds.
3. Dynamic spin BCB 750 rpm 5s, 2500 rpm for 40s.
4. Cure BCB in oven at 210C 2 hours.
5. BCB etch back using ICP etcher.

### 3.5.7 BCB Shaping

As only the ridge and pedestals are protruding at this stage, the BCB must be shaped to access to the underlying N metal. Since the BCB etch has approximately a 1:1 selectivity over photoresists, a thick photoresist must be used to define the pattern. SPR220-4.5 has a thickness of 4.5  $\mu\text{m}$  with a vertical sidewall profile. After patterning, the protective nitride layer is removed from both the P and N metals



simultaneously using the  $\text{CF}_6$  selective etch. A short BOE dip gently removes the thin layer of  $\text{SiO}_2$  which has been present since step 2, exposing both metals.

1. Static spin HMDs 4000 rpm 60 seconds.
2. Static spin SPR220-4.5 3000 rpm 50 seconds.
3. Prebake at 115C 60 seconds.
4. UV exposure 40 seconds.
5. Hold for 35 mins.
6. Post exposure bake at 115C 90 seconds.
7. Develop in MF26A 35 seconds.
8. BCB etch using ICP etcher.
9. 50 W  $\text{O}_2$  Plasma 60 seconds.
10. SPR220-4.5 removal using 1165 at 90C.
11. Removal of  $\text{SiN}_x$  protective layer using  $\text{CF}_6$  ICP etch
12. Dilute BOE Wet Etch 20 sec

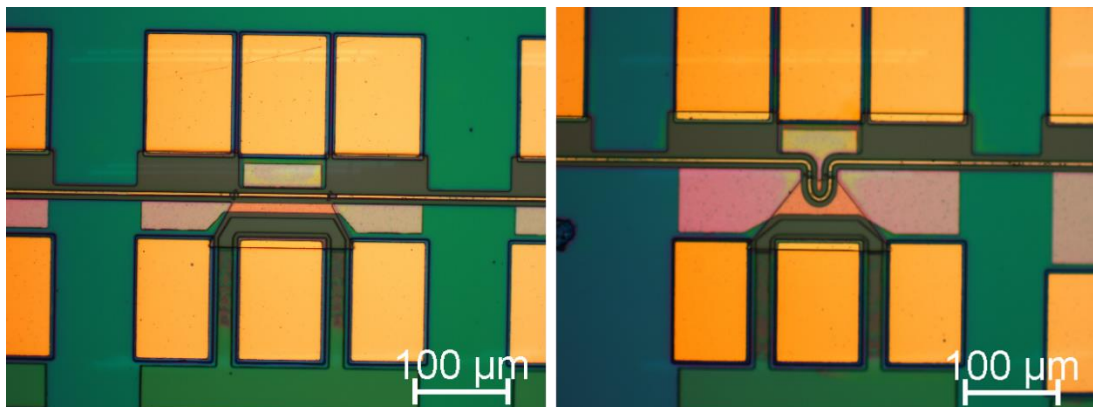


**Fig. 3.18:** Microscopic images of BCB shaping.

### 3.5.8 P Contact Metal Deposition

A contact metal is deposited to join the pedestals with the pre-existing P and N metals, facilitating the use of a GSG probe. The E-beam evaporation was done using 360 degree rotational tool to ensure the metal successfully traverses the topography without breakages.

1. Static spin HMDs 4000 rpm 60 seconds.
2. Static spin LOR10A 4000 rpm 60 seconds.

3. Prebake at 150C 180 seconds.
4. Static spin HMDs 4000 rpm 60 seconds.
5. Static spin S1813 4000 rpm 60 seconds.
6. Prebake at 115C 60 seconds.
7. UV exposure 7.5 second.
8. Develop in MF319 90 seconds.
9. BOE wet etch 25 seconds.
10. E-beam deposition of Ti/Au metal.
11. Metal lift off in 1165 at 90C.

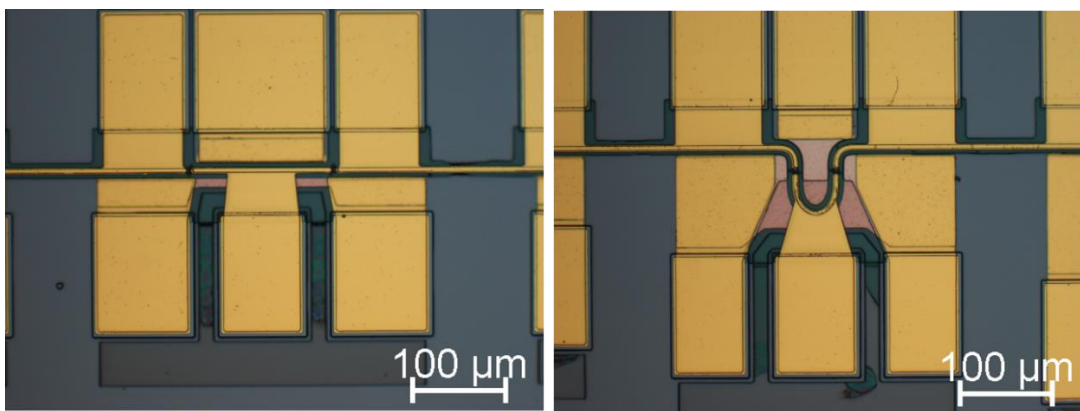


**Fig. 3.19:** Microscopic images of the contact metal.

### 3.5.9 Wafer Thinning, N metal Deposition and Cleaving

As with the DC process, the substrate was chemically thinned to a thickness of 100  $\mu\text{m}$ . The wafer was mounted face down onto a glass slide, mechanical polished and suspending it in a bromine methanol solution. Finally, the wafer was removed from the glass slide using Toluene and cleaved into testable bars.

1. Fix wafer to glass slide (epitaxy face down) using black wax.
2. Mechanically polish back side of wafer.
3. Thin wafer to 100  $\mu\text{m}$  using bromine methanol.
4. Remove from glass slide using Toluene.
5. Cleave wafer into testable bars.

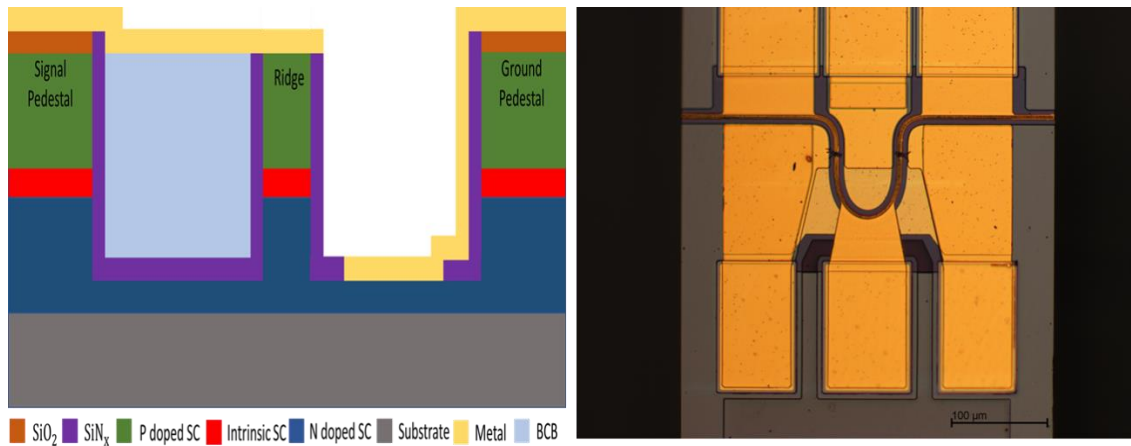


**Fig. 3.20:** Cross section and microscopic image of completed device.

### 3.6 Summary

This chapter discussed the design software and manufacturing techniques used in the manufacturing of the devices and circuits discussed in this thesis. Although common layout editors offer simple interfaces for photonic devices, an alternative software tool called PICDraw was favoured due to the efficiency with which alterations can be made to even the most complicated of circuits because of its algorithm based approach. A requirement for the realisation of a CoWDM PIC is the ability to integrate shallow etched (ridge waveguide) and deep etched (rib waveguide) structures. A DC process which utilises a composite hard mask approach to achieve a low loss transition between rib and ridge waveguides is also described. This process was used to produce a wide range of devices and circuits suitable for DC to 5.5 GHz applications. Finally, a high speed process which centred around the formation of isolated pedestal contacts to enable the devices to go at speeds which surpass the 5.5 GHz limitations of the DC process was also discussed. In the next chapter the DC process will be used in the development of various laser structures that were developed for integration into larger PICs

### Bibliography

- [1] "WieWeb software: Clewin." [Online]. Available: <http://www.wieweb.com/nojava/layoutframe.html>. [Accessed: 10-May-2017].
- [2] "Tanner L-Edit IC Layout - Mentor Graphics." [Online]. Available: <https://www.mentor.com/tannereda/l-edit>. [Accessed: 10-May-2017].

- [3] "KLayout Layout Viewer And Editor." [Online]. Available: <http://www.klayout.de/index.html>. [Accessed: 10-May-2017].
- [4] "Luceda | Software and services for integrated photonics designers." [Online]. Available: <http://www.lucedaphotonics.com/en>. [Accessed: 10-May-2017].
- [5] "Phoenix Software | Software, Hardware, EUC, IT Services." [Online]. Available: <https://www.phoenixs.co.uk/>. [Accessed: 10-May-2017].
- [6] "PICDraw Tyndall." [Online]. Available: <https://careers.tyndall.ie/content/phonic-integrated-circuits-pics>. [Accessed: 10-May-2017].

## Chapter 4

# Single Mode Laser based on Dual Port Multimode Interference Reflector

### 4.1 Introduction

Distributed feedback (DFB) and distributed Bragg reflector (DBR) lasers can provide stable single mode outputs suitable for optical communications [1],[2]. However, a disadvantage of these lasers is their fabrication complexity which requires the resolution of submicron features and epitaxial regrowth to create the necessary surface gratings. Slotted Fabry Perot lasers offer an alternative solution with lower fabrication complexity but the performance of the mirror sections is highly dependent on etch depth [3].

In this chapter, a regrowth free, single mode laser suitable for monolithic integration is proposed and demonstrated. The laser utilizes a dual port multimode interference reflector (MIR) and an etched facet to create a lasing cavity. A single deep etched slot produces single moded behavior with a side mode suppression ratio (SMSR) of 30dB. The performance of the dual port MIR and etched facet have little dependence on the etch depth when compared with the mirror sections of a slotted Fabry Perot laser [3]. This laser therefore, is ideal for use as a light source in complex integrated photonic circuits as it does not require reflections from a cleaved facet, providing flexibility in circuit layout/design. The epitaxial structure used was commercially grown 1550 nm laser material on an N doped InP substrate. It contained five compressively strained AlInGaAs quantum wells with a total active region thickness of 0.4  $\mu\text{m}$  (Appendix A.1).

### 4.2 Multimode Interference Devices

Multimode interference couplers (MMIs) provide an alternative to y-branch structures, directional couplers and star couplers in photonic devices and circuits. Such devices operate on the principal of self-imaging, in which an input field is

reproduced in single or multiple images at periodic intervals as it propagates along a multimode waveguide [4]. These self-images can be decoupled from the MMIs into output waveguides by optimizing the MMI dimensions such as width, length, and output waveguide separation. Advantages of MMIs include a wide spectral bandwidth, polarisation insensitivity, and compact size. Since MMIs are typically based on rectangular waveguides, two-dimensional mode solutions are required. The beam propagation method (BPM) is a computationally light method for solving intensity and modes within a waveguide structure and is formulated as a solution to the Helmholtz equation in a time-harmonic case [5]. A BPM simulation of a 1x2 MMI coupler is shown in Figure 4.1.

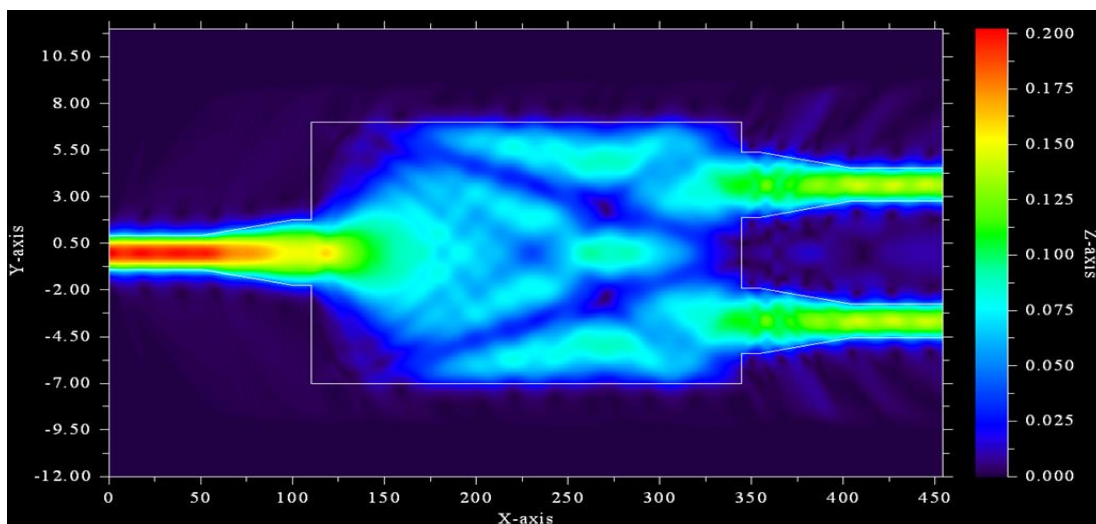


**Fig 4.1:** BPM simulation of 1x2 MMI coupler.

Reflective elements are an essential part of Fabry-Perot lasers and resonators. Cleaved and etched facet solutions are relatively easy to achieve, but a large quantity of light is transmitted and lost, which is undesirable when a one hundred percent reflector is preferred. Total internal reflection has the potential to offer higher reflection provided that the required critical angle of the interface does not exceed  $45^\circ$ . The critical angle for an InP air interface is  $< 30^\circ$  (assuming a group index of 3.16). Therefore, introducing two  $45^\circ$  deep etched mirrors into a single mode waveguide would in theory fully reflect the optical mode. However, the intersection point between the mirrors will round due to limits in lithographic resolution. As this rounding would occur where the mode intensity is a maximum,

significant losses would be incurred. An approach presented in [6] is to use the principle of self-imaging in multimode waveguides to ensure that a negligible amount of the optical power is present at the mirror intersection. These multimode interference reflectors (MIRs) are created by adapting MMI designs using  $45^\circ$  mirrors so that light is reflected and propagates back towards the input side of the device. Using MMI theory, the position of the images can be predicted and MIRs with high port numbers can be realised. The BPM simulation and SEM image of a 1 port MIR is shown in Figure 4.2. Single mode lasers based on MIRs [7] have been shown, integrating passive mirror sections and waveguides with active gain sections. These designs rely on preprocessing of the wafers using dry etching and selective regrowth to integrate active and passive epitaxy [8]. The devices are then defined using lithography and dry etching. This preprocessing of the wafers using epitaxial regrowth increases processing cost and duration [8].

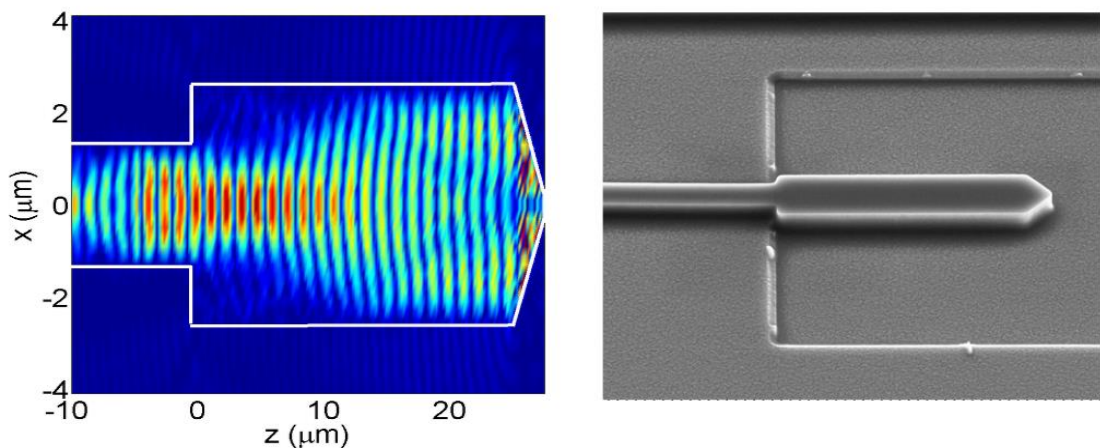


**Fig 4.2:** BPM simulation courtesy of Padraic Morrissey (left) and SEM image (right) of 1 port MIR [9].

### 4.3 Waveguide Slot Characterisation

Slots can be positioned along the ridge of a lasing cavity to alter the lasing spectrum [10], [11]. These slots provide secondary reflections within the cavity and light resulting from this feedback can either constructively or destructively interfere with the main modes, depending on the phase conditions. In this way, the resonance of the cavity can be influenced. As the slots are defined by etching into the waveguide, the effective index experienced by the optical mode changes as the mode

propagates into the etched region. The reflection coefficient experienced by a plane wave at normal incidence can be expressed as a function of the effective index in the ridge ( $n_1$ ) and the effective index in the slot ( $n_2$ ) [12].

$$r = \frac{n_1 - n_2}{n_1 + n_2}$$

Slots can also be added to electrically isolated sections so that they can be independently biased, leading to tunability of the laser's resonance. As part of this development of an MIR based facetless laser, Fabry-Perot lasers with various slot types were included on the mask. Their purpose was to examine the effect of the slots on the laser's output spectrum and thus identify the best design for electrical isolation and for use in a single mode device. The slot types investigated (Figure 4.3) include straight, angled, deep and an experimental double etched slot. The straight slots (where the etch stops above the active region) are shallow etched t-bars, identical to those commonly used in the slotted mirror sections of SFP lasers. Angle slots are shallow etched t-bars with a 7-degree angle to minimise reflections. They are designed to provide electrical isolation between sections while having minimal effect on the optical mode. Deep etched slots (where the etch penetrates through the active region) have the same shape as the straight slots but are defined using a deep etch which penetrates through the active region. As a result, they are expected to provide much higher reflection. They are however, dependent on the side wall profile of the etch and can be much lossier than shallow slots. An experimental double etched slot was also included whereby the waveguide changes abruptly from a shallow to a deep etched waveguide and back again.

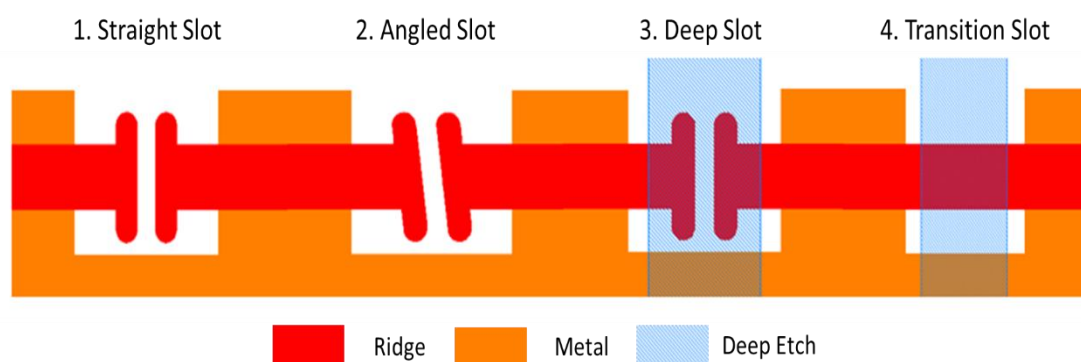


**Fig 4.3:** Schematic of slot designs.



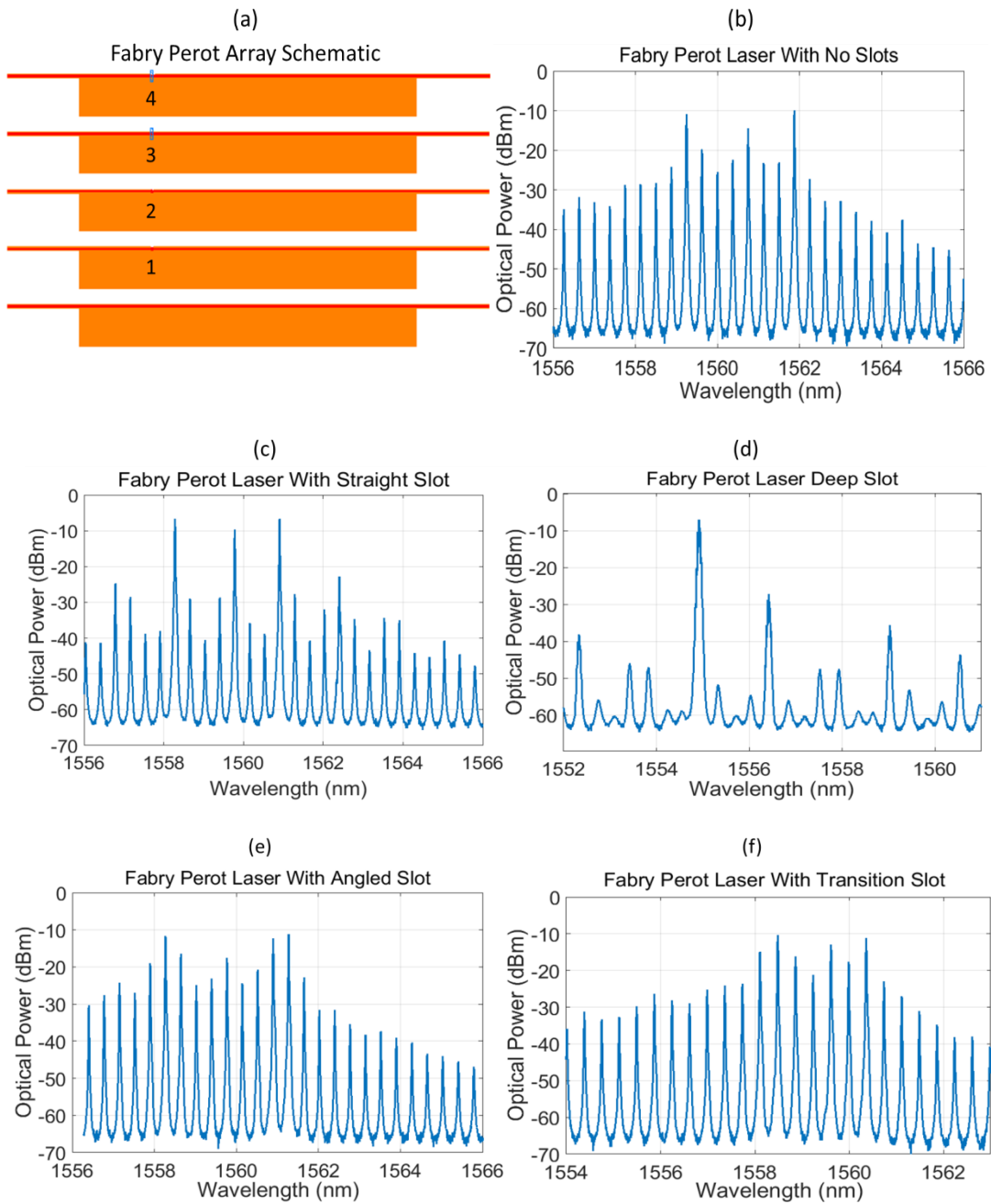


**Fig 4.4:** (a) Schematic of Fabry-Perot test structures with the numbers corresponding to the slot types illustrated in Figure 4.3 and (b-f) output spectra of the respective with various slot types.

The performance of the slots was compared by analysing the spectral properties of the corresponding lasers (Figure 4.4a). A Fabry-Perot with no slots was also included to act as a control for comparison (Figure 4.4b) as any internal reflection caused by the addition of a slot will result in extra resonances in the spectral output of the laser. While the shallow slot did perturb the Fabry-Perot spectrum (Figure 4.4c), the

deep slot provided much higher reflection making it a better choice when attempting to create a single mode laser with an individual slot (Figure 4.4d). The angled slot showed little effect on the lasing spectrum, confirming its suitability as an electrical isolator (Figure 4.4e). The transition slot showed no significant effect on the output spectrum, indicating that a negligible reflection level was achieved due to the mismatch as the mode transitioned from a rib to ridge section (Figure 4.4f).

#### 4.4 MIR Test Structures

An array of 400  $\mu\text{m}$  long Fabry Perot lasers with various reflectors at one end allowed for a comparison between the performances of a single port MIR and a metal coated etched facet. Two variations of the single port MIR were tested. One had metal deposited on the reflective mirrors while the other was designed so that the reflective mirrors were exposed.

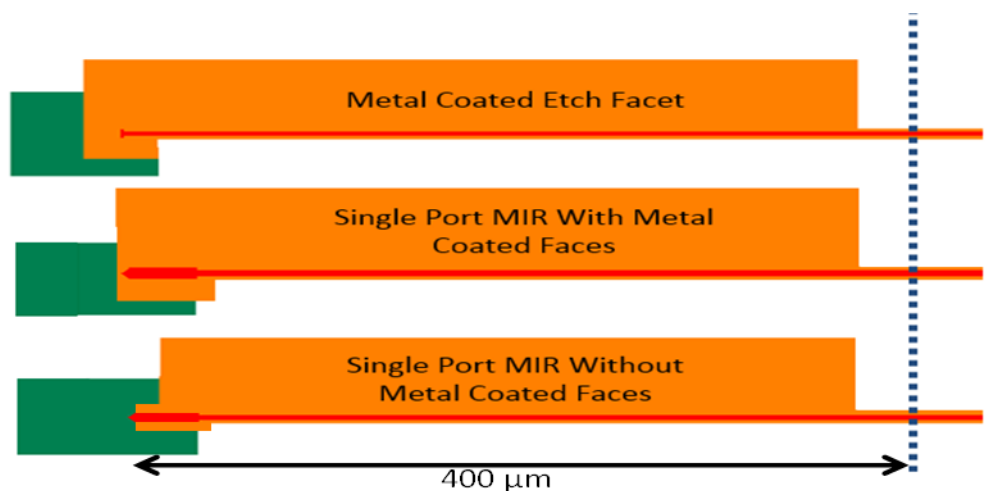


**Fig. 4.5:** Schematic of one port reflector test structures.

The width and length of the MIRs were 5  $\mu\text{m}$  and 25  $\mu\text{m}$  respectively. A schematic of these structures is shown in Figure 4.5. Each device was powered by a single probe and the output power was recorded while the current was swept from 0 to 50 mA (Figure 4.6). With a threshold current of 14 mA, the etched facet showed superior performance to both single port MIR variations. Hence, the etched facet was favoured for the laser design. The lower reflectivity of the single port MIRs was

attributed to sidewall roughness of the reflective surfaces which introduced scattering losses.

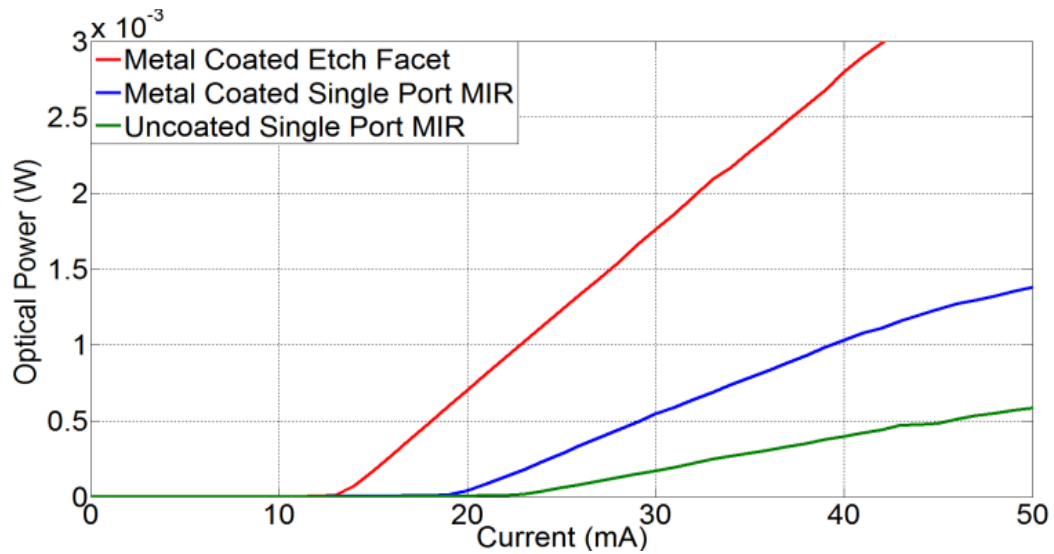


**Fig. 4.6:** Plot of coupled optical power versus applied current for various single port port reflector test structures

Figure 4.7a displays a schematic of an array of test structures designed to investigate the behaviour of the dual port MIR. These dual port MIRs were based on a 2x2 MMI coupler and were designed to act as 50:50 reflectors. Therefore, when light was coupled into port A, fifty percent of the reflected power should be transmitted through port B while the remainder should return to port A. The primary purpose of these structures was to confirm that the dual port MIR reflects sufficient light into both ports for lasing to occur. The MIRs were integrated with two waveguide outputs, which terminated with cleaved facets. The length of the structure was 410  $\mu\text{m}$  with a total cavity length from facet to facet of 820  $\mu\text{m}$ . All sections including the output waveguides had individual contact pads so that they could be biased separately. As with the one port MIRs, two variations of the dual port reflector were tested. One had metal coated reflective mirrors while for the others, the reflective mirrors were left bare. To compare the performance of the two dual port MIR designs, the current applied to Output 1 was swept from 0 mA to 50 mA while Output 2 was not biased. The MIR was biased to transparency to minimise absorption loss. As before, a short focus lensed fibre was positioned close to the edge of the device to record the optical power from Output 1. Figure 4.7b

demonstrates that the metal coated MIR performance is slightly better than the uncoated alternative, but both variations are viable options. As with the one port MIRs, it is believed that the reflection of the dual port structures is primarily being limited by losses associated with sidewall roughness. As the MIRs are based on total internal reflection instead of solely relying on high index contrast, coating the reflective surfaces with metal only slightly improved the performance of the device.

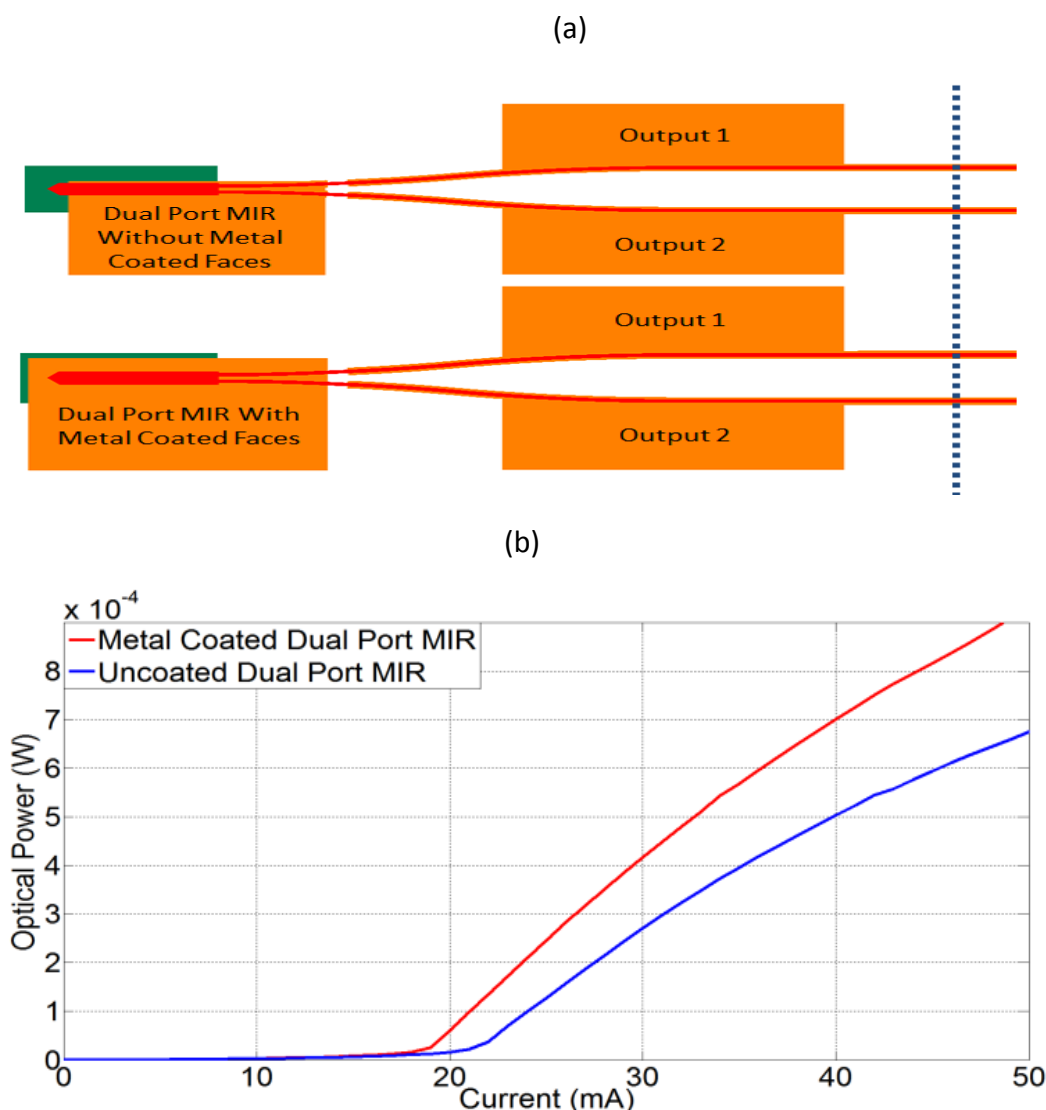


**Fig 4.7:** (a) Schematic and (b) light intensity plot of dual port reflectors.

Figure 4.8 displays the optical spectra observed from Output 1 via a lensed fiber. When both outputs were biased to 50 mA, double peaks appear in the spectrum. These double peaks indicate the presence of two cavities of slightly different length. Although both output waveguides were designed to be identical, the difference is

likely caused by a slight rotational misalignment between the lithography and the cleave plane which alters the effective optical path length of the arms. Secondly, when Output 1 is biased to 50 mA while Output 2 was left unbiased, a simple Fabry Perot spectrum is observed. These traces suggest that the dual port MIR has created

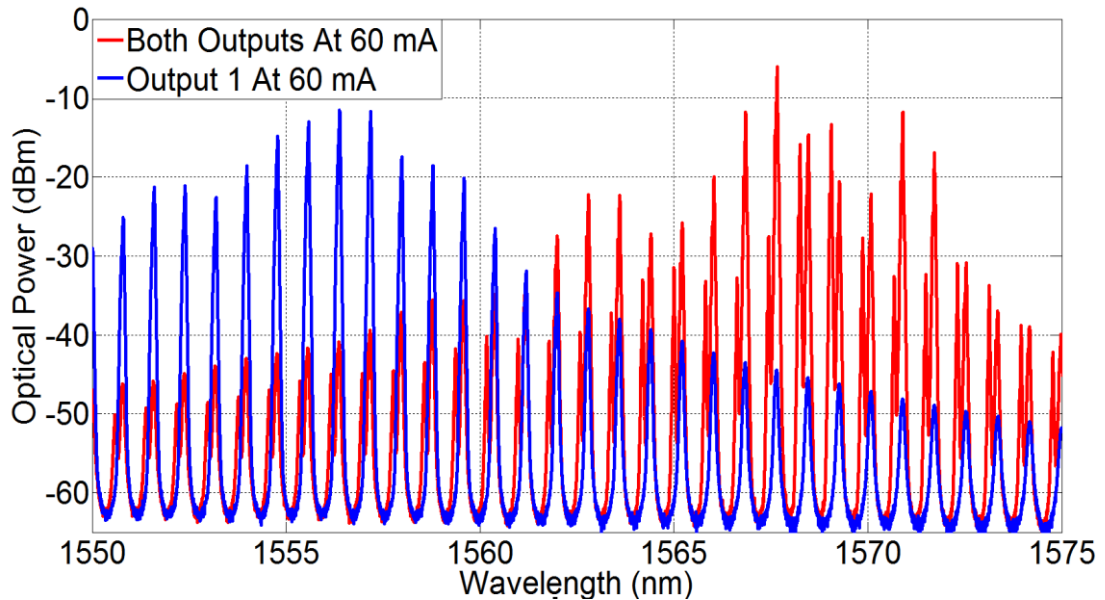


**Fig 4.8:** Optical spectra of dual port MIR test structure for various output waveguide bias conditions

two sub cavities. This behaviour was observed for both types of dual port MIR. The wavelength drift between the two measurements was a result of thermal heating due to the increased current. To further strengthen the conclusion that the dual port MIR is creating two sub cavities, Output 1 was biased to near threshold while Output 2 was left unbiased. The corresponding cavity lengths were extracted by taking the Fourier Transform of the spectral data from an OSA trace near threshold, similar to those in Figure 4.8 with the results presented in Figure 4.9. A peak is clearly visible at  $410 \mu\text{m}$ , corresponding to the distance from the cleaved facet to the end of the MIR. These results verify that the MIR is capable of providing sufficient feedback to an individual port for lasing to occur.

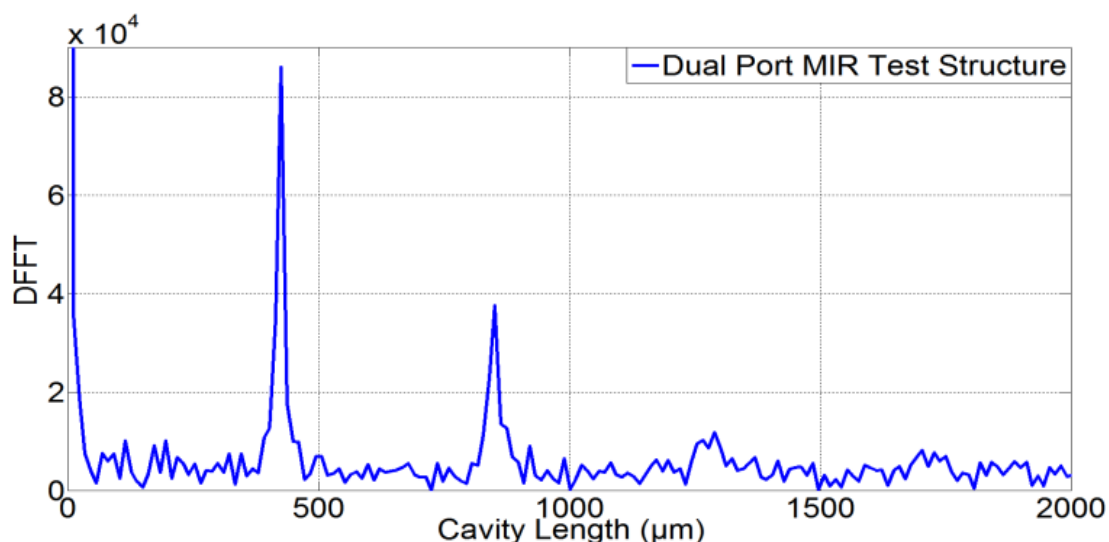


**Fig 4.9:** Fourier transform analysis dual port MIR optical spectrum near threshold.

#### 4.5 MIR Laser Test Devices

A schematic of MIR based test devices is shown in Figure 4.10. A 480  $\mu\text{m}$  long gain section is enclosed by a two port MIR and an etched facet. The etched facet directs all the reflected light back into the laser cavity while a dual port MIR divides the reflected light equally between the laser cavity and an output semiconductor optical amplifier section (SOA). Device 0 has a 90 degree facet and therefore should contain two discrete cavities. Device 1 has a 7-degree SOA section as an output and will need to rely exclusively on the reflections from the two MIRs to lase. Analysis of these two devices will confirm that the dual port MIR can be used to create a lasing cavity which does not rely on a cleaved facet.

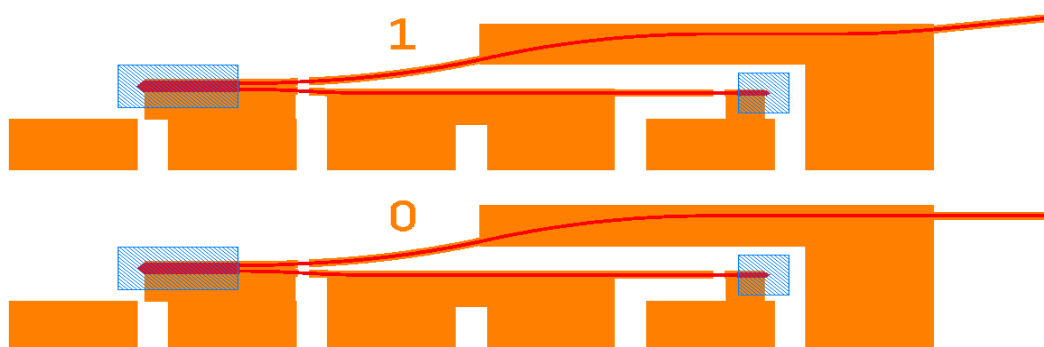


**Fig 4.10:** Single facet and facetless MIR based lasers

To compare the resonant cavities of these test lasers, their optical spectra near threshold was measured (Fig 4.11a). These OSA traces were converted into the wavelength domain plot presented in Figure 4.11b by taking their Fourier Transforms. The single facet laser produced a complicated plot with multiple peaks correspond to numerous resonant cavities. The peak  $A_0$  represents the 480  $\mu\text{m}$  spacing between the etched facet and the dual port MIR. Peak  $B_0$  corresponds the SOA output length with  $C_0$  equal to the sum of these two cavities and therefore indicates the total cavity length.

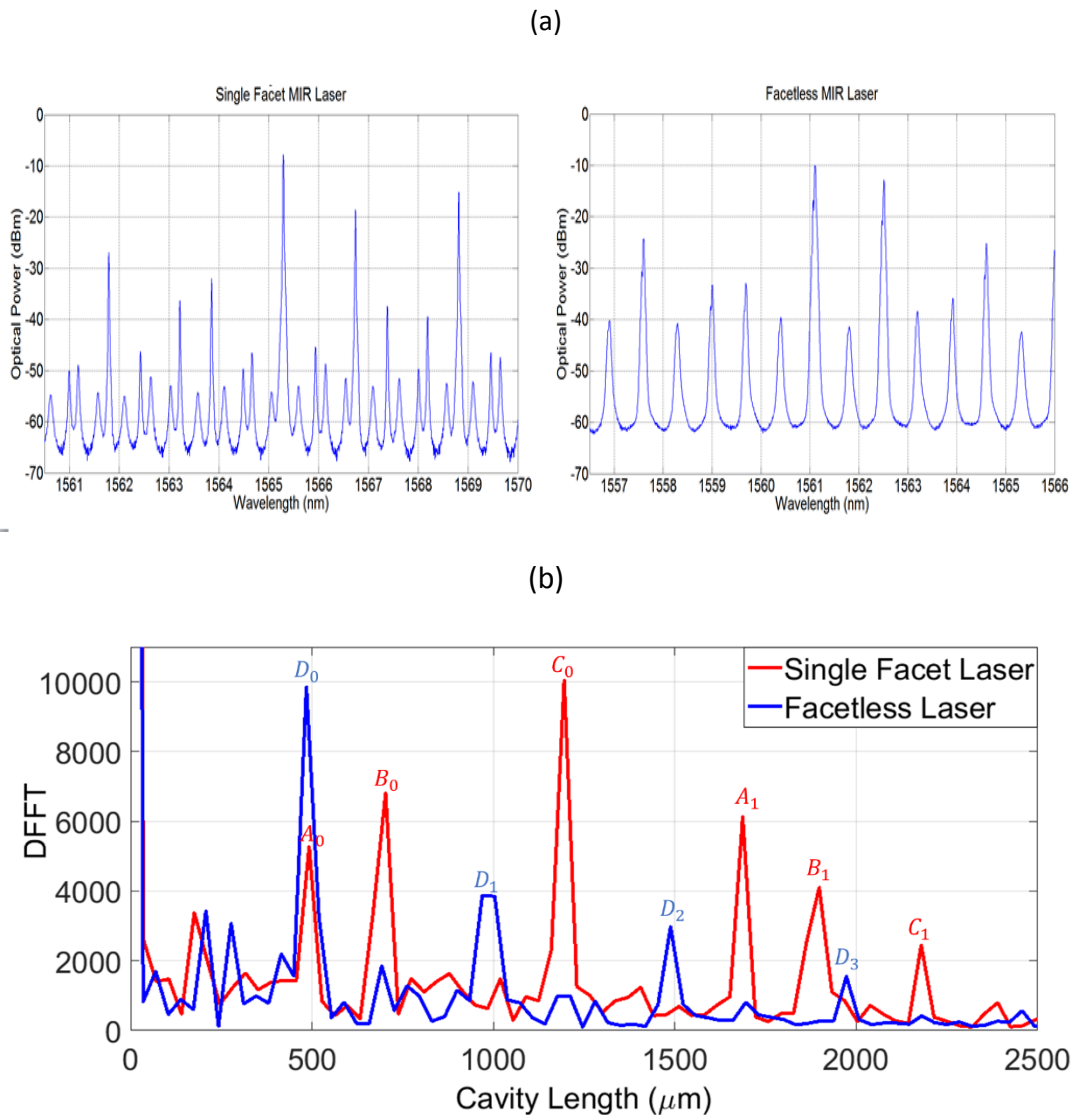


**Fig 4.11:** (a) Optical spectra near threshold and (b) Fourier Transform analysis of single facet and facetless MIR based lasers

As expected, this laser design is influenced by reflections from the cleaved facet. In contrast, the facetless laser plot contains a single peak at  $480 \mu\text{m}$  confirming that it is lasing without the assistance of reflections from the cleave. Repetitions of the cavity lengths are denoted by incremental subscripts i.e.  $A_1$  is equal to  $A_0$  plus the total cavity length  $C_0$ .

#### 4.6 MIR Facetless Laser

The MIR laser with the deep etched slot was selected for extensive testing as it exhibited the most favourable single mode behaviour. A schematic of the device demonstrated in this section is shown in Figure 4.12. A  $480 \mu\text{m}$  long gain section is enclosed by a dual port MIR and a metal coated etched facet. The etched facet forms a simple mirror which reflects light back into the laser cavity while a dual port MIR divides the reflected light equally between the laser cavity and an output waveguide. The  $650 \mu\text{m}$  long output waveguide then terminates in a 7 degree facet which allows light to be coupled off-chip while minimising reflections. The dimensions of the MIR were designed using the same methods as in [6],[13]. It has an overall length of  $80 \mu\text{m}$  and a width of  $11 \mu\text{m}$ . A single  $1 \mu\text{m}$  wide deep etched slot divides the laser cavity into two discrete sub cavities (Cavity 1= $400 \mu\text{m}$  and Cavity 2= $79 \mu\text{m}$ ), to utilise

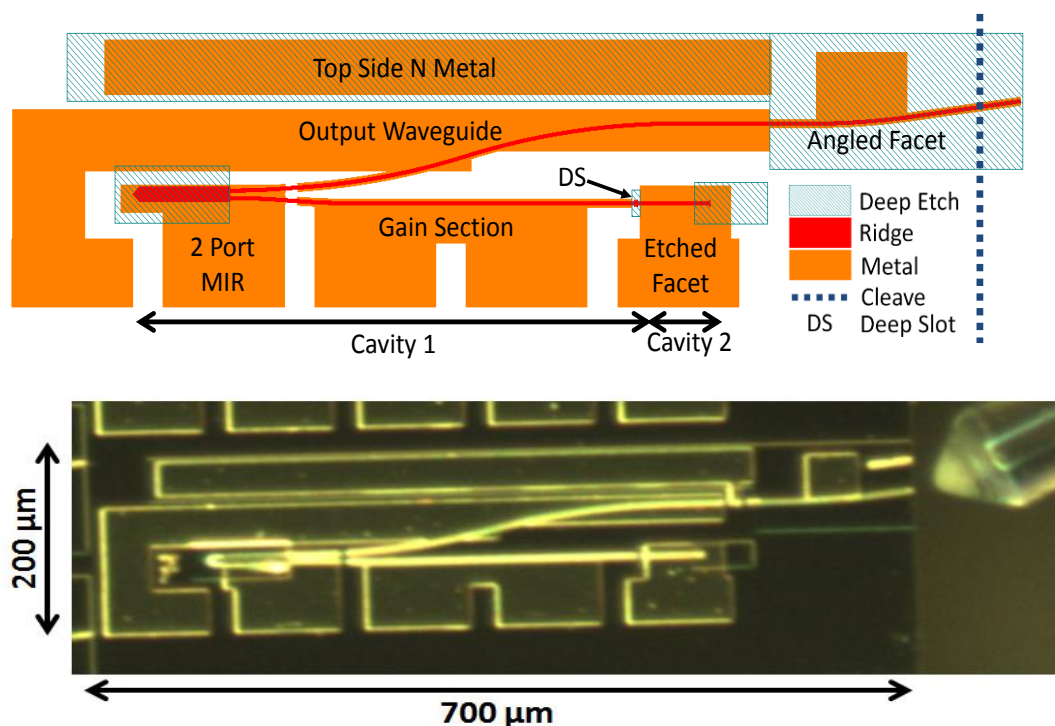


**Fig 4.12:** Schematic and microscopic image of MIR based facetless laser.



the coupled cavity effect [14]. Wavelengths which are resonant in a cavity are enhanced with non-resonant wavelengths being suppressed. Creating sub cavities can induce single mode operation as only resonant wavelengths common to both the main cavity and sub cavities will lase. The gain profile of a sub cavity can be altered by varying the bias across it, which in turn selects the resonant wavelengths. Therefore the lasing wavelength of the laser can be controlled using Vernier tuning [14]. This technique is commonly used in coupled cavity devices [13].

As this device was fabricated using a single epitaxial structure with no regrowth, all sections must be biased to transparency to minimise absorption losses. Different sections were designed to be powered separately to ensure that the current does not preferentially pass through the MIR sections, which have lower resistances due to their larger surface areas. The various sections were electrically separated using 10  $\mu\text{m}$  long breaks in the P metal and separate contact pads. These breaks do not provide full electrical isolation between sections. They do however separate them sufficiently to ensure that all sections receive adequate bias. They were favoured over shallow etched slots as they will not contribute to the perturbation of the optical modes present in the laser cavity. The contact pads were arranged with a 125  $\mu\text{m}$  pitch to be compatible with a multi contact probe to increase ease of testing. Scanning electron microscope images of the dual port MIR, the deep etched slot, and the etched facet are shown in Figure 4.13.

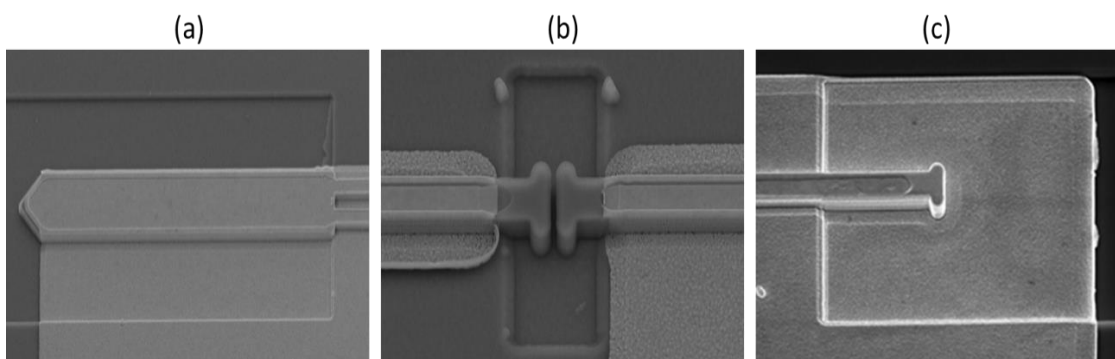


**Fig 4.13:** SEM image of the (a) dual port MIR (b) the deep etched slot which defines the two sub cavities creating a single mode output and (c) metal coated etched facet.

All sections of the device were independently forward biased using a multi-contact probe. The current in Cavity 1 was swept from 40 mA to 90 mA while Cavity 2's bias ranged from 20 mA to 45 mA and the results are seen in Figure 4.14. The output waveguide sections were lightly biased to minimise absorption losses. The threshold of Cavity 2 of the laser decreased from 35 mA to 21 mA with increasing bias to Cavity 1 from 40 mA to 70 mA. A tuning map indicating the peak wavelength for a given bias is shown in Figure 4.15. An optical spectrum analyser was used to analyse the optical spectrum of the laser output.

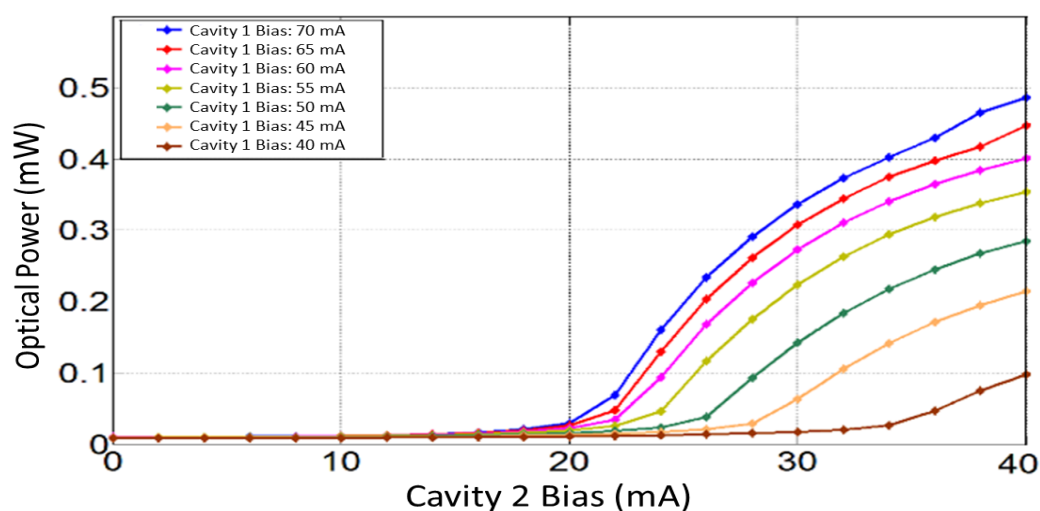


**Fig 4.14:** Fiber coupled output power as a function of cavity bias.

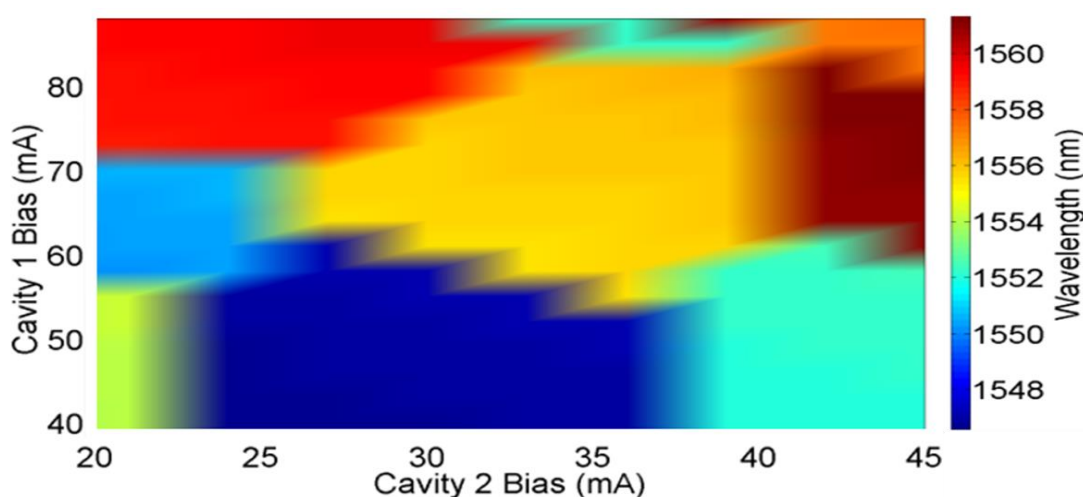


**Fig 4.15:** Contour plot demonstrating the peak wavelength of the laser for various bias conditions.

Single mode operation and mode selectivity was demonstrated by adjusting the bias ratio in the various sections. In Figure 4.16, the laser is tuned to five distinct wavelengths over a range of 15 nm by varying the bias of the two sub cavities. A side mode suppression ratio (SMSR) of 30 dB was achieved for all five bias conditions. The maximum measured optical power from the laser was <1 mW, however, we believe this is due to the limitations of the coupling efficiency with single mode fibre in our on-chip test setup. The fibre coupled output power could be improved by using a mode adapter or an optimised lensed fiber [15].

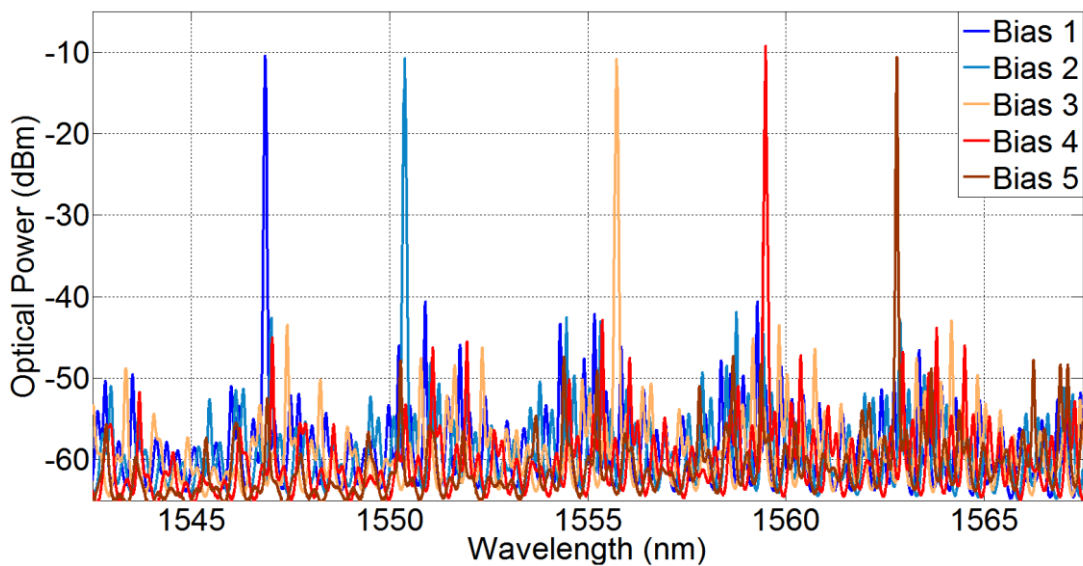


**Fig 4.16:** Single mode operation at five discrete wavelengths with an SMSR of 30dB.

The corresponding cavity lengths were extracted by taking the Fourier Transform of the spectral data from an OSA trace near threshold, similar to those in Figure 4.16, with the results presented in Figure 4.17. As expected, peaks can be seen at 79  $\mu\text{m}$  (A) and 400  $\mu\text{m}$  (B) which correspond to the lengths of Cavity 1 and Cavity 2, as well as a peak at 480  $\mu\text{m}$  (C) representing the total cavity length. This confirms that the laser does not rely on reflections from the cleaved facet as there are no peaks present which correspond to the length of the output waveguide. The free spectral range (FSR) of the laser was calculated to be 3.17 nm, which corresponds to the smaller sub cavity length (79  $\mu\text{m}$ ).

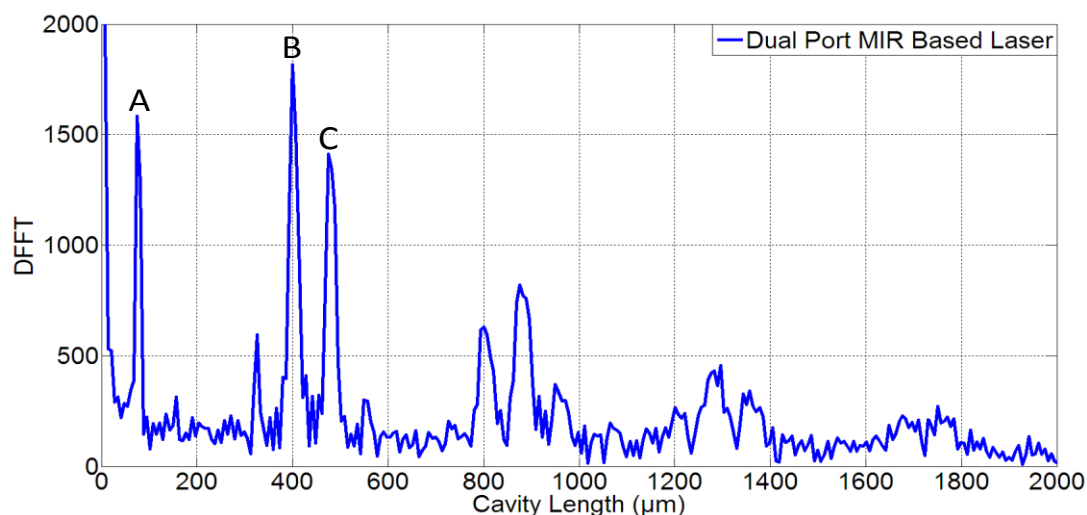


**Fig 4.17:** Fourier transform analysis of optical spectrum near threshold.

#### 4.7 Summary

This chapter has demonstrated that a dual port multimode interference reflector has been monolithically integrated with an etched facet and a gain section to create an InP based laser. The fabrication of these devices has been achieved without the use of advanced fabrication techniques such as epitaxial regrowth or E-beam lithography. A single deep etched slot produced single mode behavior due to the coupled cavity effect. Five distinct wavelengths over a range of 15 nm were achieved by varying the biases of the two sub cavities. An SMSR of 30 dB was observed for these tuning conditions. The next chapter will employ similar design and characterisation techniques to integrate the core components required for the WDM transmitter proposed in Chapter 2.

#### Bibliography

- [1] H. Soda, Y. Kotaki, H. Sudo, H. Ishikawa, S. Yamakoshi, and H. Imai, "Stability in single longitudinal mode operation in GaInAsP/InP phase-adjusted DFB lasers," *IEEE J. Quantum Electron.*, vol. 23, no. 6, pp. 804–814, Jun. 1987.
- [2] F. Koyama, Y. Suematsu, S. Arai, and T. Tawee, "1.5-1.6  $\mu\text{m}$  GaInAsP/InP dynamic-single-mode (DSM) lasers with distributed Bragg reflector," *IEEE J. Quantum Electron.*, vol. 19, no. 6, pp. 1042–1051, Jun. 1983.

- [3] D. Byrne, Q. Lu, W. H. Guo, J. F. Donegan, B. Corbett, B. Roycroft, P. Lambkin, J.-P. Engelstaedter, and F. Peters, "A facetless laser suitable for monolithic integration," in *OFC/NFOEC 2008 - 2008 Conference on Optical Fiber Communication/National Fiber Optic Engineers Conference*, 2008, pp. 1–3.
- [4] L. B. Soldano and E. C. M. Pennings, "Optical multi-mode interference devices based on self-imaging: principles and applications," *J. Light. Technol.*, vol. 13, no. 4, pp. 615–627, Apr. 1995.
- [5] K. Okamoto, *Fundamentals of optical waveguides*. Academic Press, 2005.
- [6] E. Kleijn, M. K. Smit, and X. J. M. Leijtens, "Multimode Interference Reflectors: A New Class of Components for Photonic Integrated Circuits," *J. Light. Technol.*, vol. 31, no. 18, pp. 3055–3063, Sep. 2013.
- [7] J. Zhao, E. Kleij, P. J. Williams, M. K. Smit, and X. J. M. Leijtens, "On-chip laser with multimode interference reflectors realized in a generic integration platform," in *Compound Semiconductor Week (CSW/IPRM), 2011 and 23rd International Conference on Indium Phosphide and Related Material*, 2011.
- [8] M. Smit, X. Leijtens, and E. Bente, "A generic foundry model for InP-based photonic ICs," in *Optical Fiber Communication Conference and Exposition (OFC/NFOEC), 2012 and the National Fiber Optic Engineers Conference*, 2012.
- [9] P. E. Morrissey, N. Kelly, M. Dernaika, L. Caro, H. Yang, and F. H. Peters, "Coupled Cavity Single-Mode Laser Based on Regrowth-Free Integrated MMI Reflectors," *IEEE Photonics Technol. Lett.*, vol. 28, no. 12, pp. 1313–1316, Jun. 2016.
- [10] R. Phelan, W.-H. Guo, Q. Lu, D. Byrne, B. Roycroft, P. Lambkin, B. Corbett, F. Smyth, L. P. Barry, B. Kelly, J. O’Gorman, and J. F. Donegan, "A Novel Two-Section Tunable Discrete Mode Fabry-Pérot Laser Exhibiting Nanosecond Wavelength Switching," *IEEE J. Quantum Electron.*, vol. 44, no. 4, pp. 331–337, Apr. 2008.
- [11] B. Roycroft, P. Lambkin, S. Riesner, B. Corbett, and J. F. Donegan, "Transition

- From Perturbed to Coupled-Cavity Behavior With Asymmetric Spectral Emission in Ridge Lasers Emitting at 1.55  $\mu\text{m}$ ," *IEEE Photonics Technol. Lett.*, vol. 19, no. 1, pp. 58–60, Jan. 2007.
- [12] Q. Y. Lu, W. H. Guo, R. Phelan, D. Byrne, J. F. Donegan, P. Lambkin, and B. Corbett, "Analysis of Slot Characteristics in Slotted Single-Mode Semiconductor Lasers Using the 2-D Scattering Matrix Method," *IEEE Photonics Technol. Lett.*, vol. 18, no. 24, pp. 2605–2607, Dec. 2006.
- [13] P. E. Morrissey, N. Kelly, M. Dernaika, L. Caro, H. Yang, and F. H. Peters, "Coupled Cavity Single-Mode Laser Based on Regrowth-Free Integrated MMI Reflectors," *IEEE Photonics Technol. Lett.*, vol. 28, no. 12, pp. 1313–1316, Jun. 2016.
- [14] S. W. C. Larry A. Coldren, *Diode Lasers and Photonic integrated Circuits*. Santa Barbara: Wiley-Interscience Publication, 1995.
- [15] Jeong Hwan Song, H. N. J. Fernando, B. Roycroft, B. Corbett, and F. H. Peters, "Practical Design of Lensed Fibers for Semiconductor Laser Packaging Using Laser Welding Technique," *J. Light. Technol.*, vol. 27, no. 11, pp. 1533–1539, Jun. 2009.

## Chapter 5

# Monolithic Regrowth-Free Coherent WDM PIC

### 5.1 Introduction

Monolithic photonic integrated circuits (PICs) based on InP have provided an effective solution to realise advance functions at a system level with compact size. As discussed in Chapter 2, such PICs have been demonstrated using various techniques such as epitaxial regrowth [2], hybrid/heterogeneous integration of InP and Silicon [3], and band gap engineering methods such as quantum well intermixing [4],[5] and selective area regrowth [6]. However, regrowth free monolithic integration offers reduced fabrication complexity and duration when compared with these methods [7].

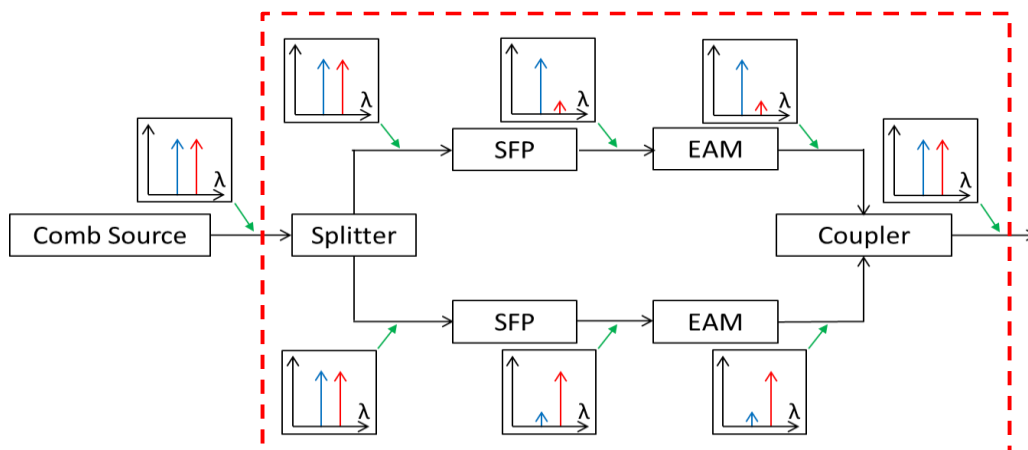


**Fig. 5.1:** Schematic of proposed regrowth free CoWDM transmitter based on SFP lasers and EAMs

In this chapter, the development of a monolithic PIC containing a 1x2 multimode interference coupler (MMI), two SFP lasers, two DC EAMs and a star coupler is discussed. The purpose of this device is to act as the core of the proposed CoWDM transmitter and its contribution is represented by the red square in Figure 5.1, which was discussed in Chapter 2, and reproduced from Figure 2.10. All devices in this chapter were fabricated using the DC fabrication process outlined in Chapter 3 and were characterised at a temperature of 25 C unless otherwise stated.

## 5.2 First Generation PIC

A schematic of the first-generation PIC is shown in Figure 5.2. A 1x2 MMI with a width and length of  $10\ \mu\text{m}$  and  $116\ \mu\text{m}$  respectively splits the injected light into two coherent outputs [8]. These MMI outputs in turn feed into two slotted SFP lasers via shallow etched curved waveguides with a bend radius of  $650\ \mu\text{m}$ . Each SFP laser consists of a  $650\ \mu\text{m}$  long gain section, which is enclosed by two mirror sections to create a facetless lasing cavity [9]. The mirror sections are comprised of 7 shallow etched slots with a gap of  $0.88\ \mu\text{m}$  and a separation of  $108\ \mu\text{m}$ . Wavelengths which are resonant with these subsections are enhanced with other non-resonant wavelengths being suppressed, providing optical feedback to the laser cavity while inducing single mode operation through the Vernier effect. Following the lasers in the PIC, there are  $300\ \mu\text{m}$  long semiconductor optical amplifiers (SOAs) and  $100\ \mu\text{m}$  long EAM sections. The SOA sections were included to act as a buffer preventing the EAMs from detuning their adjacent lasers when reversed biased. A 2x1 star coupler is arranged at the output of the PIC by converging waveguides from the EAMs to a Rowland circle, with the input waveguides directed towards the central output waveguide. Light from the input waveguides propagates in the free-space region between the waveguides where it can couple to the output waveguide [10]. The PIC's input and output waveguides are designed to create a seven-degree angle with the cleaved facets to minimise reflections which in turn will reduce the optical crosstalk between the lasers.

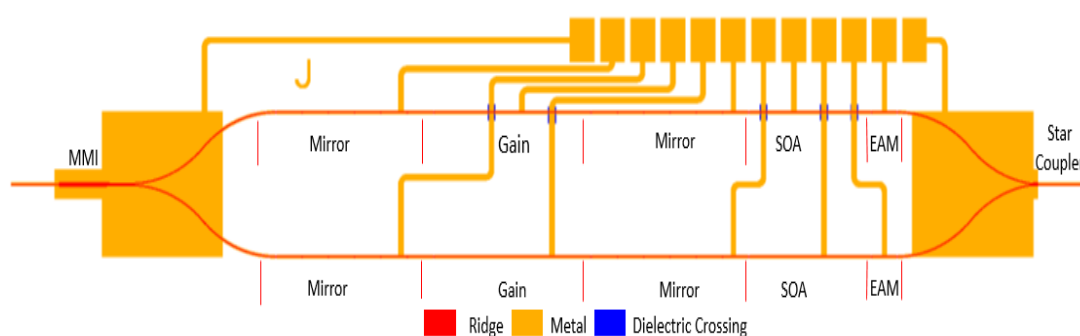


**Fig. 5.2:** Schematic of first generation PIC.



Due to the high number of sections, a noteworthy feature of this PIC is the ability to run metal traces over optical waveguides without contacting them. As this first generation PIC predates the DC fabrication process outlined in Chapter 3, an extra lithographic set was added to pattern an additional composite dielectric layer, creating metal crossings shown in Figure 5.3.  $\text{SiN}_x$  was used as the base layer for the crossings as it can be selectively patterned without damaging the dielectric present for sidewall passivation. An  $\text{SiO}_2$  layer was added to improve thermal and electrical isolation between the metal trace and the underlying waveguide/device as it has a preferable thermal conductivity and resistivity when compared to  $\text{SiN}_x$ . These traces connected to a series of standardised pads with a  $125\ \mu\text{m}$  pitch to be compatible with a multi contact probe to increase ease of testing.

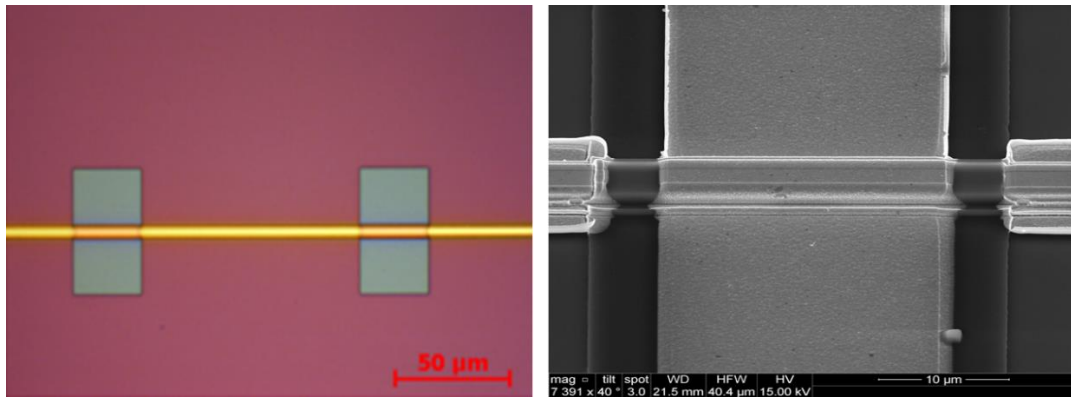


**Fig 5.3:** Microscopic and SEM images of dielectric metal trace crossings.

As the performance of the facetless lasers is critical for the correct operation of this PIC, an array of test structures was also included in the mask design (Figure 5.4). These test arrays consisted of SOA sections that surrounded lasers which were identical to those used in the main PIC. Reverse biasing the SOA sections would confirm that these lasers do not rely on reflections from the cleaved facet to lase. They were also used to monitor any variance in performance across multiple fabrication runs.

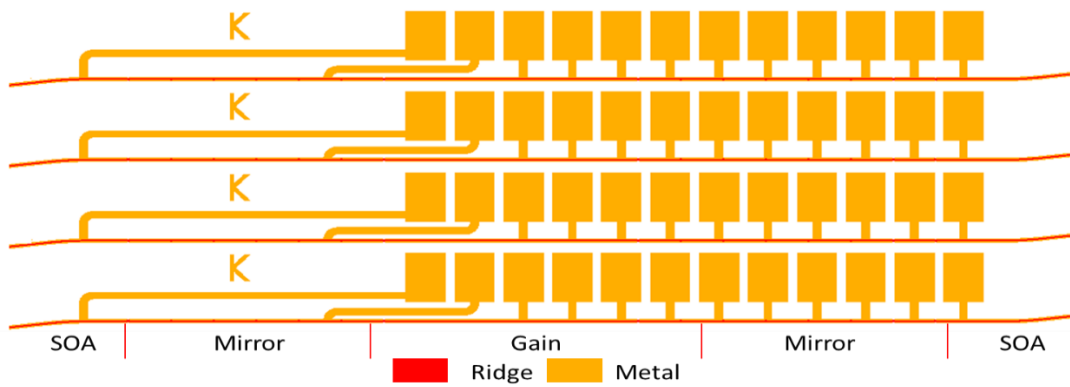
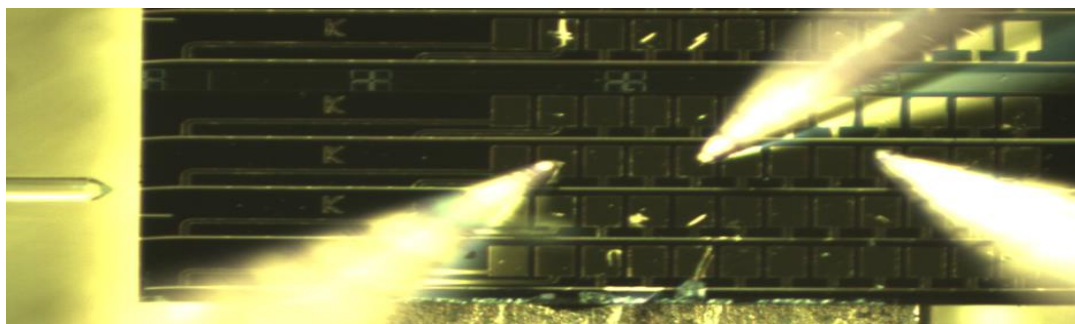
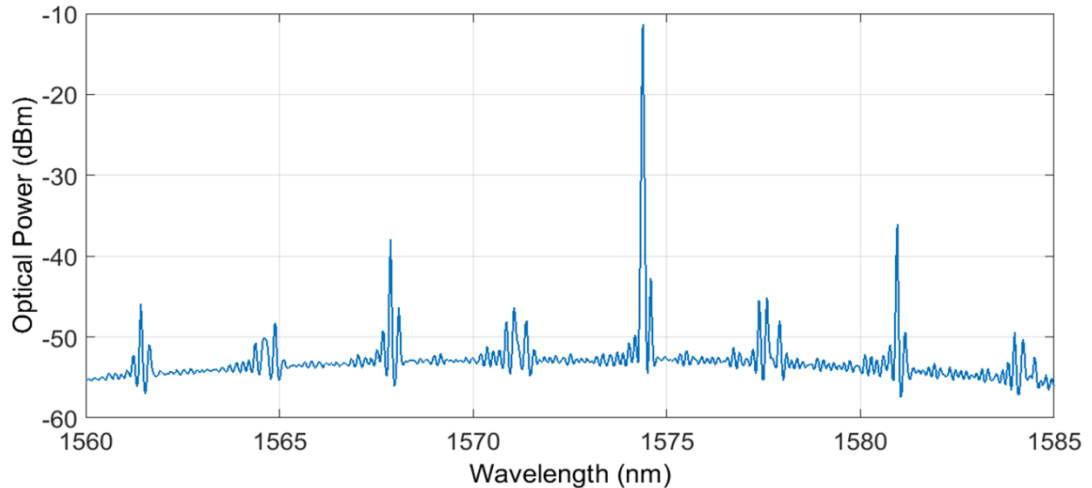


**Fig 5.4:** Schematic of facetless laser test arrays.

Figure 5.5a displays the fabricated facetless laser array under test. Each section of the laser independently received 50 mA and short focus lensed fibre was positioned close to the output of the device to enable coupling to the facet. An optical spectrum analyser (OSA) was used to analyse the power and optical spectrum of the laser output. The left SOA section was lightly biased to minimise absorption losses. Figure 5.5b shows the optical spectra of the laser with a peak power of -11.23 dBm into the fibre. The slotted mirror sections are clearly suppressing a large quantity of the Fabry-Perot modes and the output power of the laser remained unaffected as the right SOA section was reverse biased to -2 V, confirming that the laser was indeed facetless.



(a)

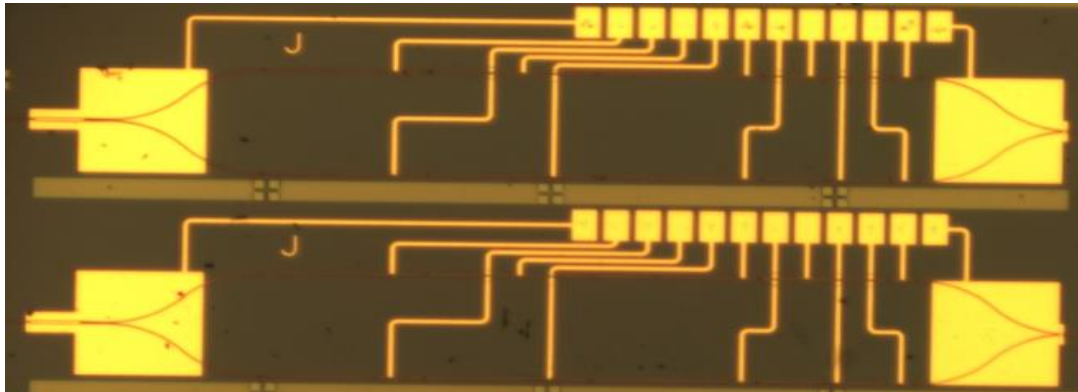


(b)

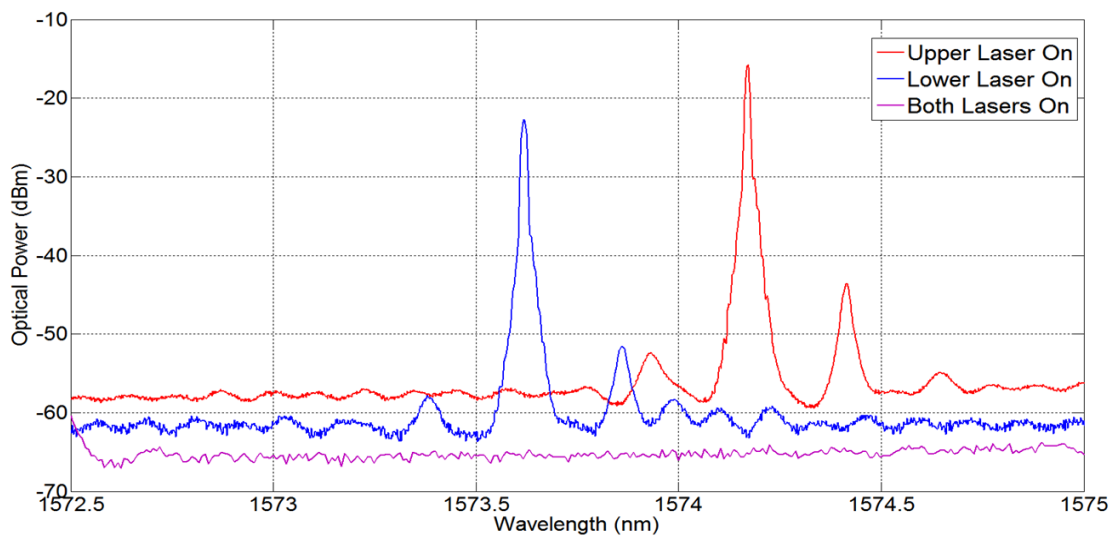
**Fig 5.5:** (a) Microscopic image and (b) optical spectrum from test arrays.

Figure 5.6 shows three different testing conditions for the first generation PIC. In the first condition, the top laser's mirror and gain sections are biased at 50 mA each while the bottom laser remained unpowered. Light was coupled through the MMI and bend sections, which were lightly biased to compensate for absorption. The optical spectra demonstrated a peak power of -16.04 dBm and a side mode suppression ratio (SMSR) greater than 25 dB. Secondly, the biasing condition was reversed so that the bottom laser now received power to all sections and the top laser was off. The bottom laser displayed a similar optical spectrum with a lower power output of -23.42 dBm. An issue arose, however, when both lasers were powered simultaneously as shown in the third plot. The output power of both lasers completely dissipated with a recorded output power of -60.26 dBm. This power drop was attributed to overheating of the chip. A series of transmission line measurement (TLM) structures showed that the P metal semiconductor interface had a high specific contact resistance of  $3.2 \times 10^{-4} \Omega \text{cm}^2$  resulting in additional ohmic heating as well as increasing the thermal crosstalk between the lasers. This was likely a result of the InGaAs cap layer becoming damaged during the ridge etch or the hard mask removal.

(a)



(b)



**Fig 5.6:** (a) Microscope image and (b) optical spectra demonstrating crosstalk between lasers.

This thermal crosstalk issue is further demonstrated in Figure 5.7 where the output of the top laser was recorded as various sections of the bottom laser were powered. An incremental decrease of the top laser's optical output was measured as other sections were systematically forward biased. Electrical crosstalk was ruled out as a possible contributor as all sections showed an electrical isolation greater than 100 k $\Omega$ , including traces isolated by the dielectric crossings.

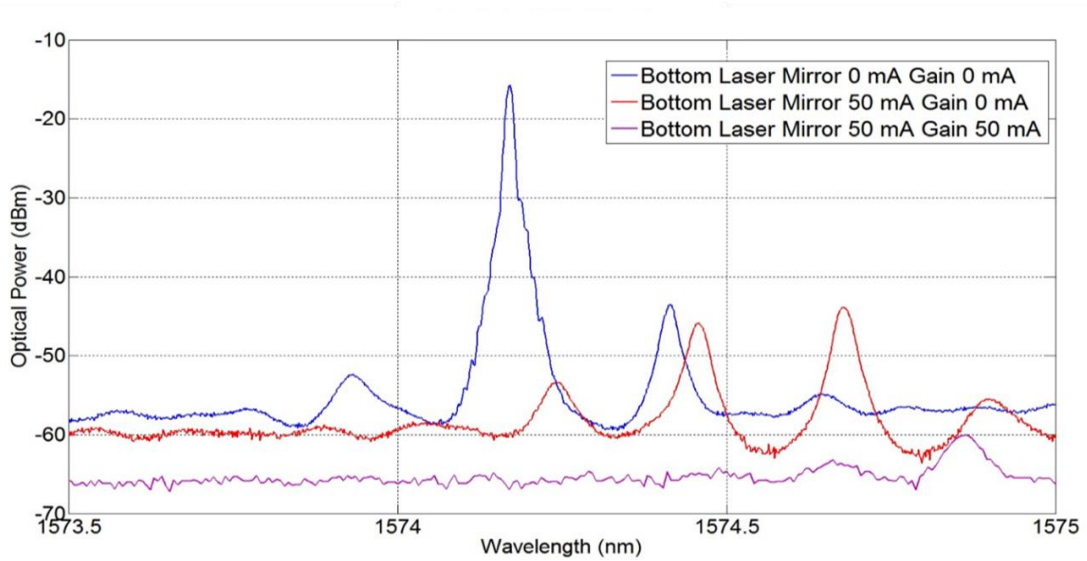


**Fig 5.7:** Optical spectra demonstrating crosstalk between lasers.

This thermal crosstalk issue was successfully managed on a single BPSK device by setting the temperature controller to 11 C (below the dew point of the testing lab). When the lasers were biased just above threshold, it was possible to get both lasers operating simultaneously as shown in Figure 5.8. This experiment confirmed that such a PIC was possible provided thermal heating was minimised.

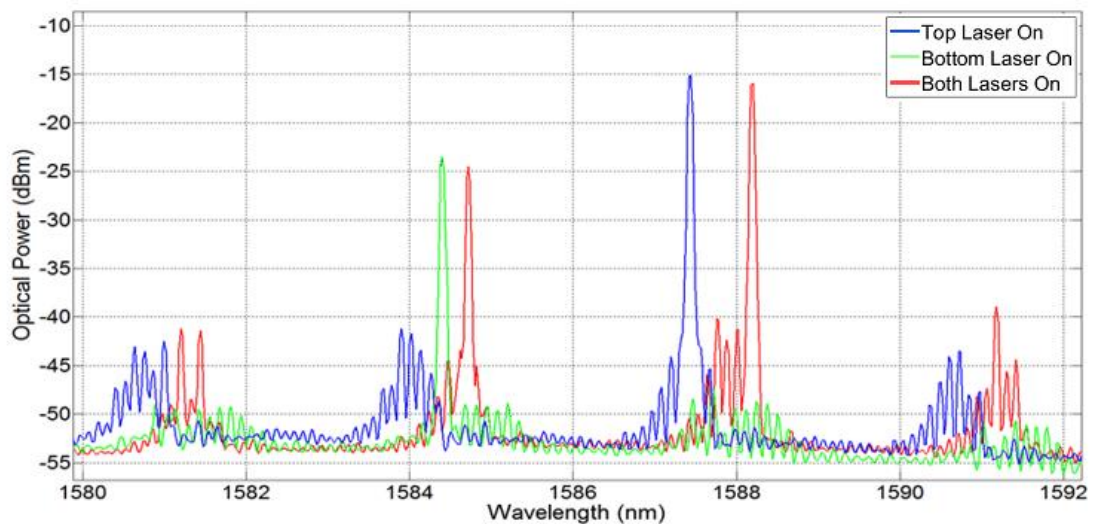


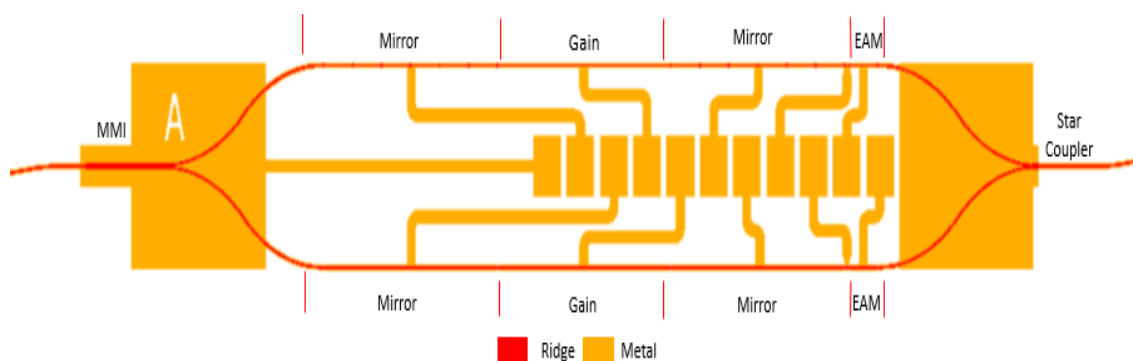
**Fig 5.8:** Optical spectra demonstrating crosstalk between lasers.

Advanced testing of this device proved impossible, however, due to overheating of the chip when additional sections such as the SOAs, output waveguides and star coupler were biased. It was these difficulties resulting from a high specific contact

resistance of the P metal semiconductor interface which prompted the implementation of the standardised DC fabrication process outlined in Chapter 3 and the design of a second generation PIC.

### 5.3 Second Generation PIC

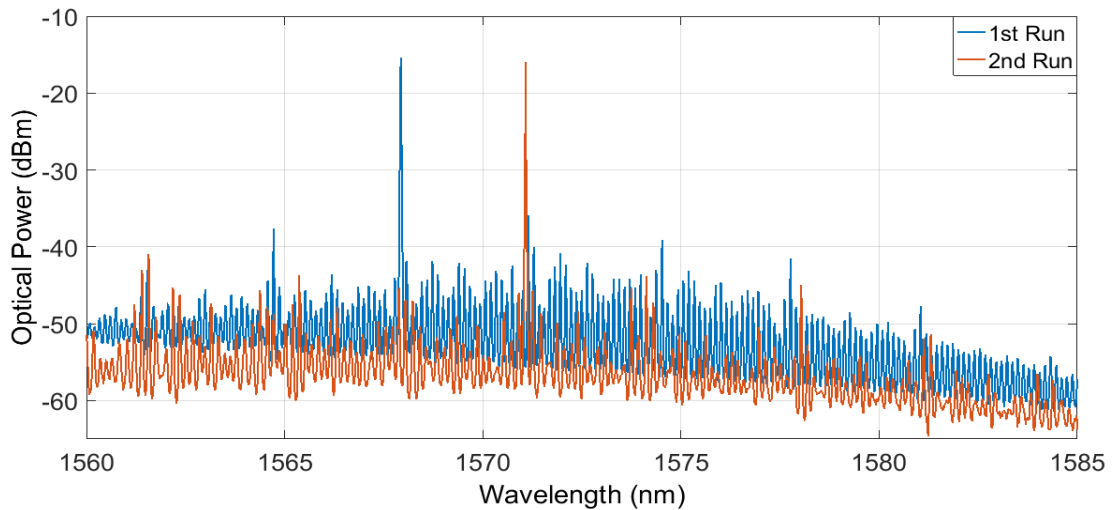
A schematic of the second generation PIC is shown in Figure 5.9. Since the dielectric crossings from the previous design were incompatible with the standardised DC process, the metal traces and contact pads were rearranged to facilitate the use of a multi-contact probe. As the isolation slots on the previous PIC provided greater than 100 k $\Omega$  resistance, the SOA sections which served as buffers between the lasers and EAMs were removed. This had the advantage of eliminating two contacts and reducing the power requirement of the PIC. The design of key components such as the MMI, lasers and star coupler were unchanged.



**Fig. 5.9:** Schematic of second generation PIC.

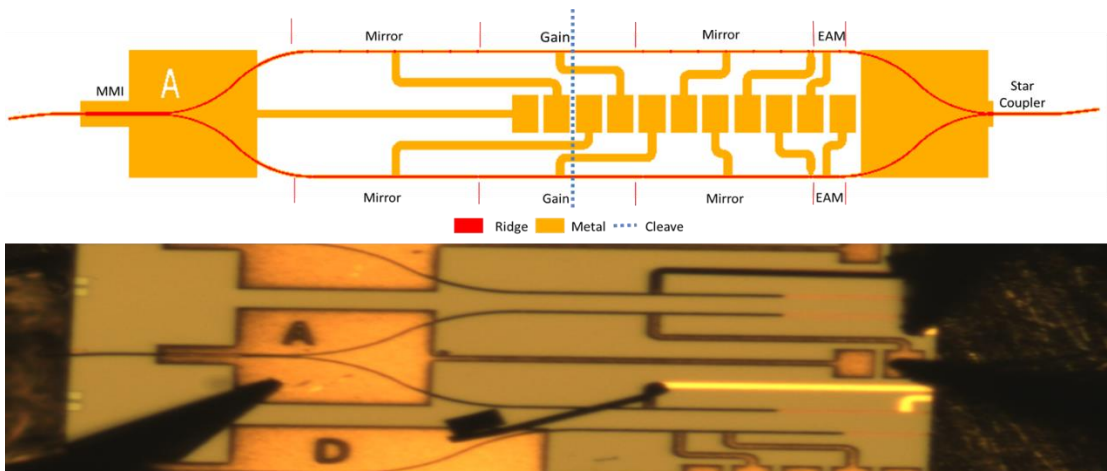
TLM measurements of the second generation fabrication run yielded a specific contact resistance of  $2.7 \times 10^{-6} \Omega \text{cm}^2$  which was two orders of magnitude better than the previous attempt. However, characterisation of the test arrays indicated that the lasers were relying on the output facets to lase. The fibre coupled optical power dropped from approximately -15 dBm to below -50 dBm when the output waveguides and star coupler were reversed biased at -2V. The under performance of the lasers was likely due to variation in the etch depth of the slot. In an attempt to rectify this issue, a second run of devices was fabricated, yielding near identical results. Figure 5.10 shows the test laser optical spectra from the two runs when both SOA sections were biased to transparency. It is clear that the mirror sections are not

providing sufficient reflection to fully suppress the Fabry-Perot modes, particularly when compared with the optical spectrum presented in Figure 5.5. Characterisation of the main PICs proved unsuccessful as only spontaneous emission was detected from the output facets suggesting that the integrated lasers could not lase without the aid of reflections from cleaved facets.



**Fig. 5.10:** Optical spectra of second generation SFP lasers.

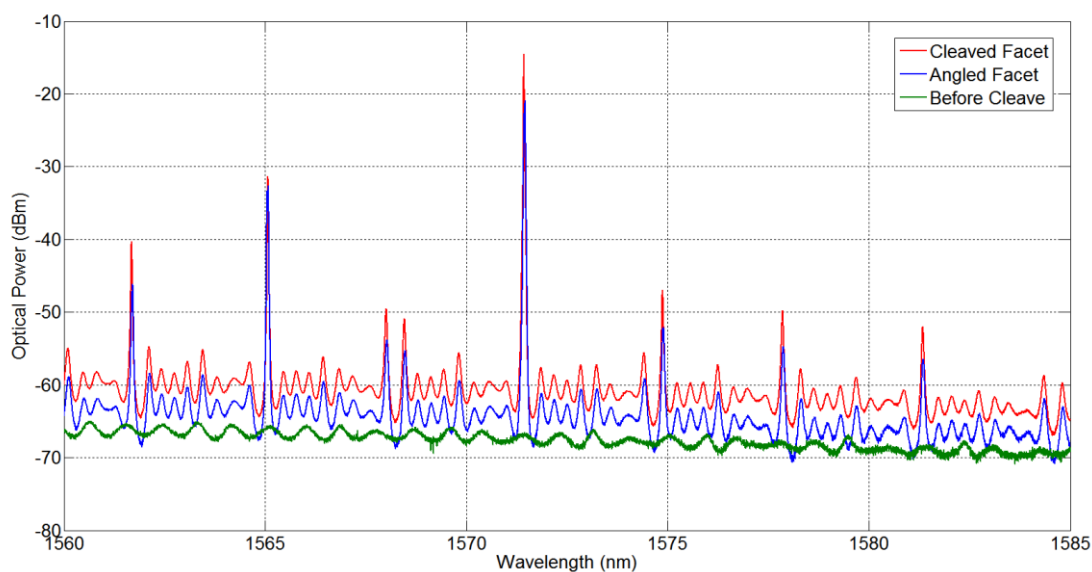
To verify that the slots were not providing sufficient optical reflection, one of the PICs was destructively cleaved in such a way that the lasers were split through the gain sections. This removed a set of mirror sections, the EAMs and the star coupler from the device, effectively creating two single facet lasers. A graphical explanation of this cleaving can be seen in Figure 5.11.



**Fig. 5.11:** Schematic of second generation PIC.



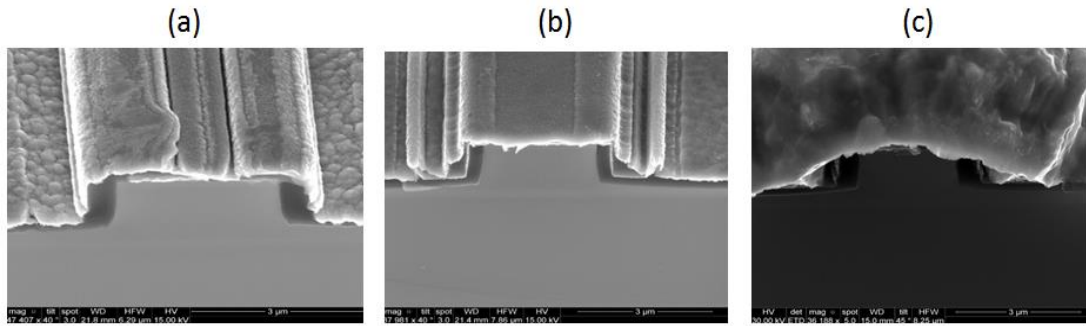
The lasers, MMI and bend sections were biased with the same current as in Figure 5.8. Lensed fibres were simultaneously aligned to the cleaved facet of one of the lasers and to the angled facet from the MMI. Figure 5.12 shows the output spectra from the PIC before and after cleaving. As discussed previously, only spontaneous emission was observed from the device before cleaving. After cleaving, a peak power of -14.6 dBm was measured from the laser's cleaved facet with a similar spectrum visible from the angled output. This confirms that the bend sections and MMI are operating correctly and are not responsible for the uncleaved chips malfunctioning.



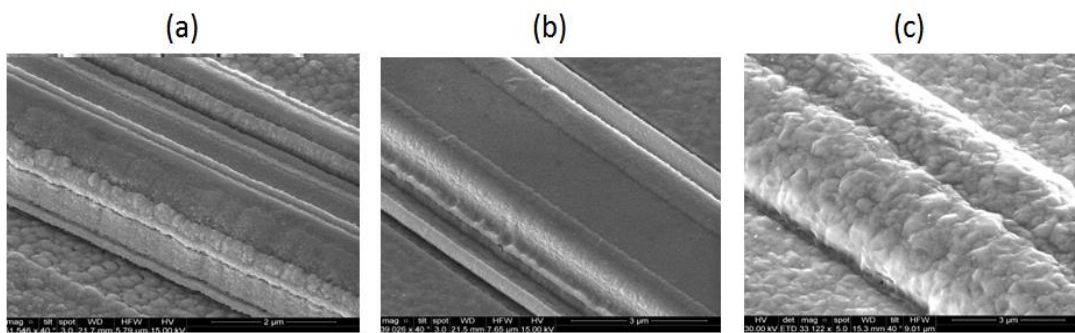
**Fig. 5.12:** Schematic of second generation PIC.

A series of SEM images were taken to determine why there is such a variation in the performance of the slotted lasers. A comparison was made for etch depth, ridge profiles, slot formation etc. but no significant difference was evident. It was concluded that although it is possible to create the current facetless slotted laser designs, they are highly sensitive to fabrication tolerances making them very difficult to reproduce.

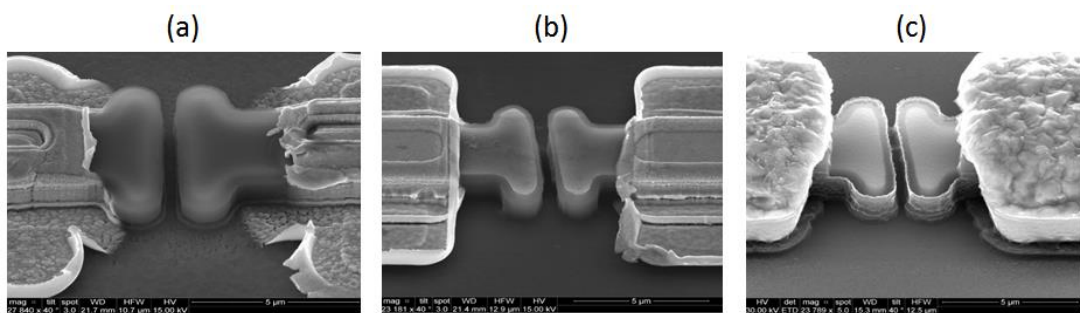




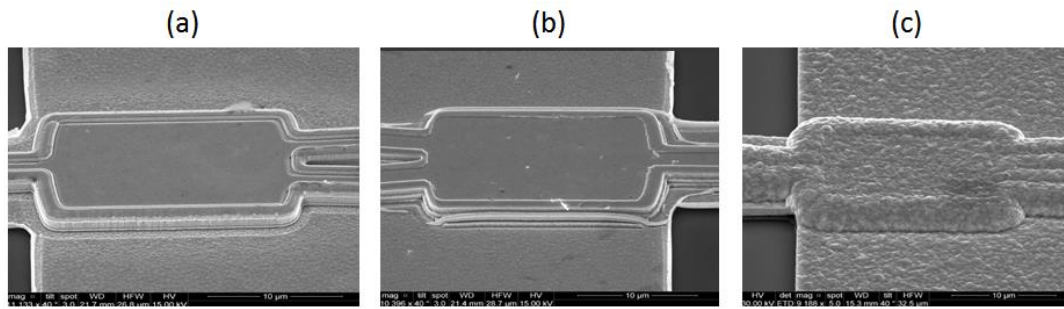
**Fig 5.13:** SEM images of waveguide facets on (a) 1<sup>st</sup> Generation (b) 2<sup>nd</sup> Generation Run 1 (c) 2<sup>nd</sup> Generation Run 2 PICs.



**Fig 5.14:** SEM images of waveguides on (a) 1<sup>st</sup> Generation (b) 2<sup>nd</sup> Generation Run 1 (c) 2<sup>nd</sup> Generation Run 2 PICs.



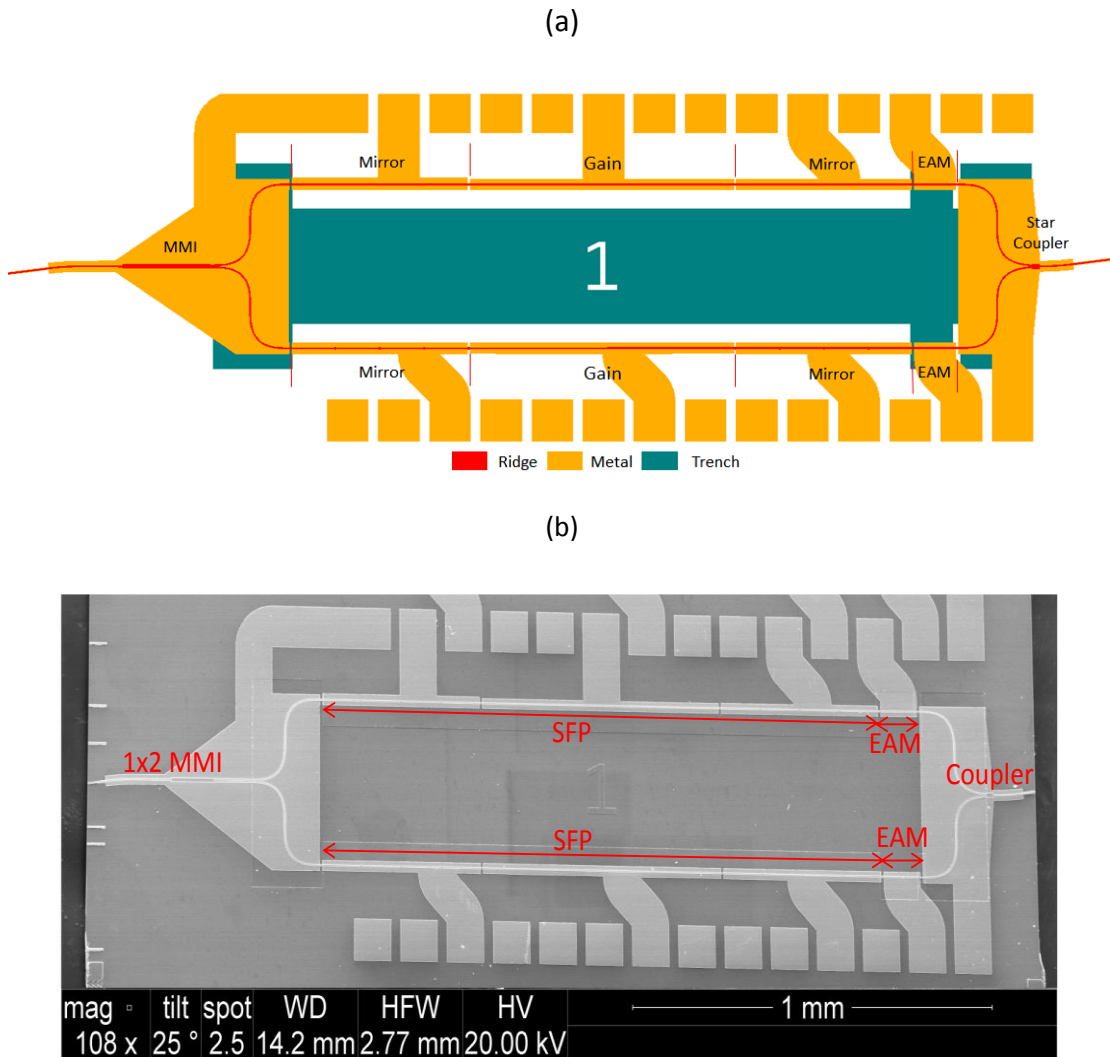
**Fig 5.15:** SEM images of shallow slots (a) 1<sup>st</sup> Generation (b) 2<sup>nd</sup> Generation Run 1 (c) 2<sup>nd</sup> Generation Run 2 PICs.



**Fig 5.16:** SEM images of star coupler on (a) 1<sup>st</sup> Generation (b) 2<sup>nd</sup> Generation Run 1 (c) 2<sup>nd</sup> Generation Run 2 PICs.

#### 5.4 Third Generation PIC Design

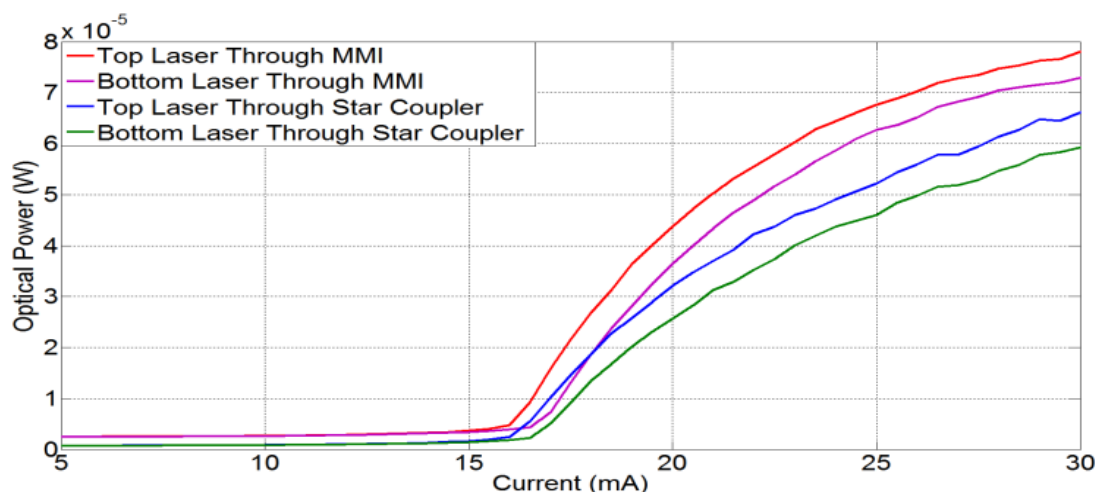
A key aspect of this generation of PIC was the redesign of the facetless lasers to improve their reliability. The new SFP lasers consisted of a 600  $\mu\text{m}$  long gain section which was enclosed by two mirror sections to create a lasing cavity. The mirrors were composed of 425  $\mu\text{m}$  sections of waveguide with five uniformly separated slots. The outermost slot of each mirror section was deep etched to provide significant reflection while the remaining slots were shallow etched to define 108  $\mu\text{m}$  sub-cavities in the laser cavity. The curved waveguide sections were deep etched to enable a smaller bend radius of 75  $\mu\text{m}$  due to increased optical confinement. Following the lasers were two 100  $\mu\text{m}$  long EAM sections. These EAM sections were also deep etched to maximise their extinction ratio through increased optical confinement. A deep etched trench (2.4  $\mu\text{m}$  deep) ran through the centre to the PIC to increase the thermal isolation between the two arms. As before, the PIC's input and output waveguides were designed to create a seven degree angle with the cleaved facets to minimise reflection, which in turn reduces the optical crosstalk between the lasers. Finally, the contact pads were arranged with a 125  $\mu\text{m}$  pitch to be compatible with a multi contact probe to increase ease of testing.



**Fig. 5.17:** (a) Schematic and (b) SEM image of 3<sup>rd</sup> generation PIC.

The first steps taken to characterise this device were to verify that the lasers and splitters/couplers were functioning as expected. To achieve this, all sections of the device were independently forward biased using multi-contact probes. The optical output of the device was coupled from the angled facets into an optical spectrum analyzer using lensed fiber. The mirror sections of the laser under test were each set to 30 mA while the current applied to the gain section was swept from 0 to 30 mA and the output power was recorded. All other sections were lightly biased to minimise absorption losses. Figure 5.18 shows the optical output power of each of the lasers through the MMI and star coupler respectively, verifying their correct operation. The maximum measured optical power from the lasers was <1mW, however, we believe this is due to the limitations of the coupling efficiency with

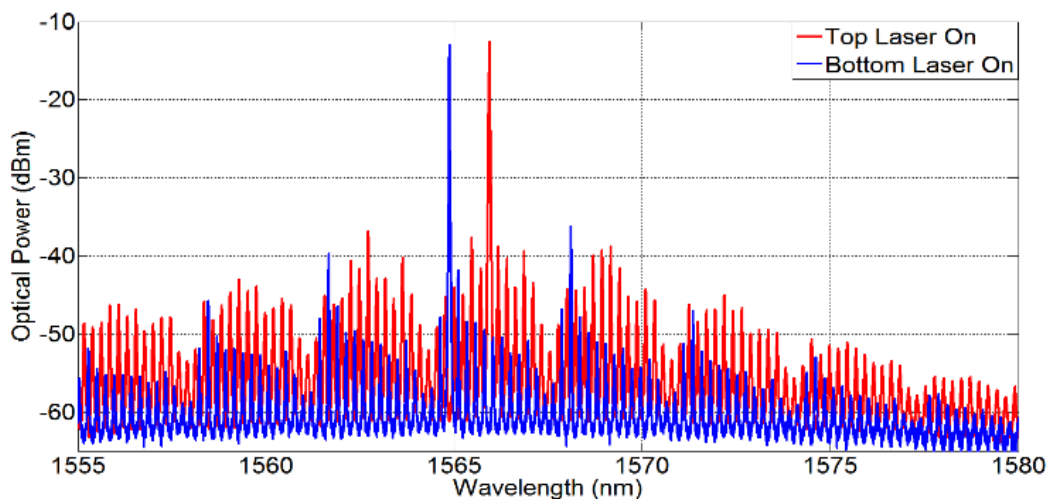
single mode fibre in the on-chip test setup. The fibre coupled output power could be further improved by using a mode adapter or an optimized lensed fibre. Minor differences in the recorded output powers are likely due to small defects which formed during the fabrication process.



**Fig. 5.18:** Fibre coupled power vs. gain section current.

Figure 5.19a displays the observed optical spectra from each of the lasers near threshold with the other laser off. Encouragingly, the optical spectrum in Figure 5.19b, which was taken when both lasers were powered simultaneously is identical to the superimposed traces in the previous graph. This demonstrates that there is not significant optical or thermal crosstalk between the lasers which is vital for correct operation as part of a CoWDM transmitter.

(a)



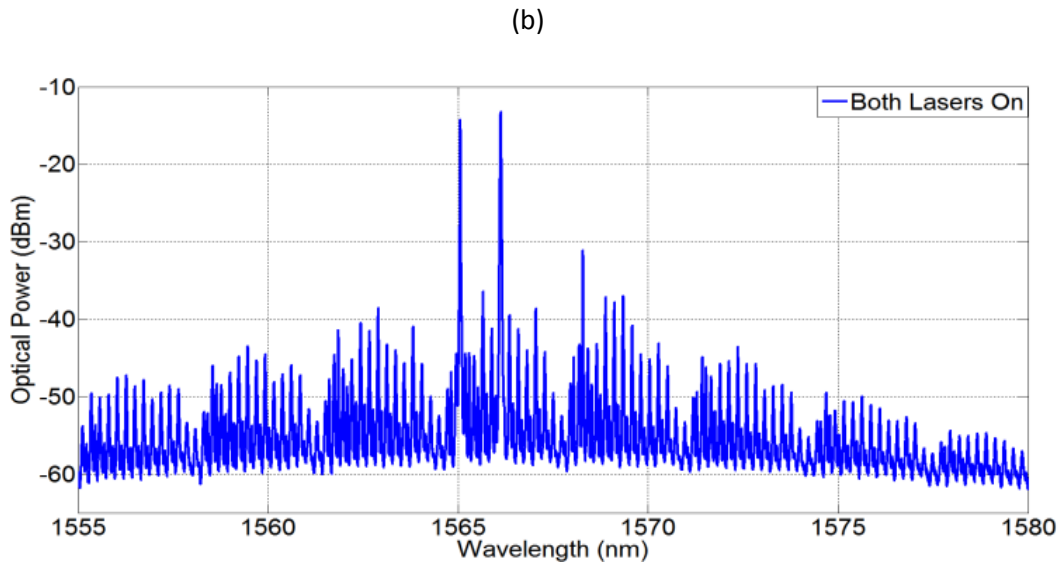


**Fig. 5.19:** (a) Optical spectra of both SFP lasers powered asynchronously. (b) Optical spectrum of SFP laser powered simultaneously.

The corresponding cavity lengths were extracted by taking the Fourier Transform of the spectral data from an OSA trace near threshold, similar to those in Figure 5.19a with the results presented in Figure 5.20. A large peak is clearly visible at  $1500\ \mu\text{m}$  (A), corresponding to the length of the gain and mirror section of the laser. Peaks representing the sub cavities created by the mirrors' slot are also visible (B). This confirms that the lasers do not rely on reflections from the cleaved facet as there are no peaks present which correspond to the length of the output waveguide. The free spectral range (FSR) of the laser was calculated to be  $3.18\ \text{nm}$ , which corresponds to the smaller sub cavity length ( $106\ \mu\text{m}$ ).

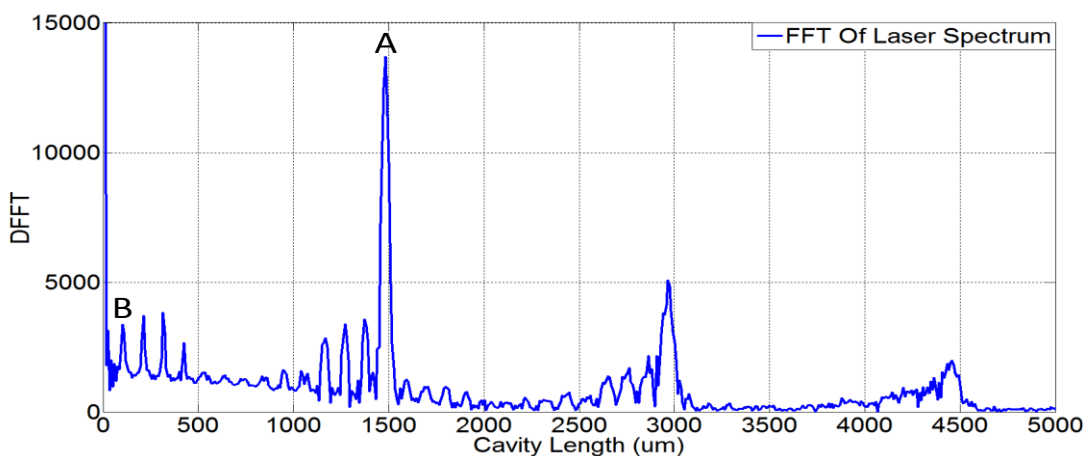


**Fig. 5.20:** Fourier transform analysis of laser optical spectrum near threshold.

For this PIC to act as the core component of a monolithic CoWDM transmitter, it is vital that the SFP lasers can be integrated with the EAMs to produce a modulated signal. To achieve this, the lasers must be tuned to longer wavelengths to take advantage of the quantum confined stark effect [12]. A high side mode suppression ratio (SMSR) is also required in CoWDM system to minimise crosstalk between the channels. A tuning map of one of the SFP lasers is shown in Figure 5.21a for a constant gain section bias of 30 mA. This plot shows that a wavelength tuning of approximately 10 nm can be achieved by varying the mirror section biases. Figure 5.21b displays the corresponding SMSR for the sweep, indicating two regions with suitably high suppression of the side modes.

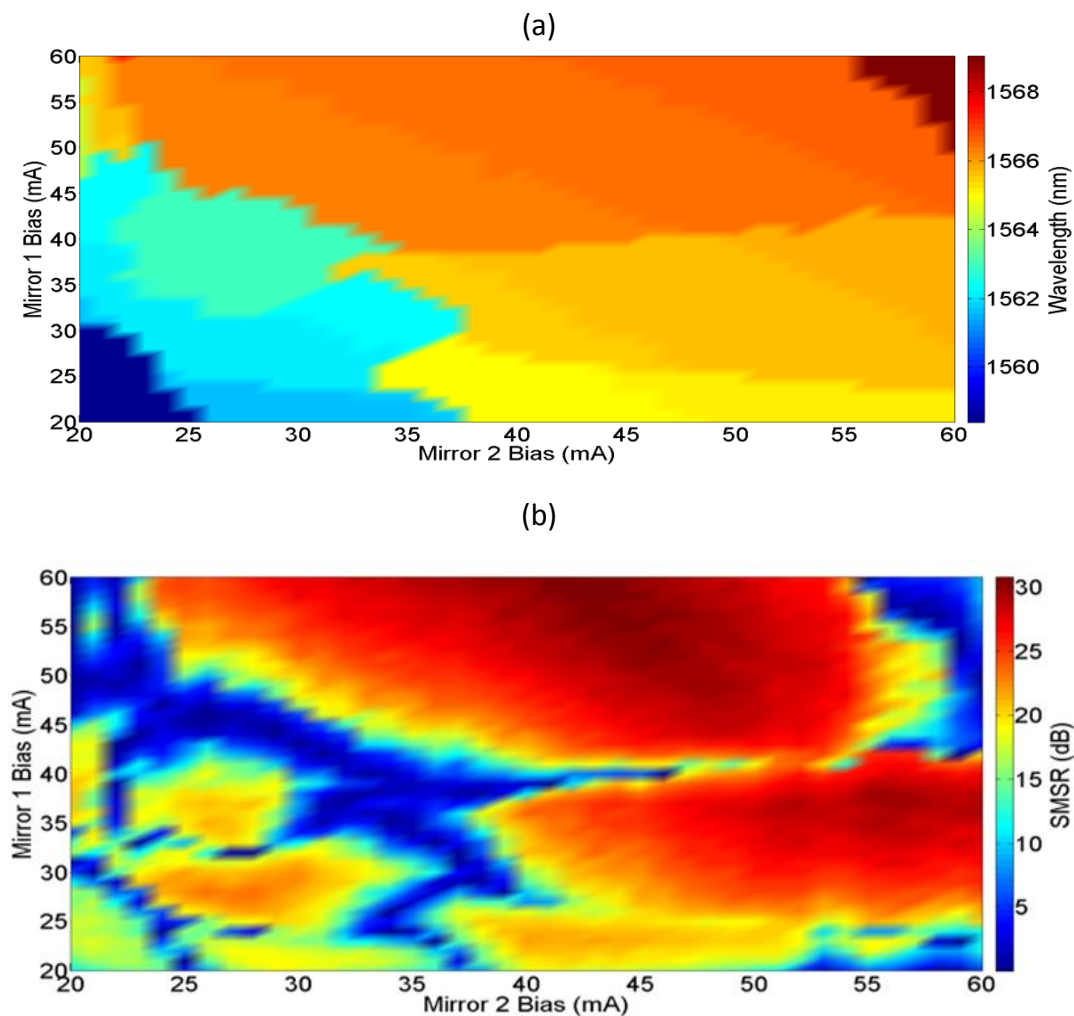


**Fig. 5.21:** (a) Contour plot demonstrating the peak wavelength and (b) SMSR of the laser for various bias conditions.



The focus of this section, however, is to complement the work presented in [13], [14]. To this end, one of the lasers was injection locked to longer wavelengths. This injection locking of the laser was achieved by coupling light from an external tunable laser source (output power of 2.40 dBm) into the device via the MMI. The behaviour of the laser was monitored by recording the optical output from the star coupler. Figure 5.22a shows the optical spectrum of the laser free running, and injection locked in approximately 5 nm increments from 1565nm to 1590nm. The laser under injection locking displays an SMSR  $>30$  dB for all wavelengths with the exception of 1590 nm. We believe that the reduced SMSR at 1590 nm is due to the wavelength being too far from the peak of the gain spectrum to fully suppress the free running lasing mode.

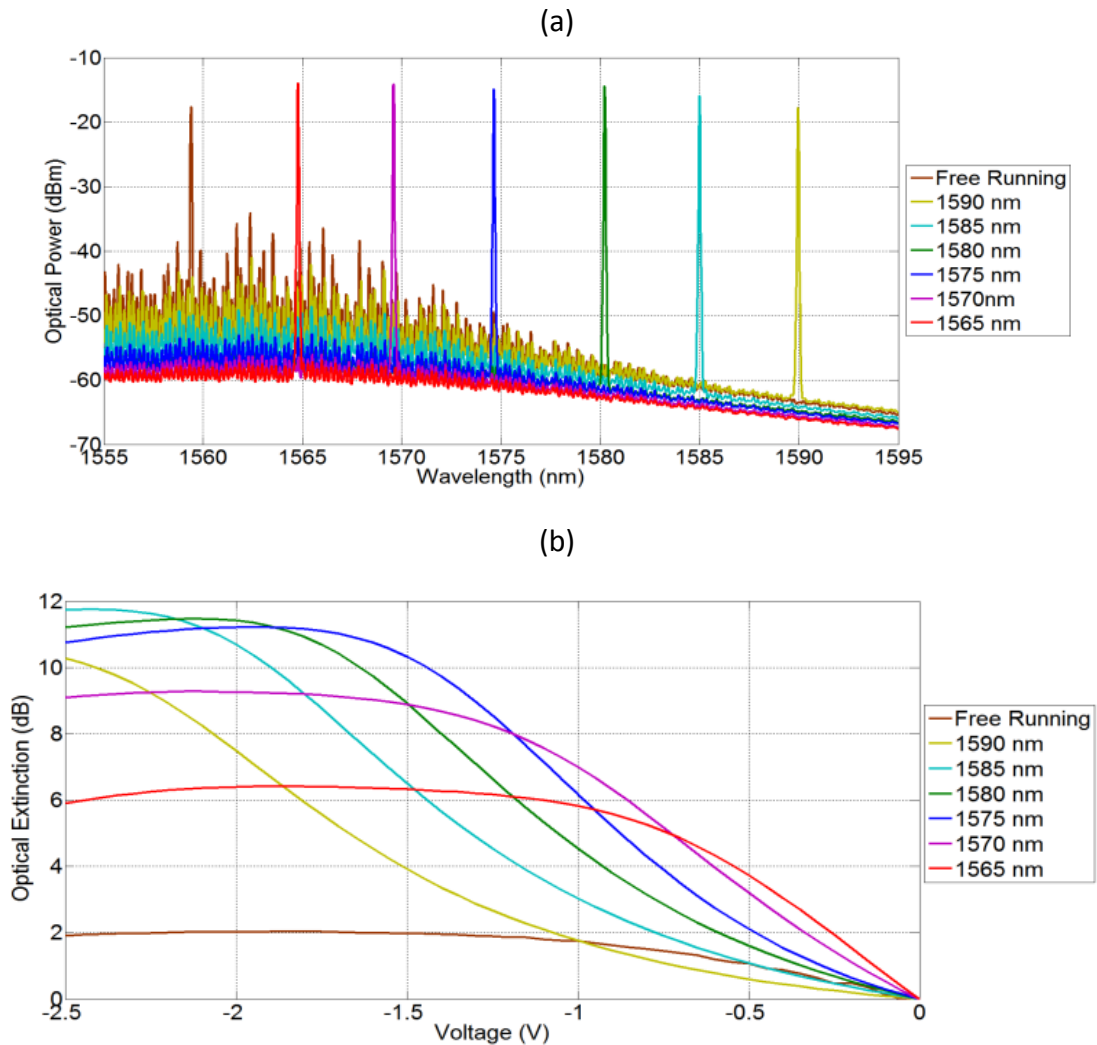


**Fig. 5.22:** (a) Optical spectra of free running and injection locked laser with external tuneable laser source (b) DC optical extinction of EAM integrated with injection locked SFP as part of the PIC.

To quantify the performance of the EAM while operating with the injection locked laser, the DC optical extinction was calculated. This was done by sweeping the bias of the EAM from 0 to -2.5 V for the various injection locking conditions described above. As before, all other sections were lightly biased to minimise absorption losses. The output power from the star coupler was recorded and each trace was normalised to its value at 0 V to produce the optical extinction trend presented in Figure 5.22b. The free running laser displayed an extinction of only 2 dB for a 2.5 V swing indicating that most of the light is already being absorbed at 0 V. The optical extinction dramatically improves as the wavelength of the injection locked laser is red shifted, peaking at a value of approximately 11.9 dB at 1585 nm. Encouragingly, this wavelength is comparable to the peak wavelength of the lasers of the previously mentioned comb source [13], which used an identical epitaxy design (Appendix A.1). The inclusion of high speed RF contacts to the EAM design would enable the modulation of the laser output to produce an eye diagram as in [15].

### 5.5 Integration of SFP Laser and EAM

To further investigate the feasibility of integrating an SFP laser with an EAM by means of injection locking a discrete device consisting of a laser and an EAM with contacts suitable for high speed modulation was designed and fabricated. A schematic of the device is shown in Figure 5.23. The single facet slotted laser consists of a 600  $\mu\text{m}$  long gain section which is enclosed by a 650  $\mu\text{m}$  mirror section and a cleaved facet to create a lasing cavity. The mirror section has six uniformly separated slots (108  $\mu\text{m}$  pitch) defining subsections of the laser cavity and providing optical feedback to the laser. The slots had a width and depth of 1  $\mu\text{m}$  and 1.83  $\mu\text{m}$  respectively. Wavelengths which are resonant with both the laser's effective cavity length and these subsections are enhanced with other non-resonant wavelengths being suppressed, inducing single mode operation through the Vernier effect. The 150  $\mu\text{m}$  EAM section curves to create a 7 degree facet which allows light to be



coupled off-chip while minimising reflections. A deep etched slot separates the mirror and EAM sections providing electrical isolation. Finally, a metal pad contacts the N semiconductor layers through an opening in the dielectric passivation creating a top side N metal.

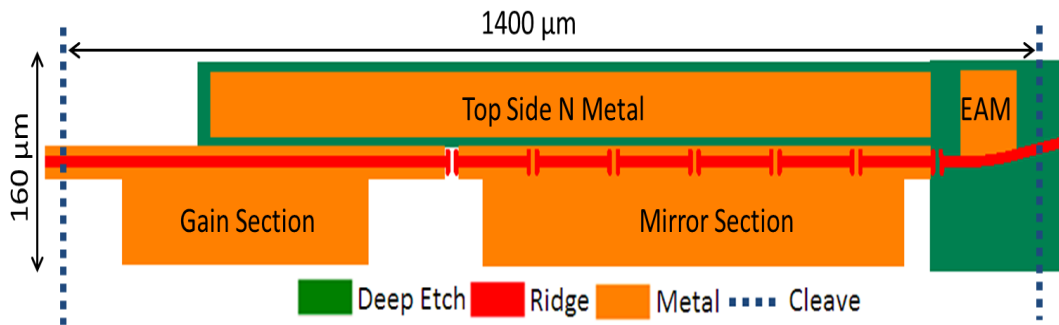


**Fig. 5.23:** Schematic of the device proposed in this section.

The gain and mirror sections of the laser were powered by DC probes while the EAM and the topside N Metal were contacted using a high-speed ground-signal (GS) probe. The N metal acted as a common ground for the entire device. Short focus lensed fibers were positioned close to the outputs of the devices to enable coupling to the facets. Initial testing of the device focused on characterising the absorption spectrum of the EAM. This was done by coupling light directly into the EAM section via the angled facet using an external TLS. The wavelength of the TLS was swept from 1540 nm to 1610 nm in 10 nm increments. The corresponding photocurrent was recorded from the EAM for varying applied voltage and is plotted in Figure 5.24. The applied voltage causes a reduction of the band gap energy. This reduction results in a red shift of the absorption spectra. Therefore, longer wavelengths which are not being absorbed at 0 V begin to experience attenuation at higher biases. This field induced absorption of longer wavelengths demonstrates the quantum confined Stark effect. This information is crucial for the integration of a single mode light source with the EAM as it indicates that the laser needs to operate at a wavelength of 1580 nm or longer to properly utilise the QCSE. Encouragingly, this wavelength is comparable to peak wavelength of the lasers of the previously mentioned comb source [13], which used an identical epitaxy design.

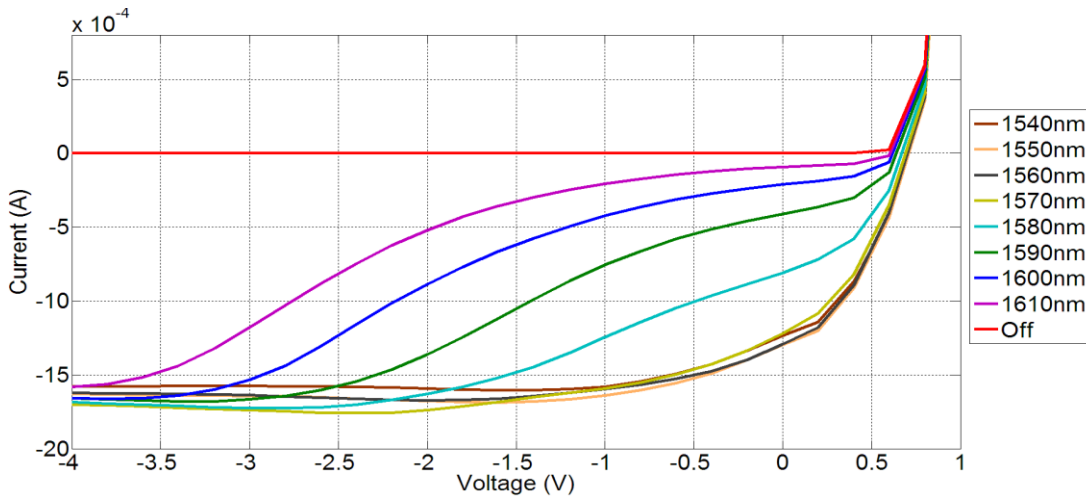


**Fig. 5.24:** EAM absorption for an off-chip tuneable laser source.

Both laser sections were biased to just above threshold (28 mA) with the EAM section lightly biased to minimise absorption losses. The output of the laser was coupled from the angled facet into an optical spectrum analyser. The corresponding cavity lengths were extracted from the resulting optical spectrum by taking its Fourier Transform (assuming the group index to be 3.5) and the results are shown in Figure 5.25. A large peak is clearly visible at 1290  $\mu\text{m}$  (A), corresponding to the length of the gain and mirror section of the laser. Peaks representing the sub cavities created by the mirror’s slot are also visible (B). This analysis confirms that the EAM section is not part of the lasing cavity and therefore, should not influence the lasers optical spectrum when modulated. The free spectral range (FSR) of the laser was calculated to be 3.17 nm [16]. This FSR is dictated by the separation of the slots in the mirror section and therefore can be manipulated as required.

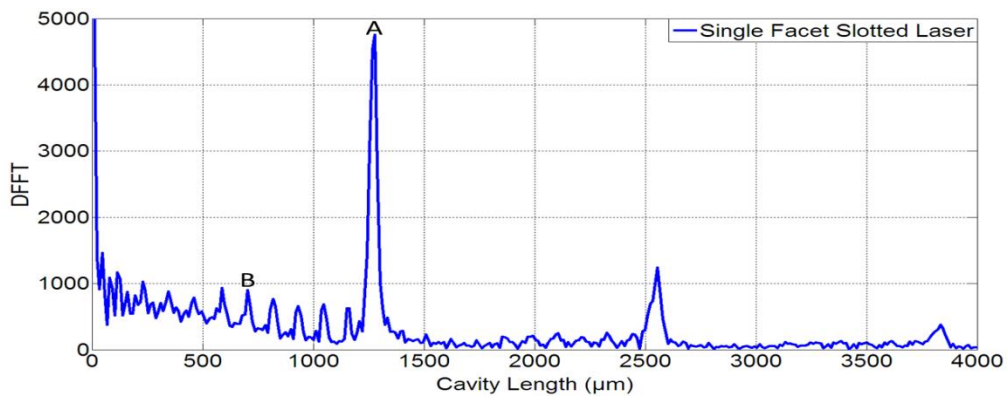


**Fig. 5.25:** Fourier transform analysis of laser’s optical spectrum near threshold.

Wavelength injection locking of the single facet laser was achieved by coupling light from the TLS directly into the gain section of the laser using the 90 degree facet. The behaviour of the laser was monitored by recording the optical output from the angled facet. Figure 5.26 shows the optical spectrum of the free running laser and injection locked in approximately 5nm increments from 1570 nm to 1595 nm. This result demonstrates that the slotted laser can be red-shifted sufficiently by means of injection locking, to operate with an EAM.

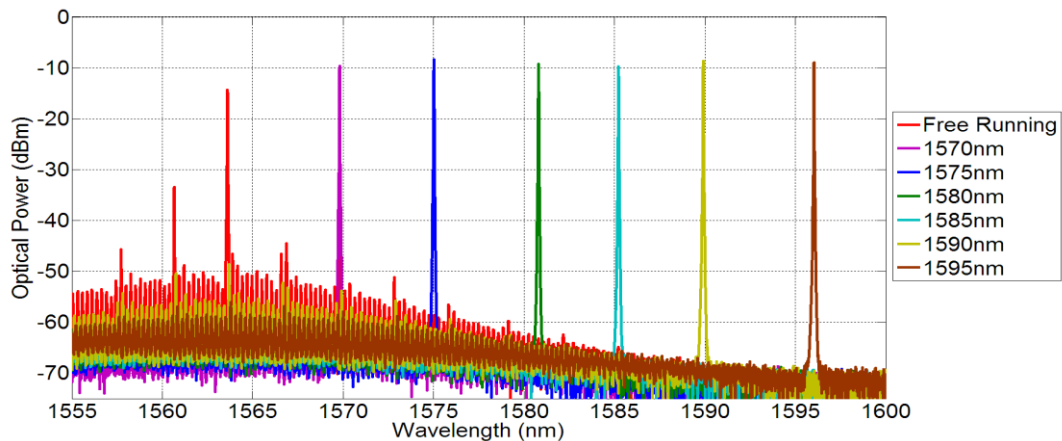


**Fig. 5.26:** Optical spectra of free running and injection locked laser with external tuneable laser source.

As in Figure 5.26, the SFP laser was externally injection locked to 1590 nm using an external TLS. A pseudorandom binary sequence (PRBS) source provided a signal with a pattern length of  $2^7-1$ . This sequence was passed through an RF amplifier to increase the peak to peak voltage of the signal to 1V. Finally, this amplified RF signal was combined with a DC bias of -1V before being applied to the EAM via a bias tee and high speed GS probes. The output signal from the device was boosted by an L band Erbium doped fiber amplifier (EDFA) to compensate for low optical power due to fibre coupling losses. The quality of the signal was then analysed with a 10 GHz photodiode and a digital communications analyser (DCA). Figure 5.27 displays the observed eye diagrams. Open eyes were achieved up to a speed of 5.5 Gbps demonstrating the successful operation of this device. Furthermore, this result confirms that such a device could potentially be applied in the CoWDM transmitter described in Figure 5.1. A DC measurement of the optical output power of the device

with the laser injection locked at 1590 nm and EAM biased at -0.5 V and -1.5 V respectively (corresponding to the maximum and minimum values of the applied RF signal) gave an extinction of approximately 8.6 dB.

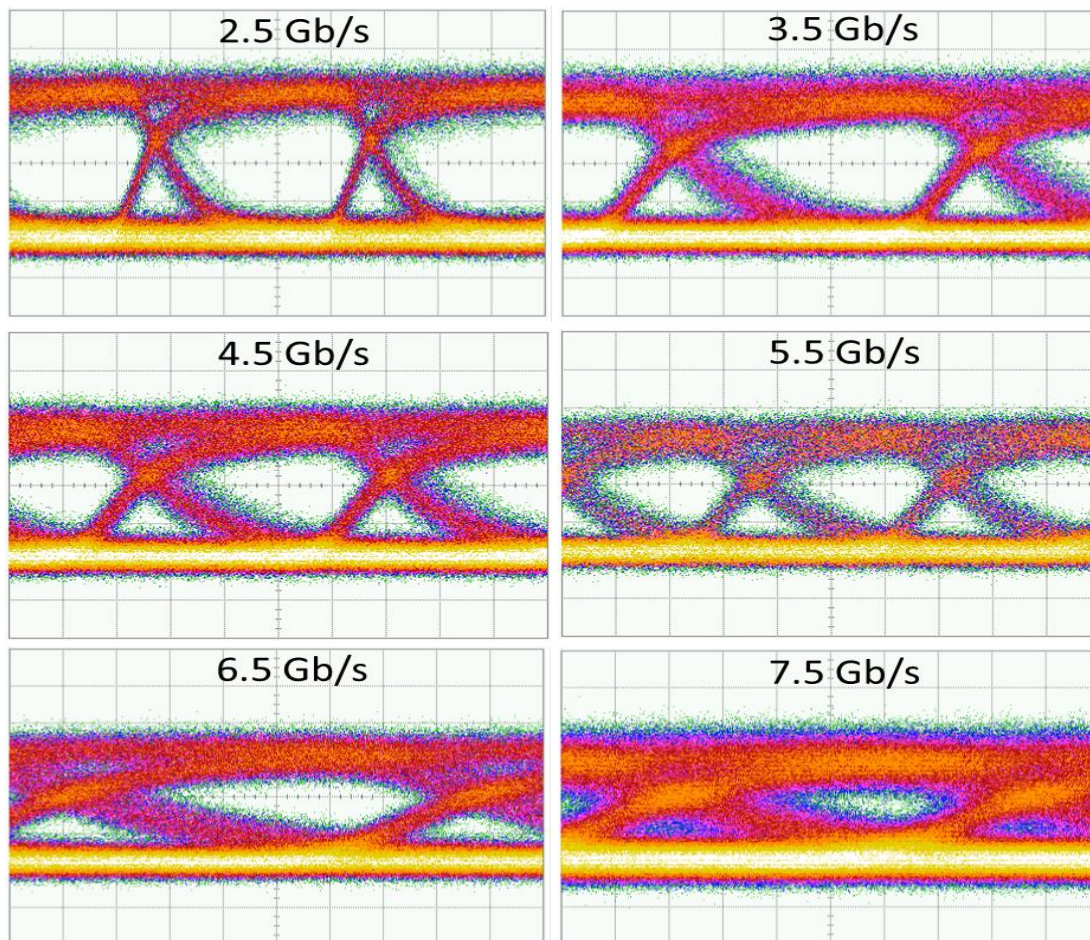


**Fig. 5.27:** Experimentally observed eye diagrams at bit rates ranging from 2.5 Gbps to 7.5 Gbps.

To quantify the limitations of this device, a vector network analyzer (VNA) was used to measure the electro optic 3 dB bandwidth of the EAM. For this measurement, the SFP Laser remained externally injection locked at 1590 nm and the EAM again received a DC bias of -1V. Figure 5.28 below shows the electro-optic S21 response of the EAM between 0.1 and 10 GHz. The 3 dB bandwidth was calculated to be approximately 5.25 GHz. This low bandwidth can be attributed to the use of an N doped substrate and the fact that the EAMs contact pad is separated from the N doped semiconductor layers by only 300 nm of dielectric which creates a significant

parasitic capacitance (approximately 17.25 pF). The high speed performance of the EAM could be improved by using a thicker dielectric layer or by using semi-insulating (SI) substrates and more advanced high speed EAM designs such as demonstrated in [15].

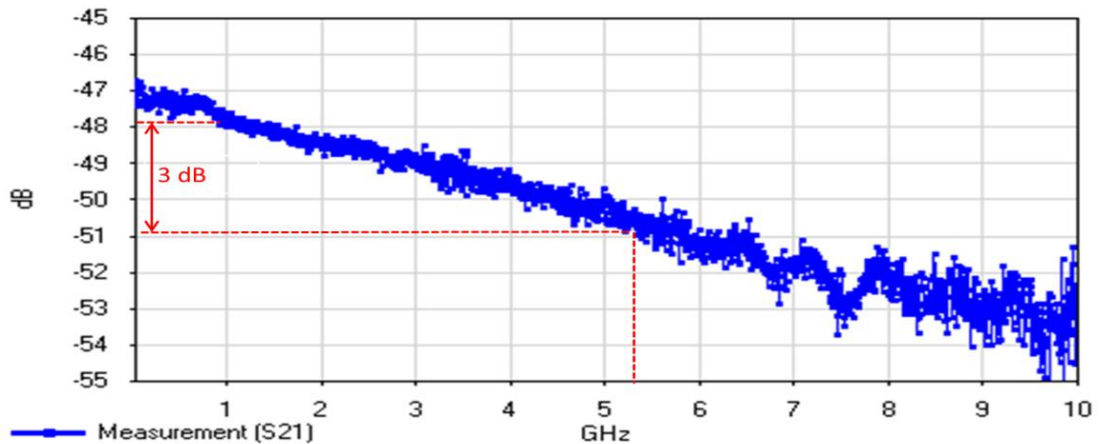


**Fig. 5.28:** Electro-optic S21 measurement of electroabsorption modulator.

## 5.6 Summary

Section 5.4 demonstrated the monolithic integration of a 1x2 MMI, two SFP lasers, two EAMs, and a star coupler to create a photonic integrated circuit suitable for use as part of a regrowth free CoWDM transmitter. Moreover, the fabrication of this device has been achieved without the use of advanced fabrication techniques such as epitaxial regrowth or E-beam lithography. The correct operation of each of these components has been experimentally verified along with confirmation of no significant optical crosstalk between the lasers. Building on previously published work, one of the lasers was injection locked up to 30 nm away from the main free running lasing mode. Crucially, the optical extinction of the EAM was shown to improve by up to 9.8 dB when the laser was injection locked to longer wavelengths.

Section 5.5 demonstrated a single facet slotted laser injection locked up to 30 nm away from the main free running lasing mode. This complements the optical absorption characteristics of the EAM which show that for this particular epitaxy, a wavelength of 1580 nm or longer is required to properly take advantage of the quantum confined Stark effect. Utilising these results, an injection locked SFP laser

has been integrated with an EAM to produce a high quality 2.5 GB/s eye diagram. The 3 dB electro optic bandwidth of the EAM was measured as approximately 5.25 GHz. Therefore, we expect that the bit rate of the eye can be significantly increased with the use of more advanced epitaxy and EAM designs. To this end, Chapter 6 will investigate of high speed modulators and epitaxy with the aim of increasing the data rate of the developed PICs.

### **Bibliography**

- [1] R. Nagarajan, M. Kato, J. Pleumeekers, P. Evans, S. Corzine, S. Hurtt, A. Dentai, S. Murthy, M. Missey, R. Muthiah, R. A. Salvatore, C. Joyner, R. Schneider, M. Ziari, F. Kish, and D. Welch, "InP Photonic Integrated Circuits," *IEEE J. Sel. Top. QUANTUM Electron.*, vol. 16, no. 5, 2010.
- [2] M. Smit, X. Leijtens, H. Ambrosius, E. Bente, and van der Tol, "An introduction to InP-based generic integration technology," *Semicond. Sci. Technol.*, vol. 29, no. 8, p. 83001, Jun. 2014.
- [3] S. Keyvaninia, S. Verstuyft, L. Van Landschoot, F. Lelarge, G.-H. Duan, S. Messaoudene, J. M. Fedeli, T. De Vries, B. Smalbrugge, E. J. Geluk, J. Bolk, M. Smit, G. Morthier, D. Van Thourhout, and G. Roelkens, "Heterogeneously integrated III-V/silicon distributed feedback lasers," *Opt. Lett.*, vol. 38, no. 24, p. 5434, Dec. 2013.
- [4] E. J. Skogen, J. S. Barton, S. P. Denbaars, and L. A. Coldren, "A quantum-well-intermixing process for wavelength-agile photonic integrated circuits," *IEEE J. Sel. Top. Quantum Electron.*, vol. 8, no. 4, pp. 863–869, Jul. 2002.
- [5] B. C. Qiu, "Monolithic integration in InGaAs/InGaAsP multiple quantum well structures using laser and plasma processing," in *IEE Colloquium on Optoelectronic Integration and Switching*, 1997, vol. 1997, pp. 1–1.
- [6] T. Tsuchiya, J. Shimizu, M. Shirai, and M. Aoki, "InGaAlAs selective-area growth on an InP substrate by metalorganic vapor phase epitaxy," in *International Conference on Indium Phosphide and Related Materials*, 2003.,



pp. 546–549.

- [7] M. Smit, X. Leijtens, and E. Bente, “A generic foundry model for InP-based photonic ICs,” in *Optical Fiber Communication Conference and Exposition (OFC/NFOEC), 2012 and the National Fiber Optic Engineers Conference, 2012*.
- [8] L. B. Soldano and E. C. M. Pennings, “Optical multi-mode interference devices based on self-imaging: principles and applications,” *J. Light. Technol.*, vol. 13, no. 4, pp. 615–627, Apr. 1995.
- [9] Q. Lu, W. Guo, D. Byrne, J. F. Donegan, and S. Member, “Design of Slotted Single-Mode Lasers Suitable for Photonic Integration,” vol. 22, no. 11, pp. 787–789, 2010.
- [10] C. Dragone, “An N\*N optical multiplexer using a planar arrangement of two star couplers,” *IEEE Photonics Technol. Lett.*, vol. 3, no. 9, pp. 812–815, Sep. 1991.
- [11] Jeong Hwan Song, H. N. J. Fernando, B. Roycroft, B. Corbett, and F. H. Peters, “Practical Design of Lensed Fibers for Semiconductor Laser Packaging Using Laser Welding Technique,” *J. Light. Technol.*, vol. 27, no. 11, pp. 1533–1539, Jun. 2009.
- [12] D. A. B. Miller, “Band-Edge Electroabsorption in Quantum Well Structures: The Quantum-Confined Stark Effect,” *Phys. Rev. Lett.*, vol. 53, no. 22, p. 2173, 1984.
- [13] J. K. Alexander, P. E. Morrissey, H. Yang, M. Yang, P. J. Marraccini, B. Corbett, and F. H. Peters, “Monolithically integrated low linewidth comb source using gain switched slotted Fabry-Perot lasers.”
- [14] W. Cotter, D. Goulding, B. Roycroft, J. O’Callaghan, B. Corbett, and F. H. Peters, “Investigation of active filter using injection-locked slotted Fabry-Perot semiconductor laser,” *Appl. Opt.*, vol. 51, no. 30, p. 7357, Oct. 2012.
- [15] C. L. M. Daunt, J. O’Callaghan, K.-H. Lee, H. Yang, R. J. Young, K. Thomas, E.

Pelucchi, B. Corbett, and F. H. Peters, "Compact Electroabsorption Modulators for Photonic Integrated Circuits, Using an Isolated Pedestal Contact Scheme," *IEEE Photonics Technol. Lett.*, vol. 24, no. 5, pp. 356–358, Mar. 2012.

- [16] S. W. C. Larry A. Coldren, *Diode Lasers and Photonic integrated Circuits*. Santa Barbara: Wiley-Interscience Publication, 1995.



# Chapter 6

## High Speed Electroabsorption Modulators

### 6.1 Introduction

InP based electroabsorption modulators (EAMs) are a key component of PICs as they offer high speed operation, a large extinction ratio and a low driving voltage [1]. Lumped element EAMs are commonly favoured over their traveling wave counterparts for such applications due to their compact design and simple layout. Design consideration such as electrode configuration and epitaxial structure will be discussed in this chapter. This will be followed by a detailed discussion on the characterisation of fabricated high speed modulators.

### 6.2 High Speed EAM Electrode Design

As discussed in Chapter 2, EAMs are based on the principle of the QCSE and will therefore be exclusively operated in reverse bias. The electro optic bandwidth of such a reverse biased device is limited by the intrinsic capacitance of the optical waveguide. However, the varying electric field used to create the optical intensity modulation is applied to the semiconductor junction via a metal electrode deposited on top of the ridge. Therefore, the bandwidth of the modulator also directly depends on the design of this electrode. Two well published designs will be discussed in this section: lumped element [2] and traveling wave electrodes [3].

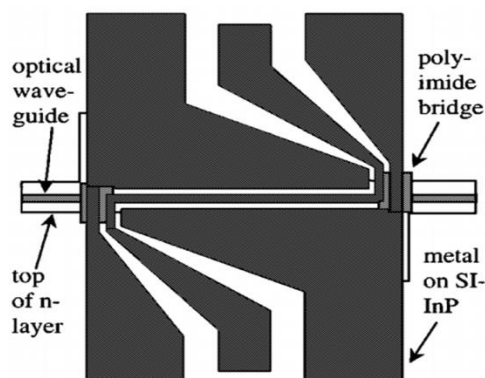


**Fig. 6.1:** Schematic of a traveling wave EAM showing the microwave electrodes and optical waveguide [4].

In a traveling wave configuration such as shown in Figure 6.1, the RF signal is applied to one end of the device where it propagates along the waveguide with the optical mode. To prevent reflections of high frequency electrical signals (where the wavelength is of the same order as the electrode length) due to impedance mismatching, the end of the electrode is connected to a 50  $\Omega$  termination [5]. If the electrode is not terminated correctly, the reflected power can create a standing wave introducing additional losses. The advantage of the traveling wave design is that it enables the device to achieve higher speeds as the intrinsic capacitance of the ridge structure is distributed along the length of the phase shifting electrode. The driving voltage and extinction ratio of the device can therefore be improved by increasing the device length. As the applied electric field propagates along the waveguide with the optical mode, a mismatch between the two waves can occur. The electrical bandwidth for a lossless RF electric can be describes as a function of the speed of light ( $c$ ), the length of the electrode ( $l$ ) and optical ( $n_o$ ) and electrical ( $n_\mu$ ) refractive indices [6].

$$f_{3dB} = \frac{1.4c}{\pi|n_o - n_\mu|l}$$

Advanced designs such as capacitively loaded electrodes have been demonstrated to match the velocity of the microwave and the group velocity of the optical signal of an MZM, minimising the phase offset [7]. However, EAMs are not as susceptible to the losses associated with velocity mismatching as MZMs due to their shorter lengths and exponential absorption characteristics. As traveling wave EAMs are usually less than 300  $\mu\text{m}$  in length, most of the light is absorbed while the two waves are still relatively in phase. Therefore, traveling wave EAM electrode designs commonly focus on reducing other forms of loss such as reflection loss and propagation loss. Although such EAM designs offer many advantages, they occupy a large area when compared to other photonics devices such as lasers due to their contact pad requirements. This large footprint is problematic for their application in high density photonic integrated circuits as they will reduce the device per wafer ratio, which in turn will increase fabrication costs. They also require a 50 Ohm

termination at the end of the electrode to minimise RF reflections which increases the complexity of packaging.

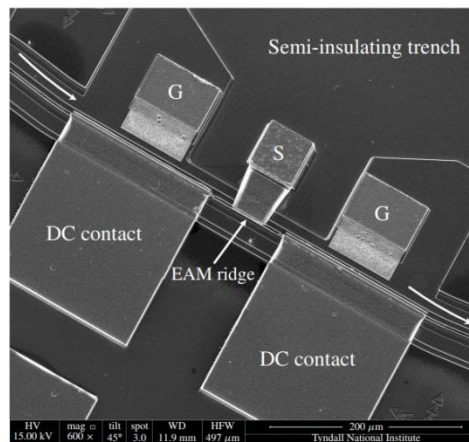


**Fig. 6.2:** Schematic of a lumped element EAM showing the microwave electrodes and optical waveguide [2].

Lumped element EAMs as shown in Figure 6.2 offer a compact alternative to their traveling wave counterparts. Utilising a simpler electrode design, the microwave signal is applied to the centre of the waveguide. A reverse biased lumped EAM can be represented as a differential resistance ( $R$ ) associated with the doped semiconductor layers and a junction capacitance ( $C_i$ ). As the devices discussed in this chapter will be based on deep etched ridges, the junction capacitance can be considered as a parallel plate capacitor where  $d_i$  is the intrinsic region thickness,  $A$  is the surface area of the ridge and  $\epsilon$  is the permittivity of the material.

$$C_i = \frac{\epsilon A}{d_i}$$

Contact pads are required to deliver the signal to the device as the ridge structure is too narrow to contact using probes or wire bonds. These pads can introduce parasitic impedances if not designed correctly, as the contact pads result in a parasitic capacitance ( $C_p$ ) with the underlying n doped layers (Figure 6.3). This parallel capacitance can severely limit the performance of the modulator.

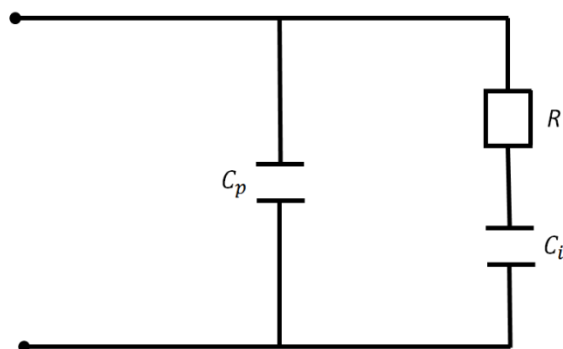


**Fig. 6.3:** Equivalent circuit of lumped element EAM.

Lumped element electrodes are therefore only applicable if the contacts are optimised to maximise the bandwidth of the devices. If the parasitic capacitance is much smaller than the junction capacitance, the 3 dB bandwidth can be expressed as a function of the electrical response time  $\tau = RC_i$ . Unlike traveling wave designs, it is not feasible to make lumped element EAMs significantly longer to improve the extinction ratio due to its RC bandwidth limitation [8].

$$f_{3dB} = \frac{1}{2\pi RC_i}$$

Traditionally, parasitic capacitances attributed to lumped element devices have been minimised using two techniques. The first is to run the RF contact from the ridge to a metal pad on the semi-insulating substrate [9]. However, this approach requires a very thick dielectric to minimise capacitance attributed to the signal metal traversing the ridge sidewall and n doped layers. An undesirable height mismatch between the top of the ridge and the contact pads is also created. The second approach is to planarise the surface of the wafer mid fabrication process using dielectrics such as BCB or polyimide [10]. The signal and n metal bond pad are then formed on top of the planarised dielectric. These bond pads commonly suffer from delamination issues making the devices difficult to characterise or package.

The isolated pedestal contact offers an alternative solution which addresses some of the issue described above [11]. Pedestals are formed during the ridge etch process and are therefore the same height as the top of the waveguide. The centre pedestal is encircled by a deep trench which penetrates into the semi-insulating

layers, fully isolating the signal pad from the surrounding conductive layers. The area between the signal pedestal and the ridge is planarised using BCB, facilitating the formation of a bridge metal between the two sections. This approach was favoured over an undercut airbridge structure [12] which proved impractical due to the incompatibility of the required crystallographic dependent wet etch and the need to contact the EAM side on. A second set of metal traces traverse the sides of the ground pedestals, which are insulated with a dielectric, shorting the ground pads to the n doped layers. Forming the contact pads on these planar semiconductor pedestals (Figure 6.4) has the dual advantage of improving adhesion and preventing deformation of GSG probes which would lead to inaccurate measurements. This configuration also provides an excellent platform for flip-chip packaging due to the uniformity of the ridge and contact pad heights.

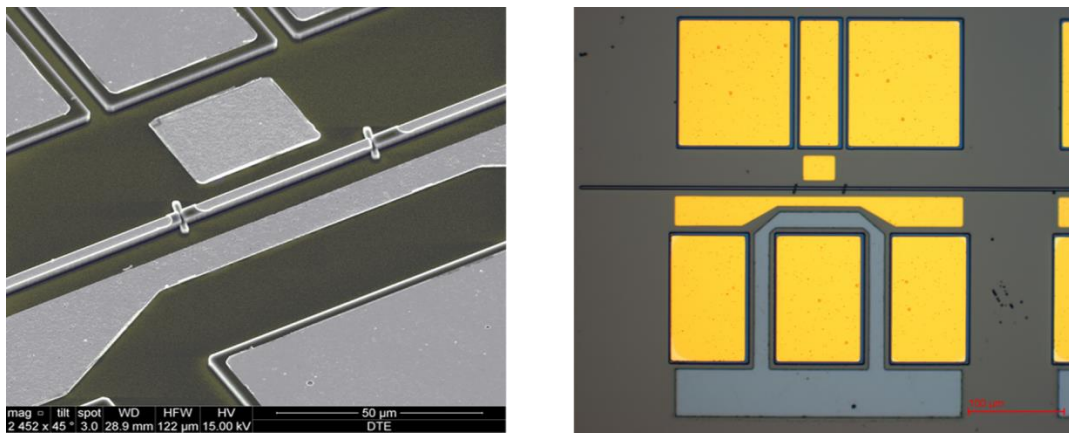


**Fig. 6.4:** SEM and microscopic images of isolated pedestal contacts.

### 6.3 High Speed Epitaxial Design

Power handling must be considered when designing the epitaxial structure for EAMs, so that a sufficiently large optical extinction can be produced to generate the eye diagrams that are required as part of the CoWDM signal. A contributing factor to the saturation limit of absorption modulators is carrier pile up. As layers of semiconductor material are grown to form the epitaxy, discontinuities in the conduction and valence bands create heterobarriers. Transmission across these barriers is dominated by two mechanisms: thermionic emission and field emission. Thermionic emission occurs when carriers have sufficient energy to cross the

heterobarriers. However, since this emission occurs on a quantum mechanical scale there is always a finite probability that a carrier with sufficient energy would be reflected by the heterojunction. The energy required for thermionic emission to occur must be minimised by reducing the potential step of the barriers [13]. Field emission describes the probability of carriers tunnelling through the heterojunction potential. This probability increases as a function of applied voltage because the barrier becomes thinner with applied electric field. Heavy holes will tend to tunnel the least due to their comparatively large effective mass. For this reason, it is preferable to use an alloy that has a large conduction band offset and minimises the valence band discontinuities [14]. Unlike InGaAsP, which is traditionally used in PICs, AlInGaAs produces minimal valence band heterobarriers at the expense of a larger conduction band offset. This lower discontinuity will increase both thermionic and field emission of the heavy holes reducing carrier pile up. As an EAM relies on the QCSE, its bandwidth is limited by the electric field and not limited by the carrier transit time. This transit time however, can influence the dynamic extinction ratio and power handling abilities of the devices [15]. Photogenerated carriers slowly sweeping out of the intrinsic region can influence the QCSE by perturbing the electric field. The mobility of the carriers is defined by the alloys used to form the multiple quantum well region and their respective thicknesses. It is not feasible to reduce the thickness of the intrinsic region as this would limit the bandwidth of the devices due to an increased capacitance. The transit time is limited by the mobility of the slowest carrier, which are the heavy holes due to their higher effective mass. Therefore, the lower drift velocity of the heavy holes can be compensated for while still preserving the intrinsic region thickness by offsetting the MQWs.

The epitaxial structure used for the EAMs was based on the work reported in [16] and listed in Appendix A.2. It contained eight 7.5 nm wide compressively strained AlInGaAs quantum wells separated by 10 nm wide barriers and was grown on a semi-insulating InP substrate. A 70 nm undoped AlInGaAs layer was added between the wells and the p layers to minimise valence band discontinuities, reducing photogenerated hole pile up. The quantum wells were grown on a 210 nm undoped InGaAsP layer to create equal carrier transit times. This 420 nm thick

intrinsic region also reduced the capacitance of the waveguide. SIMWINDOWS [17] was used to produce a representation of the epitaxial layers (without contacts for clarity) and a band diagram of the epitaxy under an applied bias of -2 V, as shown in Figure 6.5.

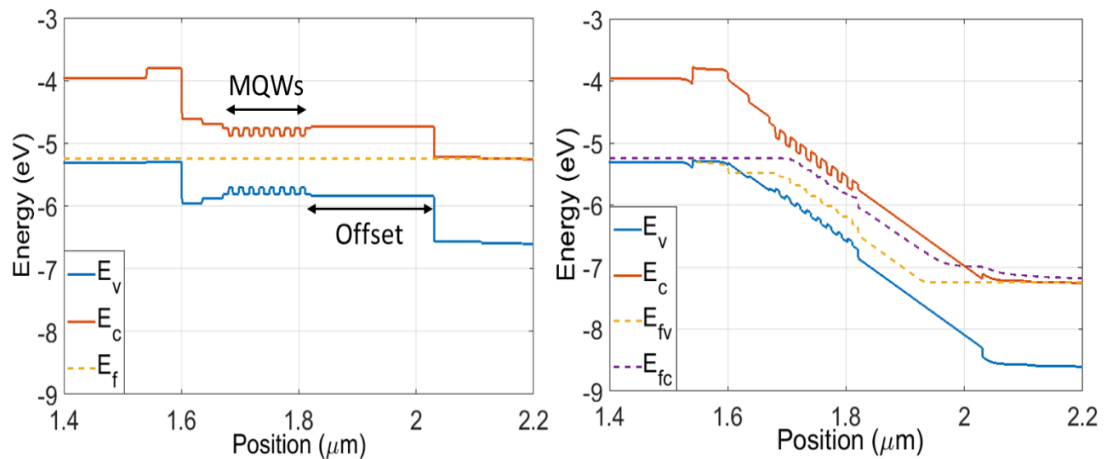


**Fig. 6.5:** Representation of epitaxial layers (left) and band diagram of epitaxy under an applied bias of -2 V (right) using SIMWINDOWS.

The epitaxy was grown on a 2 inch semi-insulating InP wafer using metal organic vapor phase epitaxy (MOVPE) in a horizontal reactor, with nitrogen as the carrier gas [18]. Zinc is a commonly used p dopant for InP [19] and was also used to form a highly doped InGaAs cap layer to facilitate the formation of a low resistance p contact. Silicon was used as the n dopant because it is known to diffuse very little in InP semiconductors [20]. Test structures were fabricated using the DC process to ensure that the epitaxy was grown as designed and can withstand the fabrication processes required to form photonic devices. Diffusion of dopants into the quantum wells during the growth or exposure to the ICP plasma can have a severe effect on device performance such as interfering with the Coulomb interactions between the exciton's confined electron hole pairs. Other concerns include the oxidation of the Al in the quantum wells which readily oxidises when exposed to air. Figure 6.6 shows that characterisation of pillar photodiodes. The VI confirms that a high quality diode with low contact resistance was formed with negligible leakage current under reverse bias. Vertical illumination of the photodiode demonstrates the electric field induced absorption shift associated with the QCSE.

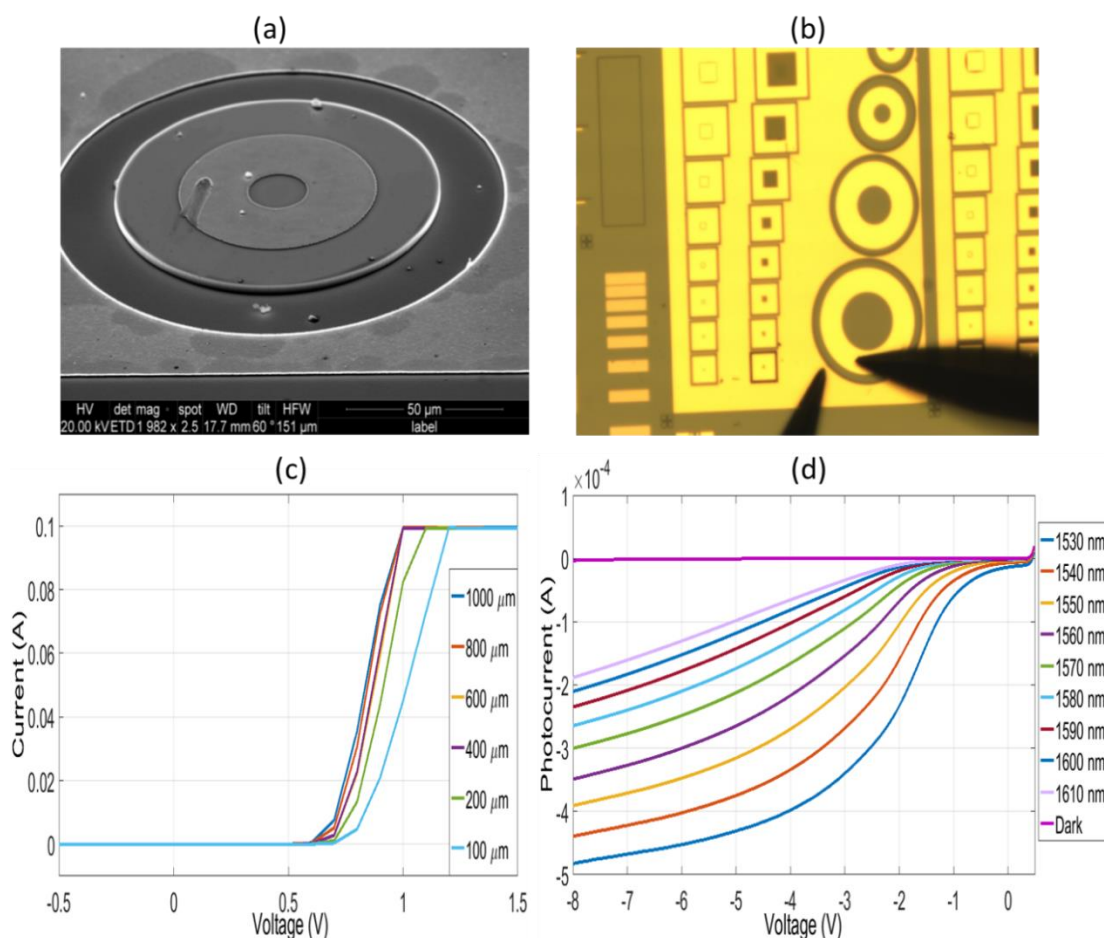


**Fig. 6.6:** (a) SEM and (b) microscopic image of pillar photodiode under test (c) VI displaying low resistance and leakage current for varying applied bias and (d) a field induced absorption shift of photodiode under surface illumination.

Though the epitaxy describe above is designed for the fabrication of high speed EAMs, it must also be compatible with laser designs so that it can be eventually applied to the realisation of the CoWDM PIC described in Chapter 2. Therefore, it is important that the material provides sufficient optical gain under forward bias. An array of 500 μm long Fabry Perot lasers were fabricated and characterised to verify that the material is capable of confining sufficient carriers for lasing to occur. Figure 6.7 shows that the lasers can produce 1.5 mW of power with a lasing spectrum centred at 1517 nm.



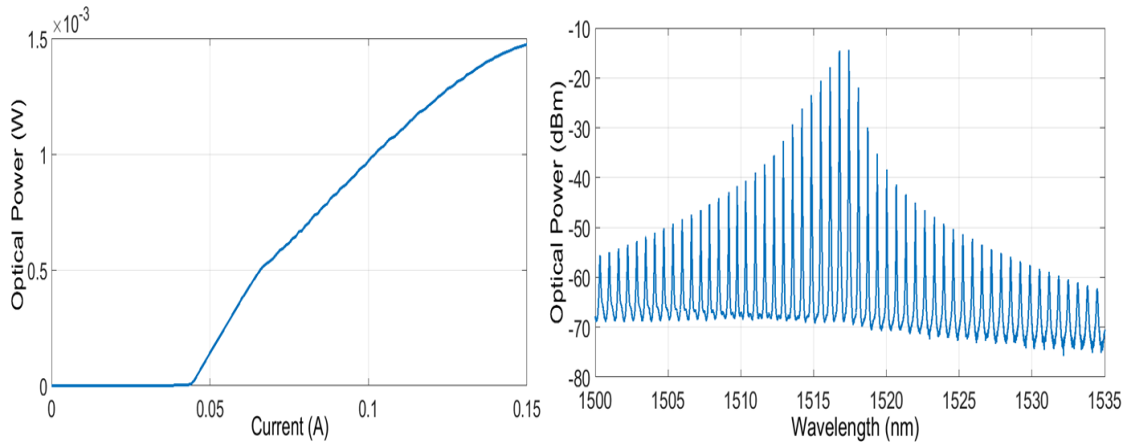


**Fig. 6.7:** Optical power vs. current plot (left) and optical spectrum (right) of Fabry Perot laser.

#### 6.4 RF Pedestal Characterisation

The frequency response of a lumped element electro-optic device is limited by the capacitance and resistance of the semiconductor junction as well as by the parasitics associated with the RF contact pads. Therefore, to fully understand the high speed performance of the device, the contribution of the pedestals must be quantified. To this end, test structures consisting of GSG pedestals and an isolation trench were also included on the mask design. These RF pads are identical to those used in the real devices and therefore similar capacitances and resistances can be assumed. Figure 6.8 displays a microscopic image of an RF test structure as well as a Smith chart of the its scattering matrix S11 measurement from 0-20 GHz using a vector network analyser (VNA). A capacitance of 56.6 fF was extracted by fitting this data to an equivalent circuit model. This relatively high capacitance could be reduced by decreasing the size of the pedestals while increasing the width of the isolation trench. The isolation etch provided a DC resistance exceeding 500 M $\Omega$ .

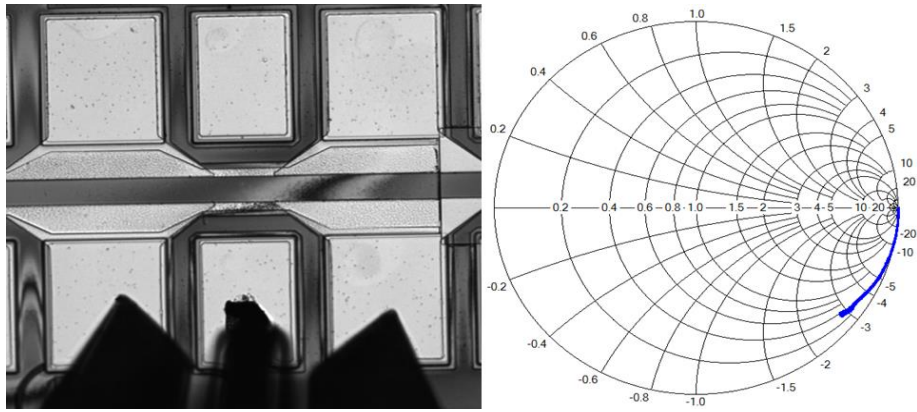


**Fig. 6.8:** Microscopic image of RF test structure and corresponding S11 measurement.

### 6.5 Lumped Element EAM Array

The device design centres around a ridge waveguide structure which penetrates through the quantum wells and into the N layers to provide high optical confinement. Two angled slots provide electrical isolation between the EAM and the adjacent 150  $\mu\text{m}$  SOA sections which were added to artificially widen the test bar, simplifying the characterisation process. The design utilises a planar isolated pedestal

GSG

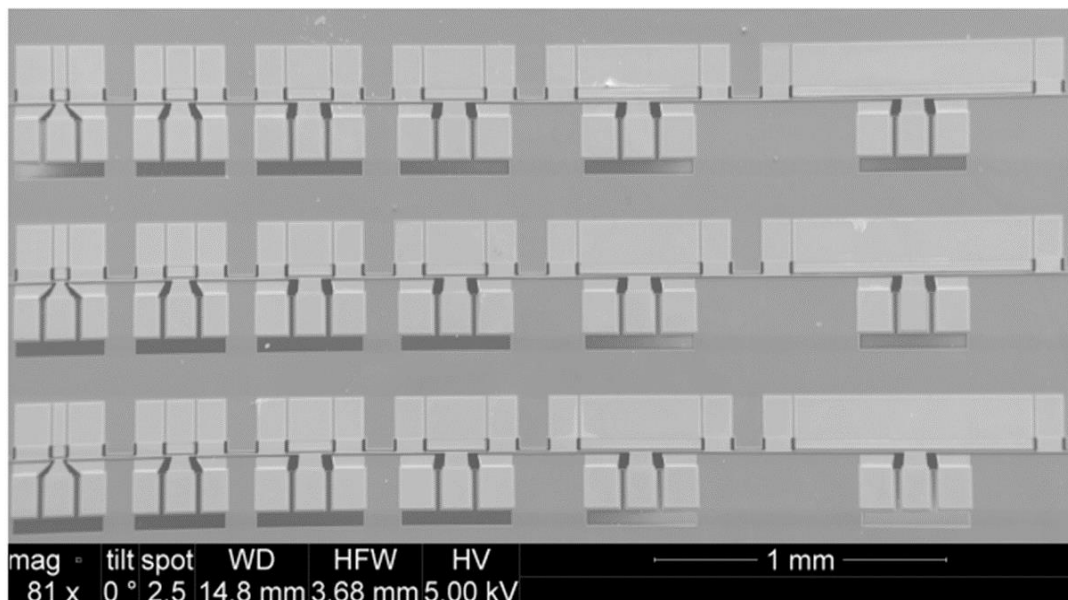


**Fig. 6.9:** SEM image of arrayed lumped element EAMS.

configuration with a pitch of 125  $\mu\text{m}$  and a lumped electrode layout. The pedestals are electrically isolated by a trench which encircles the signal pad. The devices were laid out in an arrayed format with a varying EAM length of 50, 100, 150, 200, 400 and 800  $\mu\text{m}$  respectively. Such a wide variation in device length was included to account for the tradeoff between the electro optical bandwidth and the optical extinction. A range of ridge widths were also included to add an extra dimension to the analysis. The scattering matrix S11 of the full array of EAM devices was recorded for varying reverse biases (Figure 6.9a). The smith chart is a graphical representation of the resistance and reactance of a device as a function of signal frequency, whose impedance can be extracted by fitting the data to an appropriate circuit model.

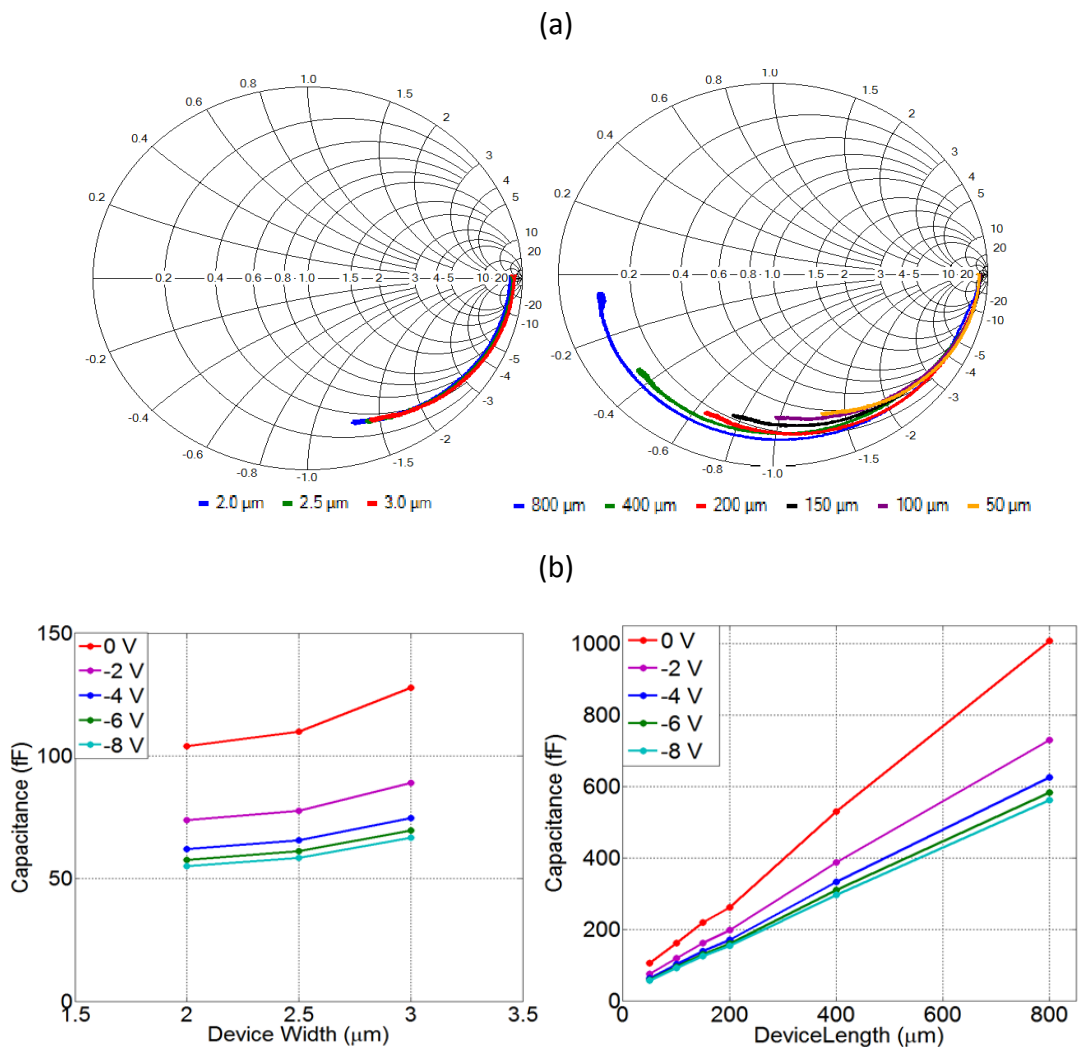


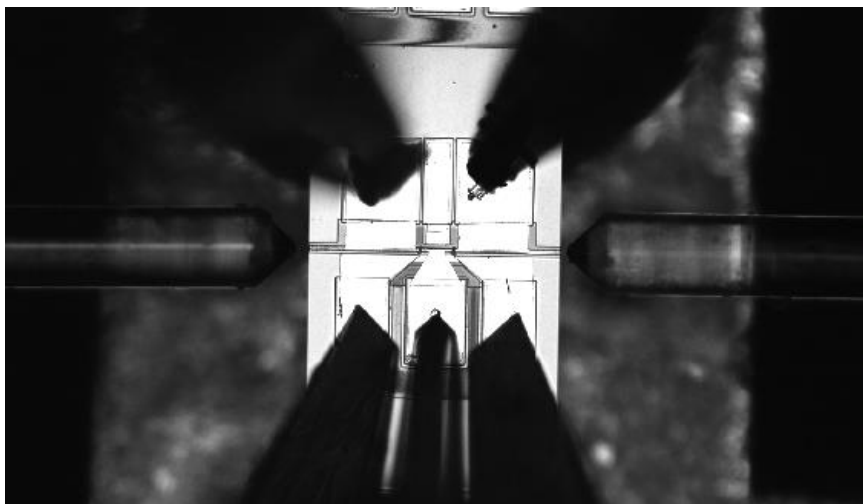
**Fig. 6.9:** (a) EAM S11 measurement and (b) extracted capacitance for a 50  $\mu\text{m}$  device as a function of ridge width (left) and for a 2.0  $\mu\text{m}$  ridge width as a function of device length (right).

Using an expanded circuit model and the parasitic values extracted from the RF test structure, it was possible to plot the capacitance of the ridge structure as a function of bias, as in Figure 6.9b. The decreasing capacitance as a function of reverse bias is a result of the increasing depletion region thickness. As expected from the parallel plate capacitor analogy, the capacitance decreases linearly with reducing device length and ridge width. Since a low device resistance was evident across the chip, the 50  $\mu\text{m}$  device with a ridge width of 2.0  $\mu\text{m}$  was identified as having the fastest electrical response time as a result of its low capacitance. This device was cleaved so that the EO 3 dB bandwidth and optical extinction could be characterised.

### 6.6 50 $\mu\text{m}$ Lumped Element EAM

Initial testing of the cleaved 50  $\mu\text{m}$  EAM focused on the characterisation of its absorption spectrum. This was achieved by injecting light into the device using an external tunable laser source whose wavelength was swept from 1530 nm to 1580 nm in 10 nm increments. Short focus lensed fibers were positioned close to the outputs to enable coupling to the facets. The EAM was contacted with a GSG probe (Figure 6.10a) while the SOA sections were lightly biased using DC probes to minimize absorption losses. The transmitted optical power was recorded from the EAM for varying applied voltage and is plotted in Figure 6.10b. The applied voltage causes a reduction of the band gap energy. This reduction results in a red shift of the absorption spectra. Therefore, longer wavelengths which are not being absorbed at

(a)



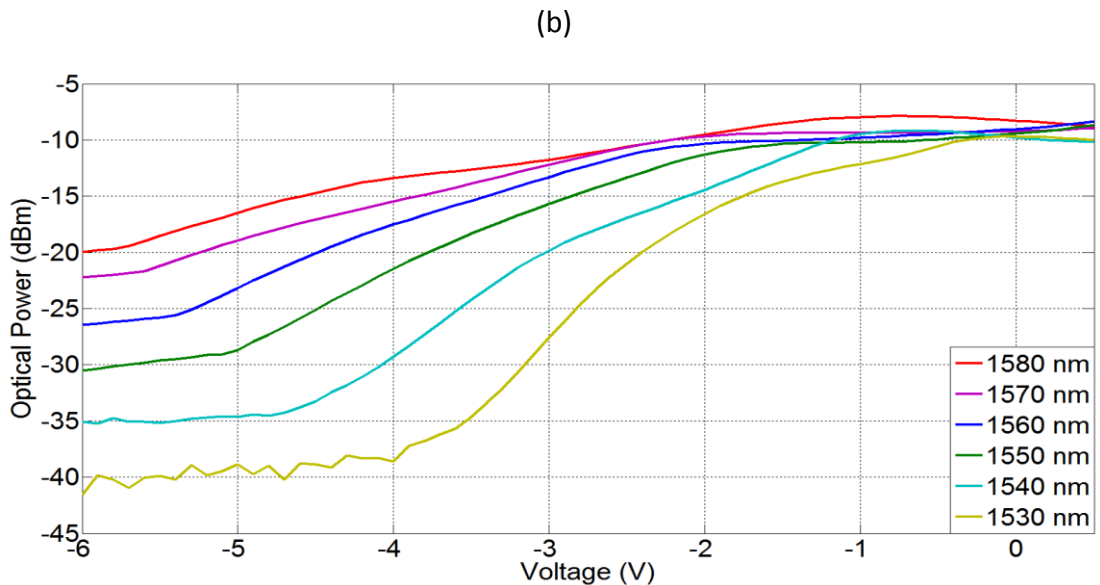
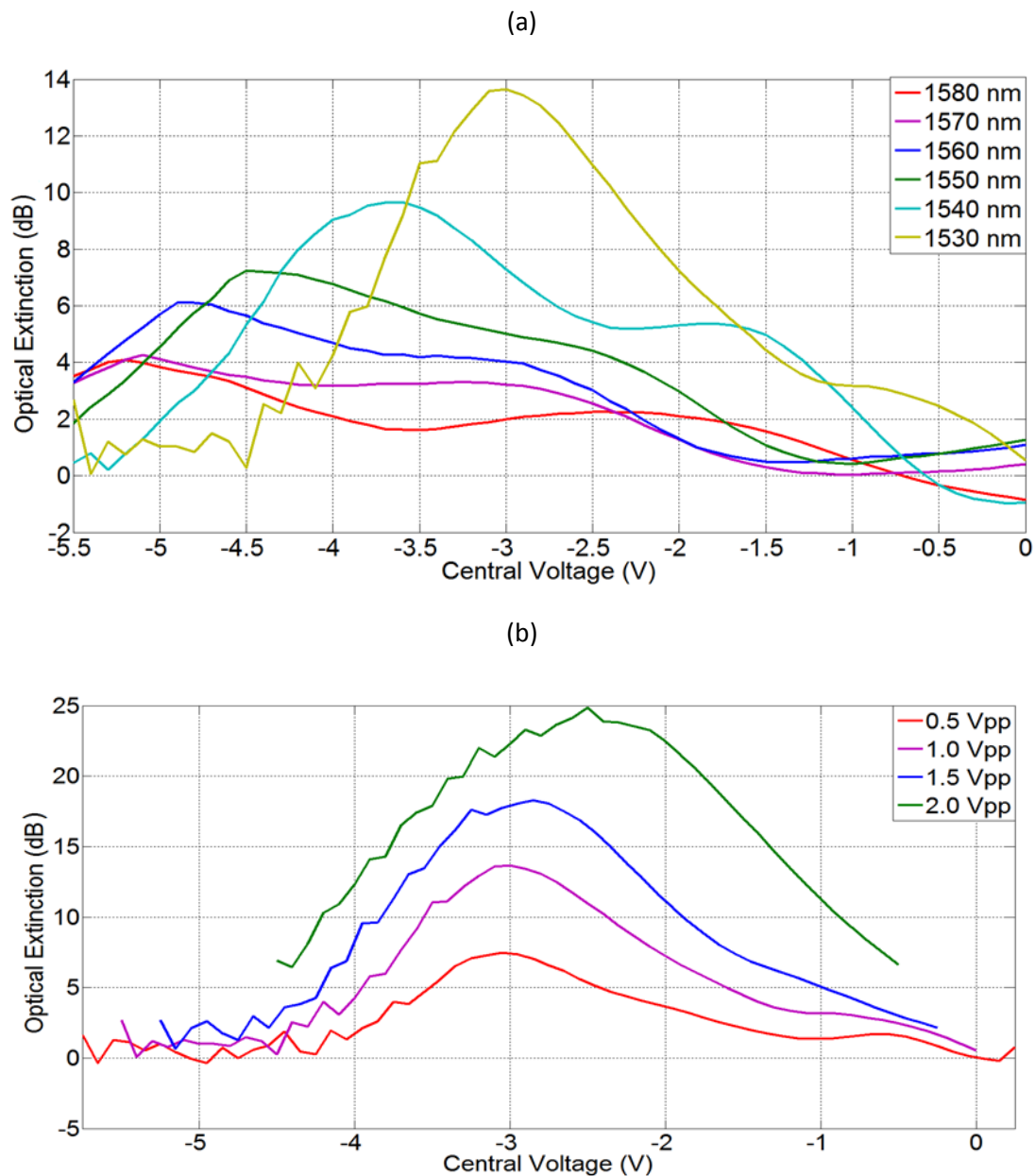


**Fig. 6.10:** (a) Microscopic image of cleaved 50  $\mu\text{m}$  lumped EAM under test and (b) transmitted optical power as a function of bias and wavelength

0 V begin to experience attenuation at higher biases. This field induced absorption of longer wavelengths demonstrates the quantum confined Stark effect.

The absorption spectrum was processed to calculate the optical extinction as a function of bias and wavelength. Figure 6.11a shows the DC optical extinction which corresponds to an RF signal with a peak to peak ( $V_{pp}$ ) voltage of 1 V. The central voltage plotted on the X axis represents the DC bias. To give an example for clarity, the points at  $-3$  V represents the optical extinction that can be expected if an RF signal with a  $V_{pp} = 1$  V offset by a DC bias of  $-3$  V was applied to the device for a given wavelength. This plot indicates that an optical extinction  $> 13$  dBm is possible at 1530 nm but decreases systematically as the wavelength increases. As the greatest performance was seen at 1530 nm, Figure 6.11b presents the optical extinction of the EAM at that wavelength as a function of  $V_{pp}$ . This information is crucial for the creation of an open eye diagram as it indicates the optimum wavelength and DC bias for a given  $V_{pp}$ . Based on this data, a wavelength of 1530 nm, a  $V_{pp}$  of 1 V and a DC bias of  $-2.5$  volts was chosen for the frequency response and eye diagram experiments outlined in the following sections. The optimal

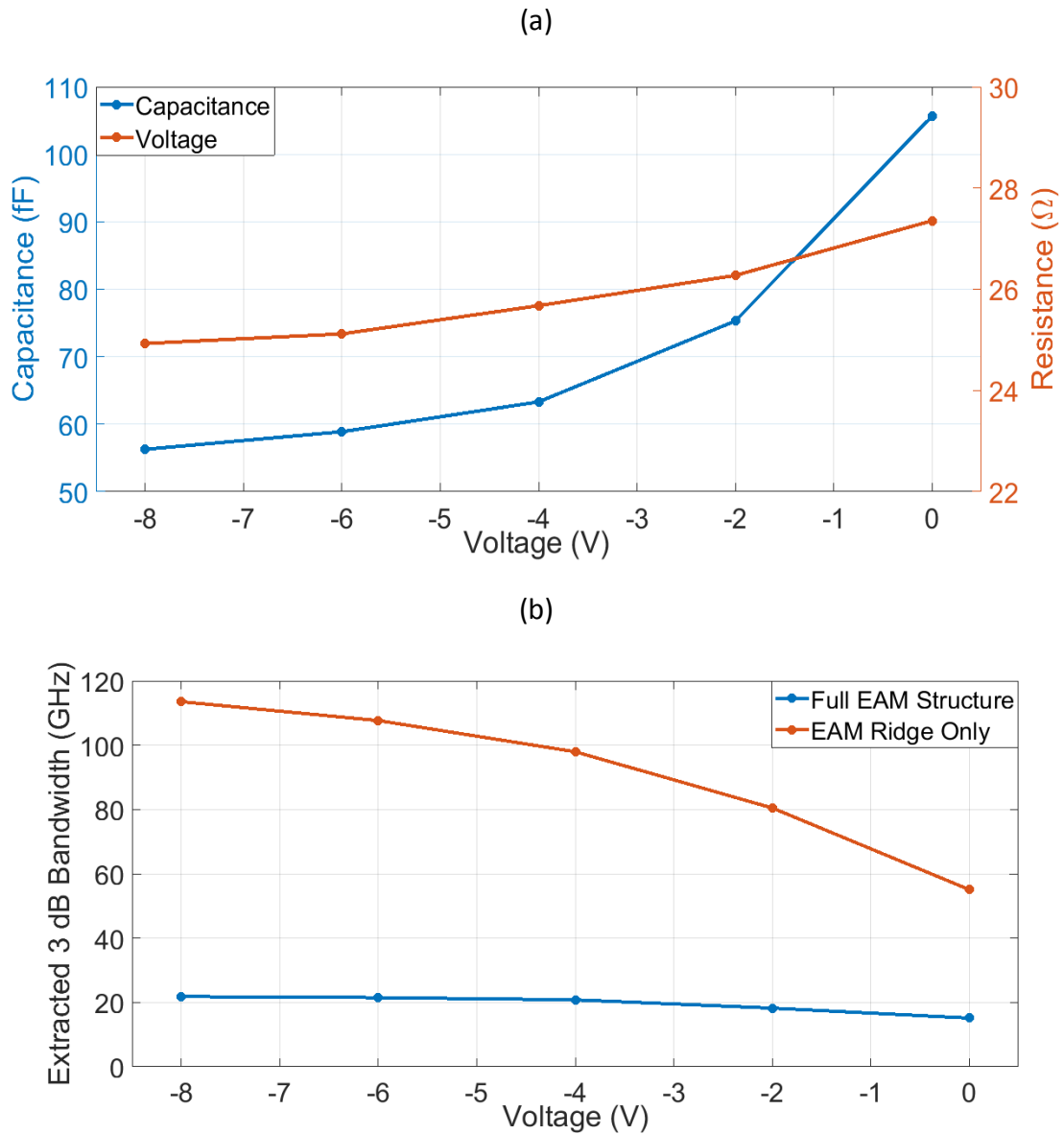
wavelength of this device could be tuned to longer wavelengths by adjusting the epitaxial design.



**Fig. 6.11:** (a) Optical extinction corresponding to a  $V_{pp}$  of 1 V for varying wavelength and (b) Optical extinction corresponding to a wavelength of 1530 nm for varying  $V_{pp}$ .

Using the parasitic values extracted from the test structure, it was possible to plot the resistance and capacitance of the EAM ridge structure as a function of bias, as shown in Figure 6.12a. Again, the decreasing capacitance as a function of reverse

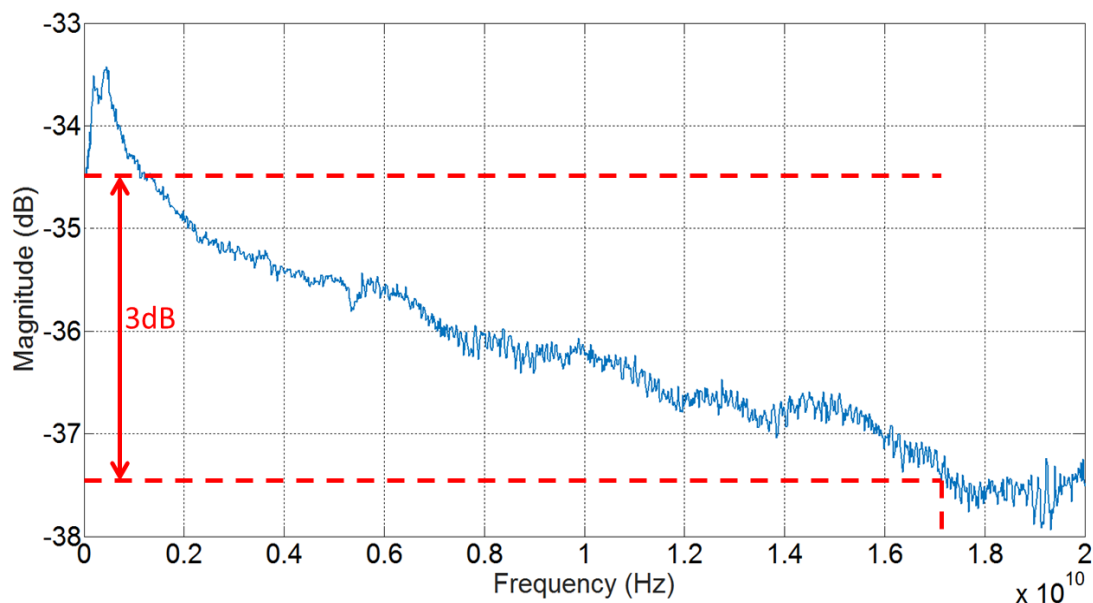
bias is a result of the increasing depletion region thickness. The 3 dB bandwidth of circuits representing the full device and the EAM ridge structure is plotted in Figure 6.12b. This indicates that the RF performance of the EAM is being significantly limited by the parasitic associated with the RF pads.



**Fig. 6.12:** (a) Optical extinction corresponding to a  $V_{pp}$  of 1 V for varying wavelength and (b) Optical extinction corresponding to a wavelength of 1530 nm for varying  $V_{pp}$ .

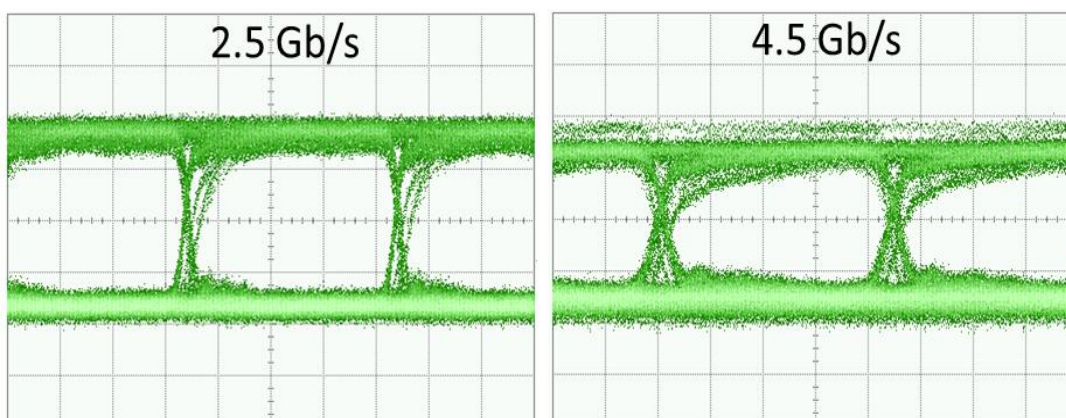
Figure 6.13 shows the measured electro-optic  $S_{21}$  response of the EAM between 0.1 and 20 GHz. For this measurement, a wavelength of 1530 nm, a DC bias of -2.5 V were used. The 3-dB bandwidth was calculated to be approximately 17.50 GHz.





**Fig. 6.13:** Electro-optic response of the EAM at 1530 nm.

As before, light with a wavelength of 1530 nm was coupled into the device. A pseudorandom binary sequence (PRBS) source provided a signal with a pattern length of  $2^7-1$ . This sequence was passed through an RF amplifier to increase the peak to peak voltage of the signal to 1 V. Finally, this amplified RF signal was combined with a DC bias of -2.5 V using a DC bias tee before being applied to the EAM via the high speed GSG probes. The output signal from the device was analysed with a 40 GHz photodiode and a digital communications analyzer (DCA). Figure 6.14 displays the observed eye diagrams. High quality eyes were achieved up to a speed of 12.5 Gbps (corresponding the maximum speed of the PRBS) demonstrating the successful operation of this device.





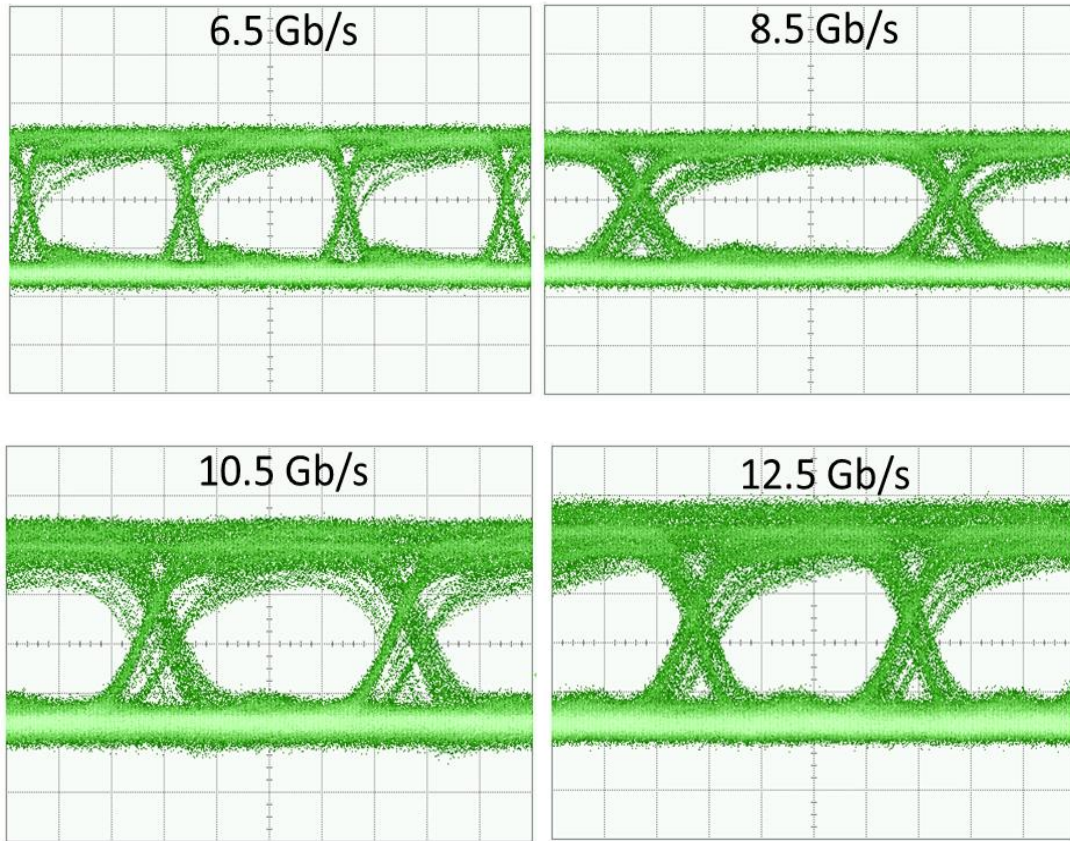


**Fig. 6.14:** Experimentally observed eye diagrams at bit rates ranging from 2.5 Gbps to 12.5 Gbps.

This EAM was sent to Rockley Photonics for further characterisation as part of an industrial collaboration with the integrated photonics group (IPG) at Tyndall National Institute, yielding a 25 Gbps eye diagram as shown in figure 6.15.

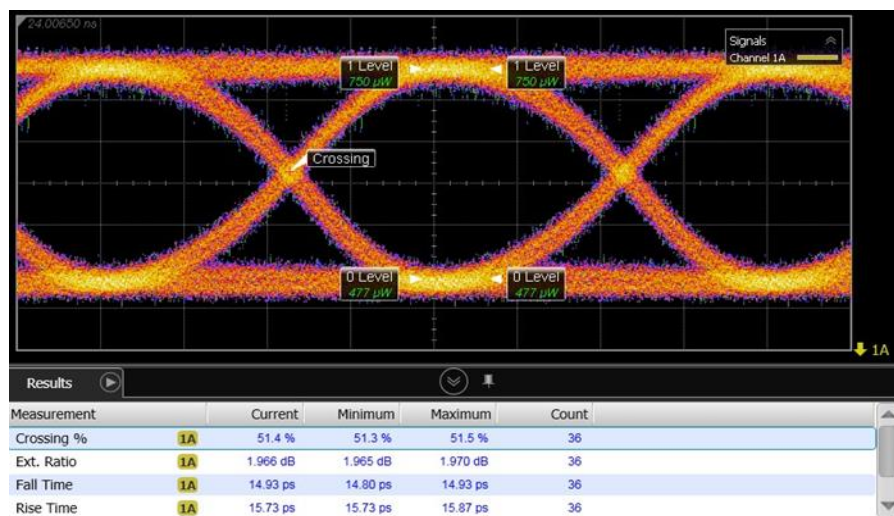


**Fig. 6.15:** 25.0 Gbps eye diagram measured by Rockley Photonics.

## 6.7 Curved EAM Design

Photonic integrated circuits have been demonstrated using various techniques such as monolithic integration, epitaxial regrowth, quantum well intermixing and the hybrid/heterogeneous integration of InP and Si. One such hybrid approach involves the flip-chip bonding of III-V devices onto silicon substrates as outlined in [21]. Therefore, a flip-chip compatible, lumped EAM is ideal for hybrid integration formats based on lateral coupling [22]. Moreover, a device whose input and output were located on the same side of the chip would minimise integration complexity by simplifying the layout for optical coupling between it and the host silicon platform.

Small low loss optical waveguide bends have been identified as a critical component for achieving compact photonic devices and integrated circuits [23]. An important consideration in designing these curved waveguides is the matching of the optical mode as it propagates through the bend [24]. While constant curvature bends provide a short path length, they are optically lossy due to mode mismatching attributed to the abrupt change in curvature between the straight and curved sections. Research has been published on the design and application of Euler bends [25], which apply a linearly changing radius of curvature to achieve low loss bends on a silicon platform. An alternative to Euler bends is a trapezoidal bend. These trapezoidal bends have a larger change of curvature than the equivalent Euler bend but a significantly smaller maximum curvature. The curvature profile of these three bend types are shown in Figure 6.16. This property gives the trapezoidal bend a shorter path length when applied to angles exceeding 120 degrees [26]. A detailed geometrical description of these three bend types is given in [27].

In this section, a curved electroabsorption modulator based on a trapezoidal bend is proposed and demonstrated. This lumped element EAM arcs 180 degrees so that its input and output face the same direction. This alignment of the ends of the modulator results in the realization of a device which can be coupled using a single fiber array, while maintaining a small footprint. This prototype EAM was monolithically integrated with two semiconductor optical amplifier sections (Figure 6.17). These sections were added to make the device compatible with our testing

facilities. The DC optical extinction of the device was shown to be >17 dBm over a 1 V range. An electro-optic 3dB bandwidth of 11.75 GHz was also recorded. The correct operation of this device was demonstrated by producing a 7.5 Gbps open eye diagram.

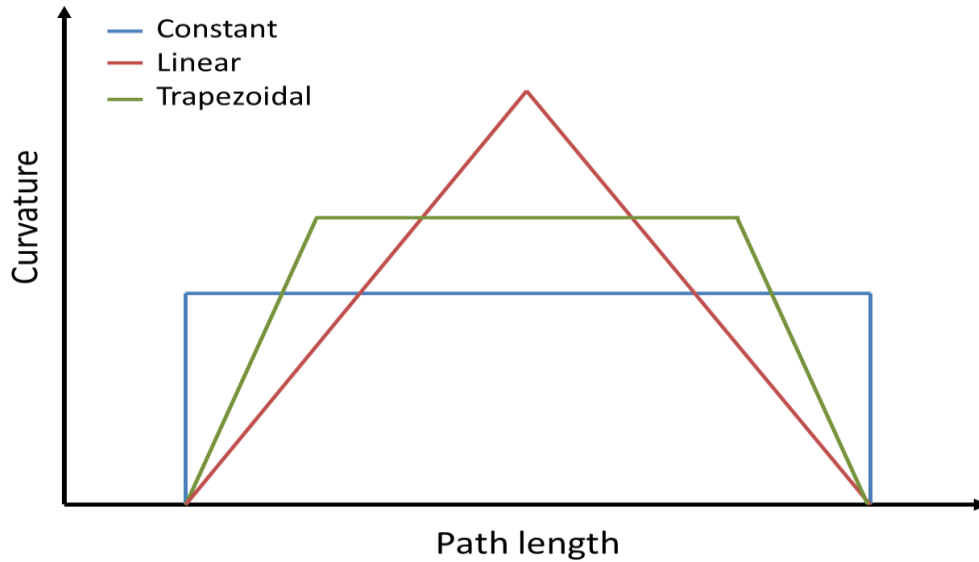


**Fig. 6.16:** Curvature versus path-length profile for constant, linear and trapezoidal curvature waveguide bends.

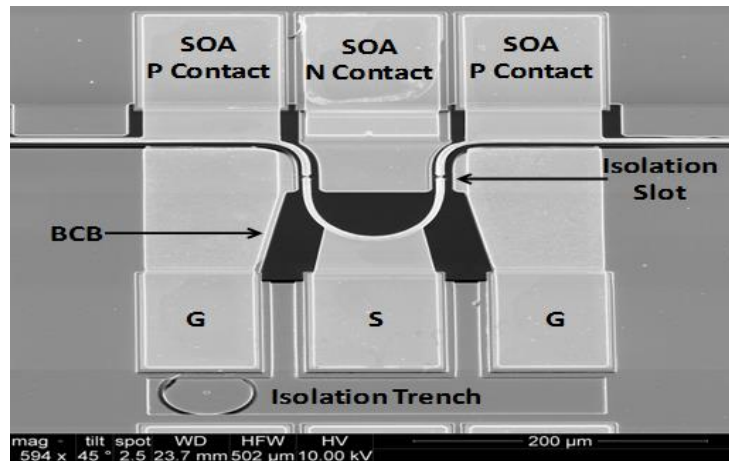
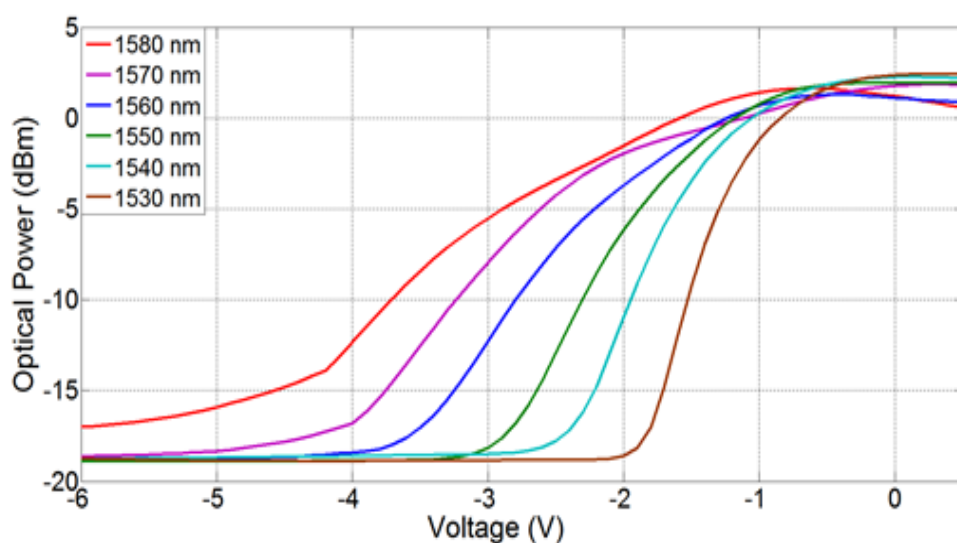


**Fig. 6.17:** Scanning electron microscope image of the curved electroabsorption modulator monolithically integrated with two SOA sections.

The device design centers around a 2.0 μm wide ridge waveguide structure which penetrates through the quantum wells and into to N layers to provide high optical confinement. The EAM section is based on a 180-degree trapezoidal bend

with a maximum radius of curvature of 75  $\mu\text{m}$  which equates to a device length of  $\sim 200 \mu\text{m}$ . Two angled slots provide electrical isolation between the EAM and the adjacent 180  $\mu\text{m}$  SOA sections. The design utilises a planar isolated pedestal GSG configuration with a pitch of 125  $\mu\text{m}$ . The pedestals are electrically isolated by a trench which encircles the signal pad. These planar pedestals provide an excellent platform for flip-chip integration and packaging due to the planarization of the contacts and the ridge waveguide. The transmitted optical power of this curved EAM was measured as a function of the varying applied voltage and wavelength of the injected light and is plotted in Figure 6.18a. Figure 6.18b shows the DC optical extinction which corresponds to a modulated signal with a peak to peak ( $V_{pp}$ ) voltage of 1 V. This plot indicates that an optical extinction  $> 17 \text{ dBm}$  is possible at 1530 nm but decreases systematically as the wavelength increases. This high optical extinction can be attributed to the relatively long length of the device and the high optical confinement due to the deep etched ridge structure. Since the greatest performance was seen at 1530 nm, Figure 6.18c presents the optical extinction of the EAM at that wavelength as a function of  $V_{pp}$ . Based on this data a wavelength of 1530 nm, a  $V_{pp}$  of 1 V and a DC bias of -1.5 volts was chosen for the frequency response and eye diagram experiments outlined in the following sections. Again, the optimal wavelength of this device could be tuned to longer wavelengths by adjusting the epitaxial design.

(a)



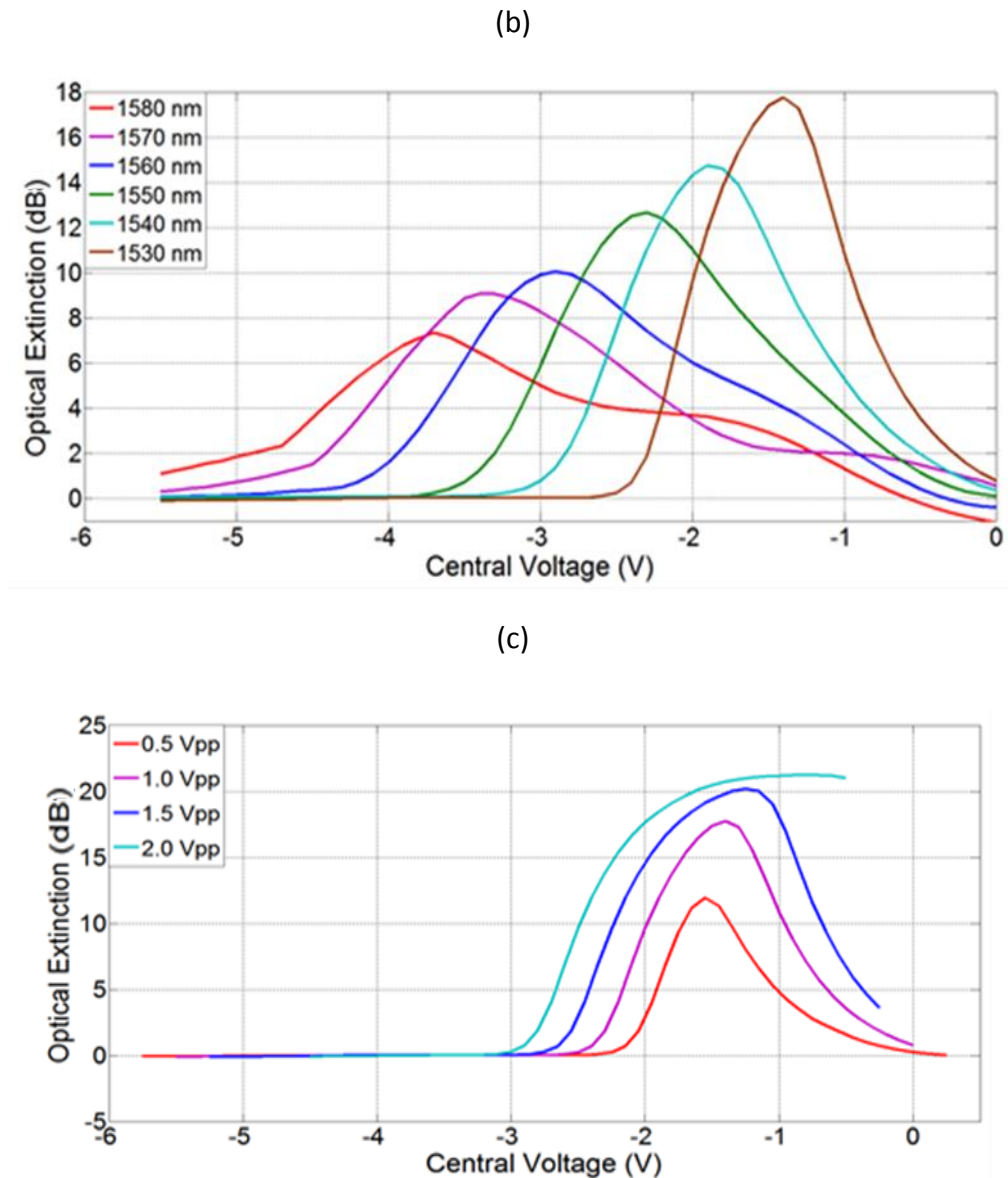
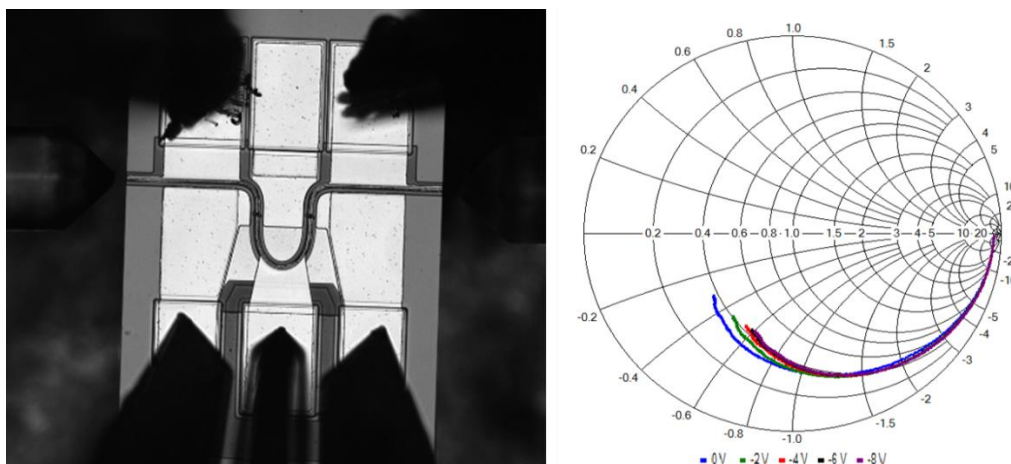


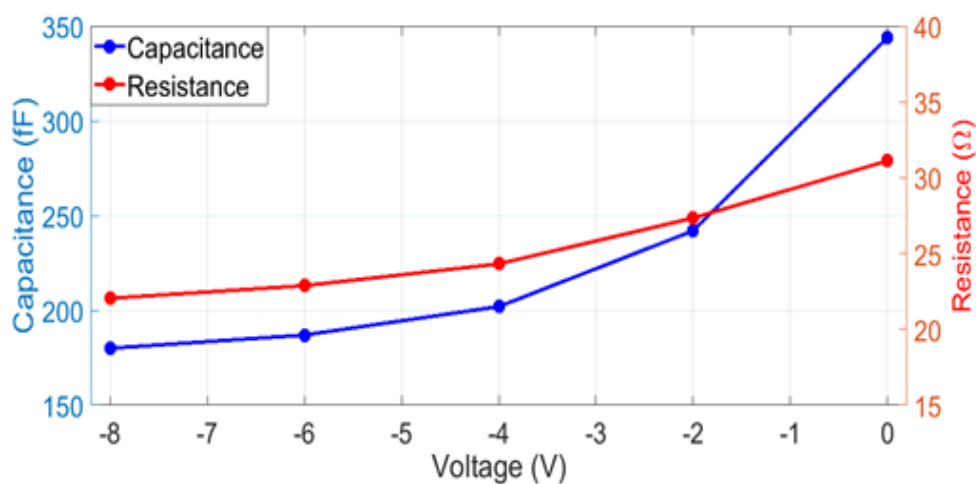
**Fig. 6.18:** (a) Measured optical transmission response as a function of bias and wavelength (b) Optical extinction corresponding to a  $V_{pp}$  of 1 V for varying wavelength and (c) Optical extinction corresponding to a wavelength of 1530 nm for varying  $V_{pp}$ .

Next, the scattering matrix  $S_{11}$  of the full curved EAM device was measured for varying reverse biases (Figure 6.19a). Using an expanded circuit model and the parasitic values extracted from the test structure, the extracted resistance and capacitance is plotted in Figure 6.19b. The 3-dB bandwidth of the equivalent circuit representing the full device and the EAM ridge structure is plotted in Figure 6.19c. This indicates that the RF performance of the EAM is being significantly limited by the parasitics associated with the RF pads.

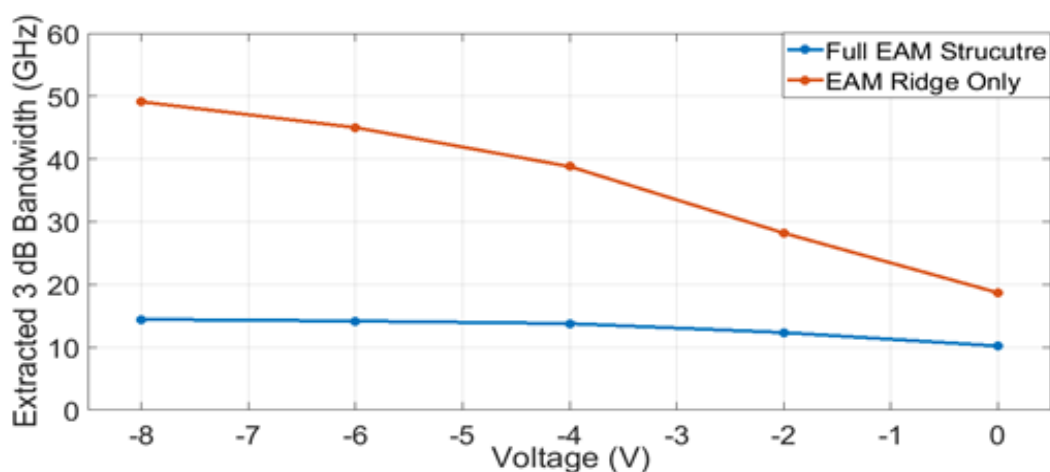
(a)



(b)



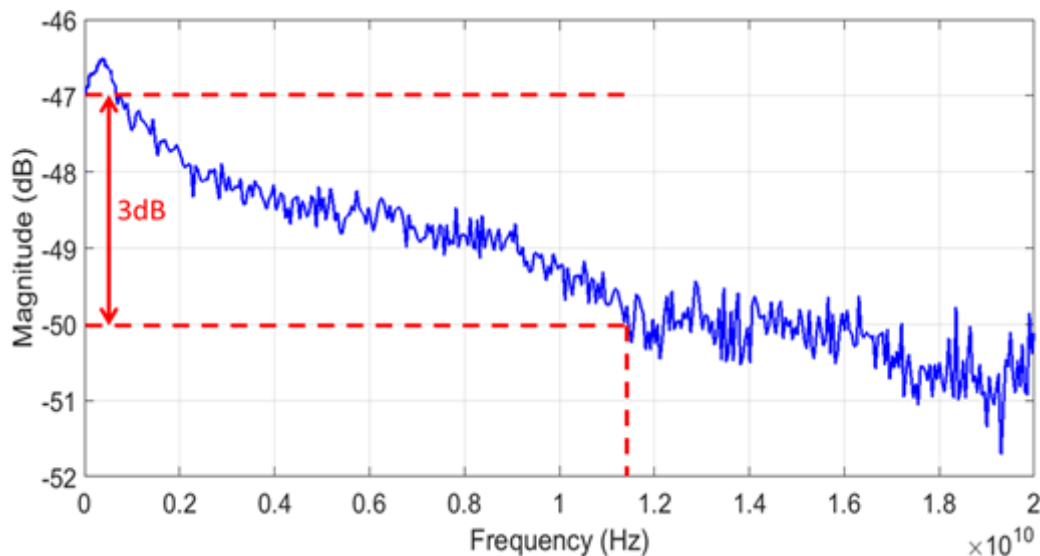
(c)



**Fig. 6.19:** (a) Microscopic image of EAM and corresponding S11 measurements (b) Capacitance and resistance plots of EAM ridge structure as a function of bias (c) Extracted 3 dB bandwidth plots for the full EAM device and the EAM ridge structure.

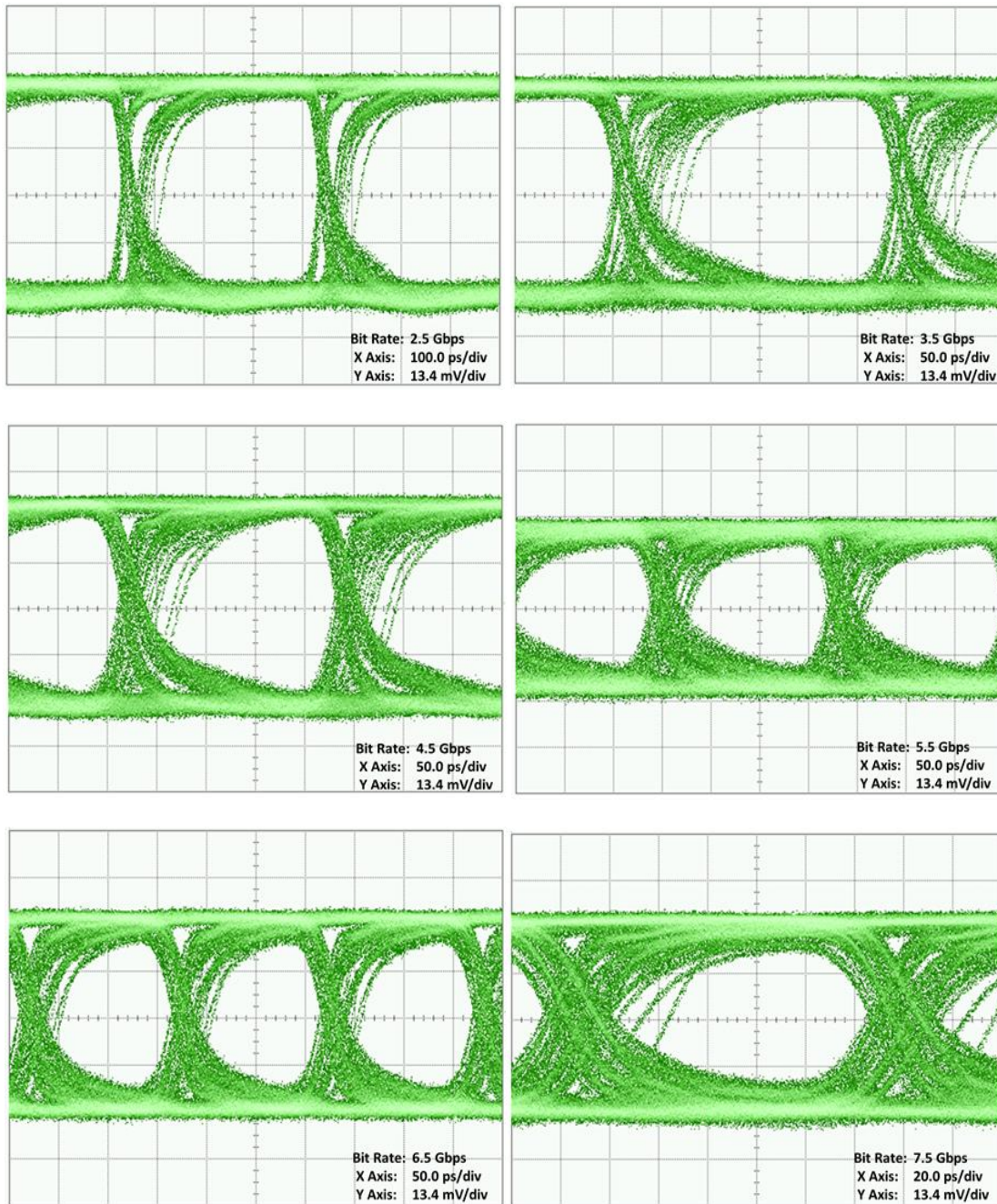


Figure 6.20 shows the measured electro-optic S21 response of the EAM between 0.1 and 20 GHz. For this measurement, a wavelength of 1530 nm, a DC bias of -1.5 V were used. The 3 dB bandwidth was calculated to be approximately 11.75 GHz. The high speed performance of the EAM could be improved by reducing its bend radius which would shorten the device length and lower the diode capacitance. Another possible improvement would be to widen the isolation trench which would reduce the effect of the parasitic capacitance of the RF pads.



**Fig. 6.20:** Electro-optic response of the curved EAM at 1530 nm.

As before, light with a wavelength of 1530 nm was coupled into the device. A pseudorandom binary sequence source provided a signal with a pattern length of  $2^7 - 1$ . This sequence was passed through an RF amplifier to increase the peak to peak voltage of the signal to 1 V. Finally, this amplified RF signal was combined with a DC bias of -1.5 V using a DC bias tee before being applied to the EAM via the high speed GSG probes. The output signal from the device was analysed with a 40 GHz photodiode and a digital communications analyser. Figure 6.21 displays the observed eye diagrams. Open eyes were achieved up to a speed of 7.5 Gbps demonstrating the successful operation of this device. There is a pattern dependent turn on seen in the eye, which is believed to be caused by the unbiased SOA section after the EAM. This delay causes the eye to degrade at 8.5 Gbps and is effectively closed at 12.5 Gbps.



**Fig. 6.21:** Experimentally observed eye diagrams at bit rates ranging from 2.5 Gbps to 7.5 Gbps.

### 6.8 Summary

This chapter discussed the design consideration such as electrode configuration and epitaxial structure associated with high speed electroabsorption modulators. These considerations were applied to a lumped EAM suitable for use in monolithic photonic integrated circuits and a curved electroabsorption modulator based on a trapezoidal bend. The 3 dB bandwidths were measured to be 17.5 GHz and 11.75



GHz respectively. This corresponded to open eye diagrams at 25.0 Gbps and 7.5 Gbps respectively, verifying the correct operation of the modulators. The devices were fabricated using UV lithography and did not require any epitaxial regrowth.

### **Bibliography**

- [1] C. R. Doerr *et al.*, "Compact High-Speed InP DQPSK Modulator," *IEEE Photonics Technol. Lett.*, vol. 19, no. 15, pp. 1184–1186, Aug. 2007.
- [2] C. L. M. Daunt *et al.*, "Compact Electroabsorption Modulators for Photonic Integrated Circuits, Using an Isolated Pedestal Contact Scheme," *IEEE Photonics Technol. Lett.*, vol. 24, no. 5, pp. 356–358, Mar. 2012.
- [3] H. Yang *et al.*, "Design and fabrication of high-performance InGaAsP/InP electroabsorption modulator," 2007, p. 67820U.
- [4] G. I. Li, S. . Pappert, P. Mages, C. k. Sun, W. s. c. Chang, and P. k. I. Yu, "High-saturation high-speed traveling-wave InGaAsP-InP electroabsorption modulator," *IEEE Photonics Technol. Lett.*, vol. 13, no. 10, pp. 1076–1078, 2001.
- [5] I. P. Kaminow and J. Liu, "Propagation characteristics of partially loaded two-conductor transmission line for broadband light modulators," *Proc. IEEE*, vol. 51, no. 1, pp. 132–136, 1963.
- [6] R. G. Walker, "High-speed III-V semiconductor intensity modulators," *IEEE J. Quantum Electron.*, vol. 27, no. 3, pp. 654–667, Mar. 1991.
- [7] R. Spickermann, S. R. Sakamoto, and N. Dagli, "In traveling wave modulators which velocity to match?," in *Conference Proceedings LEOS'96 9th Annual Meeting IEEE Lasers and Electro-Optics Society*, vol. 2, pp. 97–98.
- [8] W. S. C. (William S. Chang, *RF photonic technology in optical fiber links*. Cambridge University Press, 2002.
- [9] Yih-Guei Wey *et al.*, "110-GHz GaInAs/InP double heterostructure p-i-n photodetectors," *J. Light. Technol.*, vol. 13, no. 7, pp. 1490–1499, Jul. 1995.

- [10] U. Westergren, Y. Yu, P. Janes, P. Holmstrom, and L. Thylen, "Efficient and Compact Light-Intensity Modulators for High Frequencies and High Bitrates," in *2006 International Conference on Transparent Optical Networks*, 2006, vol. 2, pp. 142–145.
- [11] F. H. Peters and J. Geske, "Low-capacitance bond pads for high speed devices," 2002.
- [12] C. L. M. Daunt *et al.*, "Dielectric-Free Fabrication of Compact 30-GHz Photodetectors Using the Isolated Pedestal Contact Configuration," *IEEE Photonics Technol. Lett.*, vol. 24, no. 13, pp. 1082–1084, Jul. 2012.
- [13] S. Hojfeldt and J. Mork, "Modeling of carrier dynamics in quantum-well electroabsorption modulators," *IEEE J. Sel. Top. Quantum Electron.*, vol. 8, no. 6, pp. 1265–1276, Nov. 2002.
- [14] S. Adachi, *Physical Properties of III-V Semiconductor Compounds*. Weinheim, FRG: Wiley-VCH Verlag GmbH & Co. KGaA, 1992.
- [15] P. K. L. Yu, "Ultrahigh-Speed Traveling-Wave Electroabsorption Modulator—Design and Analysis," *IEEE Trans. Microw. Theory Tech.*, vol. 47, no. 7, 1999.
- [16] C. L. M. Daunt *et al.*, "Sub 10 ps Carrier Response Times in Electroabsorption Modulators Using Quantum Well Offsetting," *IEEE J. Quantum Electron.*, vol. 48, no. 11, pp. 1467–1475, Nov. 2012.
- [17] "SimWindows - 1D Semiconductor Device Simulator." [Online]. Available: <http://simwindows.wixsite.com/simwindows>. [Accessed: 19-May-2017].
- [18] R. J. Young *et al.*, "Low-angle misorientation dependence of the optical properties of InGaAs/InAlAs quantum wells," Apr. 2010.
- [19] C. Chellic *et al.*, "Minority carrier lifetime in MOCVD-grown C- and Zn-doped InGaAs," in *Conference Proceedings. Eleventh International Conference on Indium Phosphide and Related Materials (IPRM'99) (Cat. No.99CH36362)*, pp. 127–130.

- [20] H. Sugiyama, H. Yokoyama, K. Watanabe, and T. Kobayashi, "Diffusion behavior of delta-doped Si in InAlAs/InP heterostructures," Jan. 2002.
- [21] S. Tanaka, S.-H. Jeong, S. Sekiguchi, T. Kurahashi, Y. Tanaka, and K. Morito, "High-output-power, single-wavelength silicon hybrid laser using precise flip-chip bonding technology," *Opt. Express*, vol. 20, no. 27, p. 28057, Dec. 2012.
- [22] Y. Tang, J. D. Peters, and J. E. Bowers, "Energy-Efficient Hybrid Silicon Electroabsorption Modulator for 40-Gb/s 1-V Uncooled Operation," *IEEE Photonics Technol. Lett.*, vol. 24, no. 19, pp. 1689–1692, Oct. 2012.
- [23] M. Cherchi, S. Ylinen, M. Harjanne, M. Kapulainen, and T. Aalto, "Dramatic size reduction of waveguide bends on a micron-scale silicon photonic platform," *Opt. Express*, vol. 21, no. 15, p. 17814, Jul. 2013.
- [24] A. Melloni, P. Monguzzi, R. Costa, and M. Martinelli, "Design of curved waveguides: the matched bend," *J. Opt. Soc. Am. A*, vol. 20, no. 1, p. 130, Jan. 2003.
- [25] M. Cherchi, S. Ylinen, M. Harjanne, M. Kapulainen, T. Vehmas, and T. Aalto, "The Euler bend: paving the way for high-density integration on micron-scale semiconductor platforms," 2014, p. 899004.
- [26] R. N. Sheehan, S. Horne, and F. H. Peters, "The design of low-loss curved waveguides," *Opt. Quantum Electron.*, vol. 40, no. 14–15, pp. 1211–1218, Nov. 2008.
- [27] R. N. and F. H. Peters, "Bends in the Plane with Variable Curvature," *Bull. Irish Math. Soc.*, vol. 78, pp. 61–80, 2016.



# Chapter 7

## Conclusions and Future Work

### 7.1 Summary

Consumer internet traffic continues to grow at an exponential rate due primarily to the rise in popularity of bandwidth intensive services such as video streaming. As a result, communication networks need to be continually upgraded to keep up with this demand. However, these networks utilise extensive submarine cables which are expensive to replace. Therefore, short term solutions focus on increasing the information spectral density of existing systems. One such approach aims to further reduce the channel spacing in WDM systems by means of coherent carriers. Due to this coherence, inter-channel crosstalk becomes deterministic and can be minimized. In addition, significant effort has gone into the development of integrated photonic circuits which strive to replicate the successes achieved in the electronic domain, thus benefiting from reduced cost, greater reliability, and lower power consumption. To this end, this thesis proposed a monolithic regrowth-free design for a coherent WDM transmitter which requires less sophisticated fabrication techniques than alternative methods and would therefore be more cost effective to manufacture. The work began with the development of suitable processes for the fabrication of DC and high-speed components associated with the transmitter. Utilising the associated composite hard mask process, an integratable laser which was based on the self-imaging properties of propagating multimode wave and total internal reflection was developed. Five distinct wavelengths over a range of 15 nm were achieved with an associated SMSR of 30 dB. Next, the integration of core components required for the OFDM transmitter was undertaken. The monolithic integration of a 1x2 MMI, two SFP lasers, two EAMs, and a star coupler was demonstrated using free-growth free epitaxy and UV lithography. The feasibility of integrating an SFP laser with an EAM by means of injection locking was also investigated, resulting in the production of a 2.5 Gbps eye diagram. It was shown that the high-speed performance of these PICs could be improved by using more advanced modulator designs. As a result, this

thesis concluded with the investigation of high speed modulators with the aim of to increase the data rate of the developed PICs. An integratable electroabsorption modulator with a 3-dB bandwidth of 17.5 GHz and a corresponding 25 Gbps eye diagram was realised. This work also yielded a curved modulator suitable for heterogeneous integration using flip chip packaging.

### 7.2 Future Work

As discussed above, the central concept of this thesis is a monolithic regrowth-free coherent WDM transmitter. Such a design is reliant on the realisation of a number of technologies, namely:

1. An on-chip comb source which can be red shifted;
2. Active filtering of comb lines using SFP laser;
3. A suitable monolithic regrowth-free fabrication process;
4. The integration of SFP laser and EAM by means of injection locking;
5. A PIC with negligible optical/thermal crosstalk between arms;
6. An integratable high speed modulator design.

While an integratable comb source design and an investigation into the active filtering properties of SFP lasers were pre-existing, this thesis has successfully explored points 3-6. Therefore, all the key components required for such a device have now been demonstrated. The logical continuation of this research is to proceed with the integration of such components. This would begin with the addition of a comb source to the developed PIC in Chapter 5, facilitating the characterisation of an SFP laser as an active filter when operating with an integrated comb source. A key milestone of this characterisation would be the simultaneous injection locking of the two arms of the PIC to different comb-lines, demonstrating that such a configuration is capable of acting as a form of demultiplexer. Next, the characterised high-speed modulator designs would be added so that the filtered carriers could be modulated and then multiplexed, creating a prototype coherent WDM transmitter. Finally, the number of arms would be increased so that all suitable comb-lines can be independently filtered and encoded, maximizing the data rate of the transmitter. Achieving such integration would result in a WDM transmitter suitable for long haul

## Conclusions and Future Work

communications with minimal inter-channel spacing. It would also use less sophisticated fabrication techniques and would therefore be more cost effective to manufacture when compared with other approaches currently being proposed.

## Conclusions and Future Work



# Appendix A: Epitaxial Structures

## A.1 Commercial Laser Epitaxy

Material	Repeated	x	y	Thickness (nm)	Dopant
GaIn(x)As		0.53		0.2	Zinc
GaIn(x)As(y)P		0.71	0.62	0.05	Zinc
InP				1.6	Zinc
GaIn(x)As(y)P		0.85	0.33	0.02	Zinc
InP				0.5	Zinc
Al(x)GaIn(y)As		0.9	0.53	0.06	Zinc
Al(x)GaIn(y)As		0.9	0.53	0.06	Undoped
Al(x)GaIn(y)As		0.44	0.49	0.01	Undoped
Al(x)GaIn(y)As	x5	0.24	0.71	0.006	Undoped
Al(x)GaIn(y)As	x5	0.44	0.49	0.01	Undoped
Al(x)GaIn(y)As		0.9	0.53	0.06	Undoped
Al(x)GaIn(y)As		0.9	0.53	0.07	Silicon
InP				120	Silicon

**A.2 High Speed Electroabsorption Modulator Epitaxy**

Material	Repeated	Eg (nm)	Thickness (nm)	Doping ( $1e^{18}$ )	Dopant
GaIn(x)As		1499.9800	150	10	Zinc
GaIn(x)As(y)P		1302.9100	50	1.5	Zinc
InP		918.4070	1340	1.0	Zinc
Al(x)GaIn(y)As		843.4350	60	1.0	Zinc
Al(x)GaIn(y)As		968.0350	35		
Al(x)GaIn(y)As		1097.7600	35		
Al(x)GaIn(y)As	X8	1239.8500	10		
Al(x)GaIn(y)As	X8	1549.8100	7.5		
Al(x)GaIn(y)As		1549.8100	7.5		
Al(x)GaIn(y)As		1239.8500	10		
InGaAsP		1100.0000	210		
InP		918.4070	80	0.2	Silicon
InP		918.4070	70	0.5	Silicon
InP		918.4070	920	0.8	Silicon
InP		918.4070	500		Iron